

AD-A056 715

MASSACHUSETTS INST OF TECH LEXINGTON LINCOLN LAB  
SOLID STATE RESEARCH, 1978: 1.(U)  
FEB 78 A L MCWHORTER

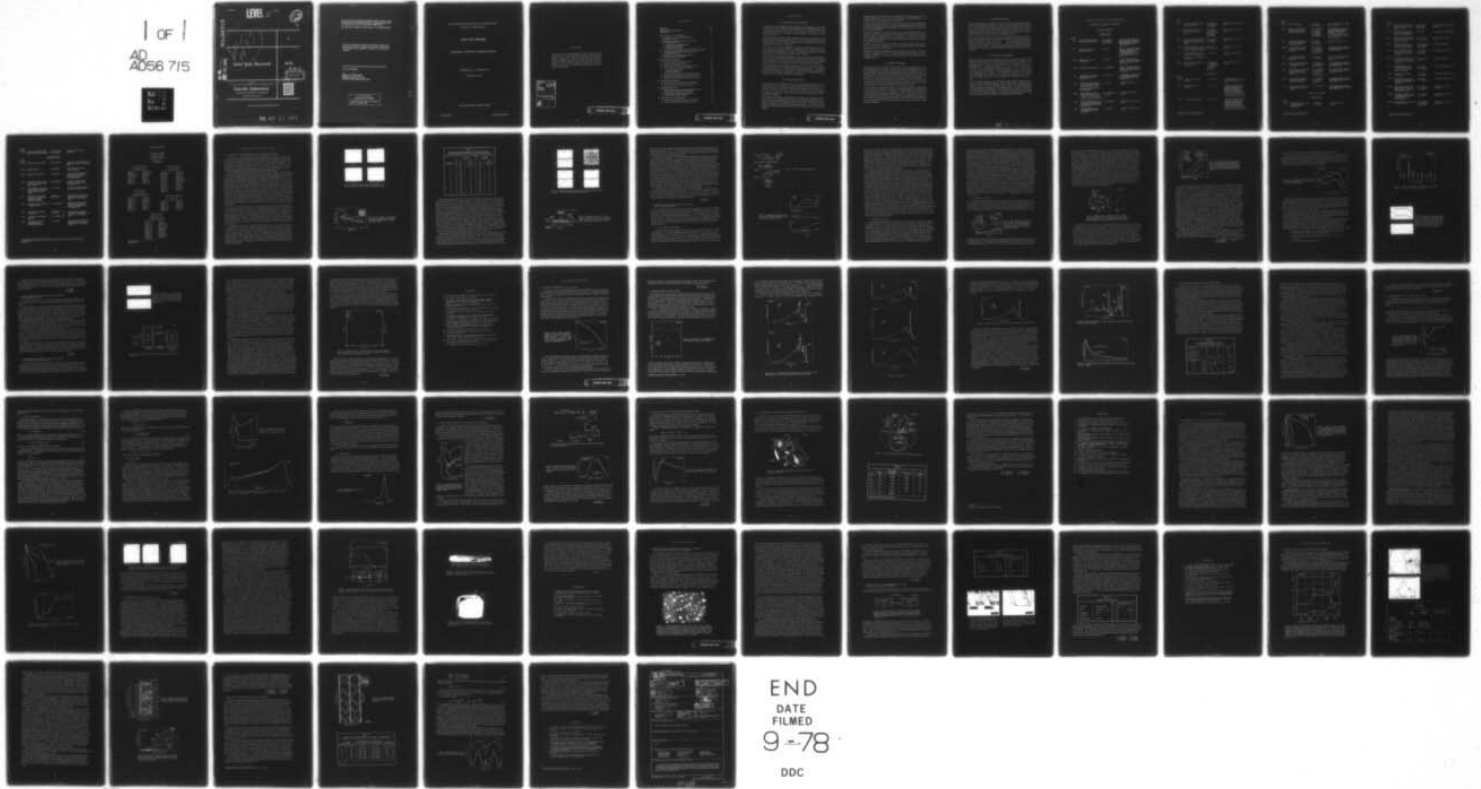
F/G 5/1

UNCLASSIFIED

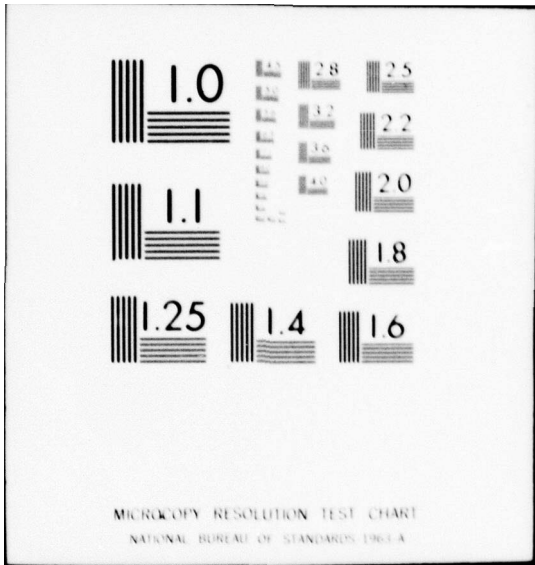
ESD-TR-78-27

F19628-78-C-0002  
NL

1 of 1  
AD  
A056 715



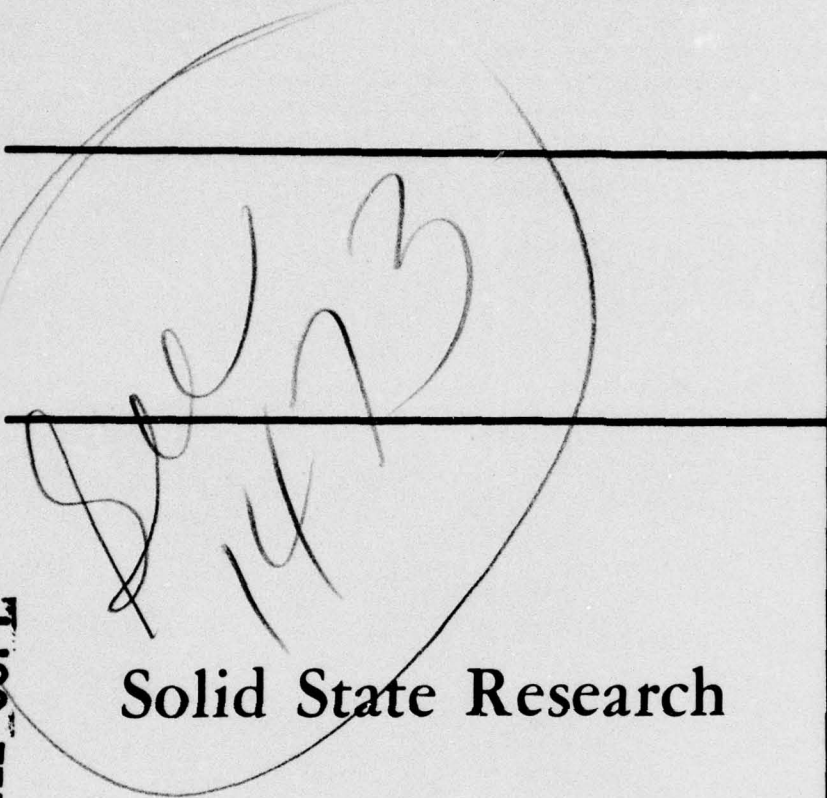
END  
DATE  
FILMED  
9-78  
DDC



**LEVEL II** 1

12

AD A 056715



1

AU NO. \_\_\_\_\_  
DDC FILE COPY

**Solid State Research**

1978

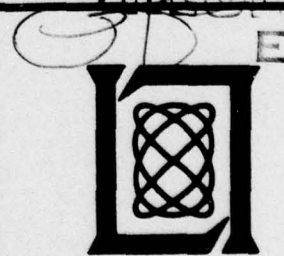
DDC  
RECEIVED  
JUL 26 1978

Prepared  
under Electronic Systems Division Contract F19628-78-C-0002 by

**Lincoln Laboratory**

MASSACHUSETTS INSTITUTE OF TECHNOLOGY

LEXINGTON, MASSACHUSETTS



Approved for public release; distribution unlimited.

78 07 24 031

The work reported in this document was performed at Lincoln Laboratory, a center for research operated by Massachusetts Institute of Technology, with the support of the Department of the Air Force under Contract F19628-78-C-0002.

This report may be reproduced to satisfy needs of U.S. Government agencies.

The views and conclusions contained in this document are those of the contractor and should not be interpreted as necessarily representing the official policies, either expressed or implied, of the United States Government.

This technical report has been reviewed and is approved for publication.

FOR THE COMMANDER

*Raymond L. Loiselle*

Raymond L. Loiselle, Lt. Col., USAF  
Chief, ESD Lincoln Laboratory Project Office

Non-Lincoln Recipients

**PLEASE DO NOT RETURN**

Permission is given to destroy this document  
when it is no longer needed.

MASSACHUSETTS INSTITUTE OF TECHNOLOGY  
LINCOLN LABORATORY

SOLID STATE RESEARCH

QUARTERLY TECHNICAL SUMMARY REPORT

1 NOVEMBER 1977 - 31 JANUARY 1978

ISSUED 25 MAY 1978

Approved for public release; distribution unlimited.

LEXINGTON

MASSACHUSETTS

ABSTRACT

This report covers in detail the solid state research work of the Solid State Division at Lincoln Laboratory for the period 1 November 1977 through 31 January 1978. The topics covered are Solid State Device Research, Quantum Electronics, Materials Research, Microelectronics, and Surface-Wave Technology. Funding is primarily provided by the Air Force, with additional support provided by the Army, ARPA, NSF, and DOE.

ACCESSION for	
NTIS	White Section <input checked="" type="checkbox"/>
DDC	Buff Section <input type="checkbox"/>
UNANNOUNCED	<input type="checkbox"/>
JUSTIFICATION.....	
BY.....	
DISTRIBUTION/AVAILABILITY CODES	
Dist.	AVAIL. and/or SPECIAL
A	

PRECEDING PAGE BLANK

## CONTENTS

Abstract	iii
Introduction	vii
Reports on Solid State Research	xi
Organization	xvi
I. SOLID STATE DEVICE RESEARCH	1
A. 12-Element, 1.4-GHz Bandwidth HgCdTe Heterodyne Arrays	1
B. Acoustically Scanned Si-Diode Array/LiNbO <sub>3</sub> Optical Imaging Devices	5
1. Device Structure and Operation	5
2. Charging Characteristics	7
3. Imaging Characteristics	8
C. Life Tests of Double-Heterostructure GaInAsP/InP Lasers	11
D. Pulse Response and Modulation Characteristics of GaInAsP/InP Lasers	13
E. Automatic Measurement of Hall Coefficient and Resistivity vs Temperature	13
II. QUANTUM ELECTRONICS	19
A. Thermal Properties of Nd <sub>x</sub> La <sub>1-x</sub> P <sub>5</sub> O <sub>14</sub>	19
B. Transition-Metal Doped Lasers	20
C. Laser-Induced Breakdown of Cryogenic Liquids	25
D. Laser Association of Diatomic Molecules	27
1. General Considerations	28
2. Specific Examples	29
E. Optical Energy Extraction from Molecular Mercury	32
F. Photolytically Excited Mercurous Bromide Laser	34
G. High-Sensitivity Submillimeter Heterodyne Receiver	35
III. MATERIALS RESEARCH	39
A. Bias-Assisted CdTe Photoemitter Development	39
B. Synthesis and Crystal Growth of CdGeP <sub>2</sub>	43
IV. MICROELECTRONICS	49
A. Oriented Crystal Growth on Amorphous Substrates Using Artificial Surface-Relief Gratings	49
B. Fabrication of Vertical-Sidewall Patterns in Glass Films on GaAs Substrates	51
V. SURFACE-WAVE TECHNOLOGY	55
A. Surface-Acoustic-Wave Properties of Fresnoite	55
B. Analysis of Propagation Modes in Convolver	59

## INTRODUCTION

### I. SOLID STATE DEVICE RESEARCH

A 12-element, 1.4-GHz bandwidth HgCdTe photodiode array designed for rapid target acquisition for a CO<sub>2</sub> laser radar has been developed with measured individual element heterodyne sensitivities better than  $7 \times 10^{-20}$  W/Hz and  $11 \times 10^{-20}$  W/Hz at 760 MHz and 1.5 GHz, respectively. RF crosstalk between elements was found to be less than -22 dB at 1.4 GHz.

The gap-coupled Si-diode array/LiNbO<sub>3</sub> acoustoelectric memory correlator has been operated as a linear optical imager device and at a scan rate compatible with real-time imaging systems. It has been shown that  $40 \text{ mW/cm}^2$  can be detected in 15 msec; this corresponds to a sensitivity of  $600 \text{ pJ/cm}^2$ .

Life tests on 13 CW, room-temperature GaInAsP/InP double-heterostructure diode lasers are being carried out. Lifetimes have ranged from a few hundred to 7500 hours, with three devices still operating. For most of the lasers which have failed, end-face degradation has been identified as the primary cause of failure.

Pulse response and modulation experiments have been carried out on GaInAsP/InP diode lasers and yield output pulse risetimes of approximately 250 psec and a modulation of 200 Mpps. When the DC bias was just below the laser threshold, the damped relaxation oscillation is minimized and a relatively clean output pulse is obtained.

An automatic system which measures the Hall coefficient and electrical resistivity versus temperature from 4 to 300 K has been constructed and operated. The apparatus is being used to characterize LPE growth of InP and InGaAsP alloys. Analysis of the data shows the donor and acceptor impurity concentrations in a LPE grown film of InP to be  $1.8 \times 10^{16} \text{ cm}^{-3}$  and  $6.5 \times 10^{15} \text{ cm}^{-3}$ , respectively.

### II. QUANTUM ELECTRONICS

Using a dynamic electrical heating technique, the thermal conductivity and specific heat have been determined for NdP<sub>5</sub>O<sub>14</sub>, a high-Nd-concentration laser material. The measured values of the thermal conductivity tensor elements (in W/cm-K) are  $\Lambda_a = 2.10 \times 10^{-2}$ ,  $\Lambda_b = 9.66 \times 10^{-3}$ , and  $\Lambda_c = 1.40 \times 10^{-2}$ . The specific heat is 0.141 cal/g-K, in excellent agreement with the value of 0.139 cal/g-K that was measured by differential scanning calorimetry.

A study of the spectral output characteristics of a Ni:MgF<sub>2</sub> laser operating at a wavelength of 1.64  $\mu\text{m}$  has indicated that the transition is primarily homogeneously broadened. The fluorescence lineshape and lifetime have also been measured in Ni:MgF<sub>2</sub> as a function of temperature, polarization, and Ni concentration. In addition, the lineshape and lifetime as a function of temperature have been observed for CO:MgF<sub>2</sub> and Ni:MgO.

Measurements have been made of the CO<sub>2</sub> laser induced breakdown parameters of the cryogenic liquids CO, O<sub>2</sub>, N<sub>2</sub>, and Ar for various spot sizes and pulse durations. The underlying physical mechanisms have been considered.

Ultraviolet association of diatomic molecules has been examined as a mechanism for inverting a tunable gas laser and as a means of investigating the structure of molecular species which are unbound in their ground state. Spectroscopic studies have been carried out on Hg<sub>2</sub><sup>\*</sup> and XeBr<sup>\*</sup>.

A technique for optically extracting the energy stored in metastable Hg<sub>2</sub><sup>\*</sup> has been considered. The process uses an infrared laser, such as HF, to transfer the relatively large population in the O<sub>g</sub><sup>±</sup> levels to the 1<sub>u</sub> radiating level. As a result, inversion on the 1<sub>u</sub> → O<sub>g</sub><sup>+</sup> (300 nm) transition can be created. Measurements have been made of HF laser induced UV emission.

Ultraviolet photolysis of HgBr<sub>2</sub> has been used to generate a pulsed green laser at 502 nm. The laser, which operates on the B → X transition of HgBr, was longitudinally pumped with a 4-mJ ArF laser.

Radiometric sensitivity measurements have been made on a quasi-optical receiver in the spectral range 170 μm to 1 mm. Using GaAs Schottky mixer diodes in a corner-reflector configuration, total system noise temperatures of 9680 K (DSB) have been obtained at 447 μm.

### III. MATERIALS RESEARCH

In an investigation of the feasibility of fabricating infrared photocathodes utilizing a graded-gap Hg<sub>x</sub>Cd<sub>1-x</sub>Te structure, it has been found that the rapid diffusion of Cs into CdTe precludes the use of emitting surfaces prepared by direct cesiation of CdTe. To determine whether bias-assisted, transferred-electron photoemitters can be made by the cesiation of a thin metal overlayer that forms a Schottky barrier on p-CdTe, the diffusion of Cs into a number of potentially useful metals has been investigated. For Al, Ti, and Cr, which were found to have low Cs diffusion rates, the work functions of cesiated surfaces have been determined and initial measurements have been made on the properties of Schottky barriers formed by these metals on p-CdTe.

In order to provide a single-crystal sample of CdGeP<sub>2</sub> large enough for measurement of the electrooptic coefficients, a technique has been developed for the synthesis and crystal growth of this II-IV-V<sub>2</sub> chalcopyrite. A single crystal whose size (volume ~5 cm<sup>3</sup>) and optical transmission considerably exceed the minimum requirements for the electrooptic measurements has been obtained from an ingot prepared by this technique, which uses the horizontal gradient-freeze method for directional solidification of a near-stoichiometric melt formed by reaction of the three elements in a sealed fused-silica ampoule.

#### IV. MICROELECTRONICS

Oriented crystal growth on an amorphous substrate has been achieved using an artificially created surface-relief grating. Crystallites of KCl grown from a water solution onto a 320-nm spatial-period square-wave grating in  $\text{SiO}_2$  nucleated preferentially at vertical steps and grew with  $\langle 100 \rangle$  directions parallel to the grating axis. It is proposed that artificially created surface microstructures may provide a new means of manipulating the growth and orientation of crystalline overlayers.

Reactive ion etching with  $\text{CHF}_3$  gas has been combined with plasma etching in  $\text{CH}_4 + 5\% \text{O}_2$  to produce submicrometer geometry patterns in glass films on GaAs substrates. Reactive ion etching is used to etch the glass within approximately 1000 Å of the glass/GaAs interface, and plasma etching then removes the remaining glass without damaging the GaAs substrate. Steep-edged walls and precise dimensional control have been achieved for both  $\text{SiO}_2$  on GaAs and phosphosilicate glass/ $\text{Si}_3\text{N}_4$  on GaAs with this technique.

#### V. SURFACE-WAVE TECHNOLOGY

Surface-acoustic-wave properties of fresnoite have been calculated from bulk material parameters and have been measured along several orientations on samples cut from Czochralski grown crystals. Favorable properties are measured for the z-cut, x-propagating wave: the coupling coefficient,  $k^2$ , is  $0.016 \pm 0.003$ , the velocity is 2678 m/sec, and the temperature coefficient of delay is  $51 \times 10^{-6}/^\circ\text{C}$ . These values, as well as those measured for the much lower coupling x-z and x-y surface waves, are in agreement with calculations. The calculations also predict that for surface waves propagating in the x direction on a surface whose normal is at  $45^\circ$  to z and y axes, the coupling coefficient is 10 percent higher than calculated for the above z-x case.

The mode structure of acoustic waves propagating in gap-coupled acoustoelectric convolvers has been theoretically analyzed. When a silicon strip is supported above a  $\text{LiNbO}_3$  surface by a structure consisting of parallel rails, these rails strongly influence the surface-wave propagation. Rail support structures have been modeled as a periodically loaded transmission line. The loading caused by rails has been calculated as a function of rail width and spacing. Mode profiles and beat lengths between modes have been predicted and they agree well with experimental measurements.

REPORTS ON SOLID STATE RESEARCH

15 November 1977 through 15 February 1978

PUBLISHED REPORTS

Journal Articles

<u>JA No.</u>			
4034	Far-Infrared Photoconductivity in High Purity GaAs	G. E. Stillman C. M. Wolfe J. O. Dimmock	Chapter 4 in <u>Semiconductors and Semimetals, Vol. 12, Infrared Detectors</u> (Academic Press, New York, 1977), pp. 169-288
4353	Brillouin Scattering in Semiconductors	A. S. Pine	Chapter 6 in <u>Topics in Applied Physics, Volume 8: Light Scattering in Solids</u> , M. Cardona, Ed. (Springer-Verlag, Heidelberg, 1975), pp. 253-273
4486	Surface Wave Device Fabrication	H. I. Smith	Chapter 4 in <u>Surface Wave Filters</u> , edited by H. Matthews (Wiley, New York, 1977), pp. 165-217
4505	Reflection Grating Filters	R. C. Williamson	Chapter 9 in <u>Surface Wave Filters</u> , edited by H. Matthews (Wiley, New York, 1977), pp. 381-442
4653	Tunable Infrared Laser Sources for Optoacoustic Spectroscopy	P. L. Kelley	In <u>Optoacoustic Spectroscopy and Detection</u> (Academic Press, New York, 1977), pp. 113-131
4739	Measured Compositions and Laser Emission Wavelengths of $\text{Ga}_x\text{In}_{1-x}\text{As}_y\text{P}_{1-y}$ LPE Layers Lattice-Matched to InP Substrates	J. J. Hsieh	J. Electron. Mater. <u>7</u> , 31 (1978)
4741	Phase Studies, Crystal Growth, and Optical Properties of $\text{CdGe}(\text{As}_{1-x}\text{P}_x)_2$ and $\text{AgGa}(\text{Se}_{1-x}\text{S}_x)_2$ Solid Solutions	J. C. Mikkelsen, Jr. H. Kildal	J. Appl. Phys. <u>49</u> , 426 (1978)
4754	Polarized Vibrational Raman Scattering Lineshape Parameters in Liquid CO and Liquid CO Mixtures	S. R. J. Brueck	Chem. Phys. Lett. <u>53</u> , 273 (1978)
4756	Thermal Expansion and Seeded Bridgman Growth of $\text{AgGaSe}_2$	G. W. Iseler	J. Cryst. Growth <u>41</u> , 146 (1977)

JA No.

- |      |   |   |  |
|------|---|---|--|
| 4775 | Chemisorbed Phases of H <sub>2</sub> O on TiO <sub>2</sub> and SrTiO <sub>3</sub>   | V. E. Henrich<br>G. Dresselhaus<br>H. J. Zeiger   | Solid State Commun. <u>24</u> , 623 (1977) |
| 4777 | Surface Relief Structures with Linewidths Below 2000 Å  | D. C. Flanders<br>H. I. Smith<br>H. W. Lehmann*<br>R. Widmer*<br>D. C. Shaver*                | Appl. Phys. Lett. <u>32</u> , 442 (1978)   |
| 4780 | Effect of O <sub>2</sub> Pressure During Deposition on Properties of rf-Sputtered Sn-Doped In <sub>2</sub> O <sub>3</sub> Films                     | J. C. C. Fan<br>F. J. Bachner<br>G. H. Foley  | Appl. Phys. Lett. <u>31</u> , 773 (1977)   |
| 4785 | Infrared Four-Wave Sum and Difference Frequency Generation in Liquid CO-O <sub>2</sub> Mixtures   | H. Kildal<br>S. R. J. Brueck  | Appl. Phys. Lett. <u>32</u> , 473 (1978)   |
| 4792 | Crystal Structure and Ionic Conductivity of Li <sub>14</sub> Zn(GeO <sub>4</sub> ) <sub>4</sub> and Other New Li <sup>+</sup> Superionic Conductors | H. Y-P. Hong  | Mater. Res. Bull. <u>13</u> , 417 (1978)   |
| 4798 | Surface Acoustic Wave Properties of Fresnoite, Ba <sub>2</sub> Si <sub>2</sub> TiO <sub>8</sub>   | J. Melngailis<br>J. F. Vetelino*<br>A. Jhunjhunwala*<br>T. B. Reed<br>R. E. Fahey<br>E. Stern | Appl. Phys. Lett. <u>32</u> , 203 (1978)   |

Meeting Speeches

MS No.

- |       |                               |              |  |
|-------|-------------------------------|--------------|--|
| 4067C | Tunable Semiconductor Lasers  | A. Mooradian | In <u>Nonlinear Optics</u> (Academic Press, New York, 1977), p. 243  |
| 4177  | Wavelength-Selective Surfaces | J. C. C. Fan | Chapter 8 in <u>Advances in Chemistry Series, No. 163: Solid State Chemistry of Energy Conversion and Storage</u> , J. B. Goodenough and M. S. Whittingham, Eds. (American Chemical Society, New York, 1977), pp. 149-164  |
| 4178  | New Solid Electrolytes        | H. Y-P. Hong | Chapter 10 in <u>Advances in Chemistry Series, No. 163: Solid State Chemistry of Energy Conversion and Storage</u> , J. B. Goodenough and M. S. Whittingham, Eds. (American Chemical Society, New York, 1977), pp. 179-194 |

\* Author not at Lincoln Laboratory.

<u>MS No.</u>			
4271	X-Ray Lithography	H. I. Smith D. C. Flanders	Jap. J. Appl. Phys. <u>16</u> , Suppl. 16-1, 64 (1977)
4383	Studies of Defect Surface States on SrTiO <sub>3</sub> Photoelectrolytic Electrodes	J. G. Mavroides V. E. Henrich H. J. Zeiger G. Dresselhaus J. A. Kafalas D. F. Kolesar	In <u>Proceedings, Symposium on Electrode Materials and Storage</u> , Philadelphia, 8-13 May 1977, Vol. 77-6 (The Electrochemical Society, Inc., Princeton, New Jersey, 1977), pp. 45-53
4433	Growth of Ni-Doped MgF <sub>2</sub> Crystals in Self-Sealing Graphite Crucibles	T. B. Reed R. E. Fahey P. F. Moulton	J. Cryst. Growth <u>42</u> , 569 (1977)
4480A	A New Signal Processing Device, the Integrating Correlator	R. W. Ralston D. H. Hurlburt F. J. Leonberger J. H. Cafarella E. Stern	<u>1977 Ultrasonics Symposium Proceedings</u> (IEEE, New York, 1977), pp. 623-628
4501	X-ray Replication of Submicrometer Linewidth Patterns	H. I. Smith D. C. Flanders	Proc. 35th Annual Mtg. EMSA, Boston, 22-26 August 1977, pp. 136-137
4545	Filter with Bandwidth Continuously Variable from 5 to 100 MHz	J. Melngailis R. C. Williamson R. H. Domnitz*	<u>1977 Ultrasonics Symposium Proceedings</u> (IEEE, New York, 1977), pp. 965-968
4547	Acoustoelectrically Scanned Gap-Coupled Si-Diode Array/LiNbO <sub>3</sub> Imaging Devices	F. J. Leonberger J. H. Cafarella R. W. Ralston E. Stern A. L. McWhorter	<u>1977 Ultrasonics Symposium Proceedings</u> (IEEE, New York, 1977), pp. 456-459
4549	Improved Acoustoelectric Schottky-Diode/LiNbO <sub>3</sub> Memory Correlator	R. W. Ralston J. H. Cafarella S. A. Reible E. Stern	<u>1977 Ultrasonics Symposium Proceedings</u> (IEEE, New York, 1977), pp. 472-477
4560	Case Studies of Successful Surface-Acoustic-Wave Devices	R. C. Williamson	<u>1977 Ultrasonics Symposium Proceedings</u> (IEEE, New York, 1977), pp. 460-468

UNPUBLISHED REPORTS

Journal Articles

<u>JA No.</u>			
4710	Micro Fresnel Zone Plates for Coded Imaging Applications	N. M. Ceglie* H. I. Smith	Accepted by Rev. Sci. Instrum.

\* Author not at Lincoln Laboratory.

JA No.			
4746	Spectroscopy and Lasing of a High Nd Concentration Al-Phosphate Glass	A. Lempicki* R. M. Klein* S. R. Chinn	Accepted by IEEE J. Quantum Electron.
4755	Doppler-Limited Spectra of the C-H Stretching Fundamentals of Formaldehyde	A. S. Pine	Accepted by J. Mol. Spectrosc.
4786	Collisionless Intramolecular Energy Transfer in Vibrationally Excited SF <sub>6</sub>	T. F. Deutsch S. R. J. Brueck	Accepted by Chem. Phys. Lett.
4790	Wavelength Dependence of GaAs Directional Couplers and Electrooptic Switches	F. J. Leonberger J. P. Donnelly C. O. Bozler	Accepted by Appl. Opt.
4799	Ultraviolet Photoemission Measurements of the Band Structure of TiO <sub>x</sub> (0.93 ≤ x ≤ 1.15)	V. E. Henrich H. J. Zeiger T. B. Reed	Accepted by Phys. Rev. B
4801	Efficient Phasematched Infrared Third Harmonic Generation in Liquid CO-O <sub>2</sub> -SF <sub>6</sub> Mixtures	S. R. J. Brueck H. Kildal	Accepted by Opt. Lett.
4802	Simplified Fabrication of GaAs Homojunction Solar Cells with Increased Conversion Efficiencies	J. C. C. Fan C. O. Bozler R. L. Chapman	Accepted by Appl. Phys. Lett.
4808	GaInAsP/InP Avalanche Photodiodes	C. E. Hurwitz J. J. Hsieh	Accepted by Appl. Phys. Lett.
4810	Oriented Crystal Growth on Amorphous Substrates Using Artificial Surface Relief Gratings	H. I. Smith D. C. Flanders	Accepted by Appl. Phys. Lett.
MS-4437	Alignment of X-ray Lithography Masks Using a New Interferometric Technique - Experimental Results	S. A. Austin* D. C. Flanders H. I. Smith	Accepted by J. Vac. Sci. Technol.
MS-4438	Polyimide Membrane X-ray Lithography Masks - Fabrication and Distortion Measurements	D. C. Flanders H. I. Smith	Accepted by J. Vac. Sci. Technol.
MS-4543	Chemisorbed Phases of O <sub>2</sub> on TiO <sub>2</sub> and SrTiO <sub>3</sub>	V. E. Henrich G. Dresselhaus H. J. Zeiger	Accepted by J. Vac. Sci. Technol.

---

\* Author not at Lincoln Laboratory.

JA No.

MS-4544 Surface Photovoltage Experiments on SrTiO<sub>3</sub> Electrodes J. G. Mavroides D. F. Kolesar Accepted by J. Vac. Sci. Technol.

Meeting Speeches\*

MS No.

4140F	Photoelectrolysis of Water	J. G. Mavroides	Fall Symp., McGill University, Montreal, Canada, 19 November 1977
4358A	Integrated Optics	I. Melngailis	New Technology, M.I.T., 1 February 1978
4392A	Tunable Infrared Lasers	A. Mooradian	Conf. on Lasers and Electro-optical Systems (CLEOS), San Diego, California, 7-9 February 1978
4537A	Vibrational Energy Transfer Processes in Simple Cryogenic Liquids	R. M. Osgood, Jr.	Seminar, Allied Chemical, Morristown, New Jersey, 30 November 1977
4581	The Electronic Structure of Defect Surfaces: Chemisorption on Transition-Metal Oxides	V. E. Henrich	Seminar, University of Maine, Orono, 18 November 1977
4582	Efficient Third Harmonic Generation of CO <sub>2</sub> Laser Radiation in Liquid CO-O <sub>2</sub> -SF <sub>6</sub> Mixtures	H. Kildal S. R. J. Brueck	Topical Mtg. on Inertial Confinement Fusion, San Diego, California, 7-9 February 1978
4588	Acoustically Scanned Optical Imaging Devices	F. J. Leonberger	IEEE Boston Section Group on Sonics and Ultrasonics, Bedford, Massachusetts, 7 December 1977
4592	GaInAsP/InP Avalanche Photodiodes	C. E. Hurwitz J. J. Hsieh	} Topical Mtg. on Integrated and Guided Wave Optics, Salt Lake City, 16-18 January 1978
4607	Semiconductor Waveguide Switches	F. J. Leonberger	
4612	High Sensitivity, GHz-Bandwidth HgCdTe Heterodyne Receivers	D. L. Spears	Seminar, Honeywell Electro-Optical Center, Lexington, Massachusetts, 30 November 1977

\*Titles of Meeting Speeches are listed for information only. No copies are available for distribution.

## ORGANIZATION

### SOLID STATE DIVISION

A. L. McWhorter, *Head*  
I. Melngailis, *Associate Head*  
C. R. Grant, *Assistant*  
  
R. H. Kingston  
P. E. Tannenwald

### QUANTUM ELECTRONICS

A. Mooradian, *Leader*  
P. L. Kelley, *Associate Leader*

Barch, W. E.	Fetterman, H. R.
Belanger, L. J.	Fleming, M. W.*
Blumberg, W. A. M.	Hancock, R. C.
Brueck, S. R. J.	Kildal, R.
Burke, J. W.	Menyuk, N.
Chinn, S. R.	Moulton, P. F.
DeFeo, W. E.	Osgood, R. M.
Deutsch, T. F.	Parker, C. D.
Ehrlich, D. J.	Pine, A. S.

### APPLIED PHYSICS

A. G. Foyt, *Leader*  
T. C. Haeman, *Assistant Leader*  
C. E. Hurwitz, *Assistant Leader*

Armiento, C. A.*	Leonberger, F. J.
Calawa, A. R.	Lind, T. A.
Carter, F. B.	McBride, W. F.
DeMeo, N. L., Jr.	Paladino, A. E.
Diadiuk, V.*	Plonko, M. C.
Donnelly, J. P.	Shen, C. C.
Duffy, P. E.	Spears, D. L.
Ferrante, G. A.	Tsang, D. Z.*
Glasser, L. A.*	Walpole, J. N.
Groves, S. H.	

### ELECTRONIC MATERIALS

A. J. Strauss, *Leader*  
H. J. Zeiger, *Associate Leader*

Anderson, C. H., Jr.	Kafalas, J. A.
Bayard, M. L.	Kolesar, D. F.
Button, M. J.	Krohn, L., Jr.
Chapman, R. L.	LaFleur, W. J.
Davis, F. M.	Mastromattei, E. L.
Delaney, E. J.	Mavroides, J. G.
Fahey, R. E.	Mroczkowski, I. H.
Fan, J. C. C.	Owens, E. B.
Feldman, B.	Palm, B. J.
Finn, M. C.	Pantano, J. V.
Gay, R. R.*	Smith, D. D.
Henrich, V. E.	Tchernev, D. I.
Hong, Y. Y-P.	Tracy, D. M.
Hsieh, J. J.	Vohl, P.
Iseler, G. W.	

### SURFACE WAVE TECHNOLOGY

E. Stern, *Leader*  
R. C. Williamson, *Associate Leader*

Baker, R. P.	Kernan, W. C.
Brogan, W. T.	Melngailis, J.
Cafarella, J. H.	Ralston, R. W.
Dolat, V. S.	Reible, S. A.
Efremow, N., Jr.	Schulz, M. B.
Holtham, J. H.	Slattery, R. L.
Hurlburt, D. H.	

### MICROELECTRONICS

W. T. Lindley, *Leader*  
F. J. Bachner, *Associate Leader*  
H. I. Smith, *Assistant Leader*

Alley, G. D.	Gray, R. V.
Beatrice, P. A.	Hansell, G. L.*
Bozler, C. O.	Hawryluk, A. M.*
Burke, B. E.	Lincoln, G. A., Jr.
Chiang, A. M.	McGonagle, W. H.
Clifton, B. J.	Mountain, R. W.
Clough, T. F.	Murphy, R. A.
Daniels, P. J.	Pichler, H. H.
DeGraff, P. D.	Shaver, D. C.*
Durant, G. L.	Silversmith, D. J.
Felton, B. J.	Smythe, D. L., Jr.
Flanders, D. C.†	Wilde, R. E.
Grant, L. L.	

\* Research Assistant

† Staff Associate

## I. SOLID STATE DEVICE RESEARCH

### A. 12-ELEMENT, 1.4-GHz BANDWIDTH HgCdTe HETERODYNE ARRAYS

A 12-element, 1.4-GHz bandwidth HgCdTe photodiode array designed for rapid target acquisition for a CO<sub>2</sub> laser radar has been developed with measured individual element heterodyne sensitivities better than  $7 \times 10^{-20}$  W/Hz at 760 MHz. The 0.5-mm-diameter planar structure consists of a central quadrantal array surrounded by eight additional photodiodes. RF crosstalk between elements was found to be less than -22 dB at 1.4 GHz. Two factors which contributed to successful array fabrication were a change in the junction diffusion parameters and the development of the new lead bonding technique, reported previously.<sup>1</sup>

The In-Hg diffusion parameters were changed from the 30 min. at 240°C, used previously in the planar fabrication process,<sup>2</sup> to 45 min. at 260°C. The lower temperature was apparently very near the stoichiometric balance conditions of HgCdTe under Hg saturation, and as a result, stoichiometric material conversion from p-type conductivity to n-type conductivity was specimen dependent and not reliable, which led to very poor device yields. In the past five diffusion runs at 260°C, twenty-nine out of a possible thirty-nine 12-element arrays were visually good, and all the approximately 200 photodiodes tested had a uniform photoresponse, indicating a reasonably uniform n-type conversion. Fourteen 12-element arrays have been bonded and partially tested to date, and nearly all have shown uniform quantum efficiencies at 10.6 μm ranging from 50 to 63 percent uncoated. Typical diode forward impedances ranged from 10 to 20 ohms (somewhat higher than some of the previous quadrantal array diodes<sup>2</sup>), and typical reverse impedances ranged from 200 to 1000 ohms. On the basis of these low frequency measurements, two arrays were selected for extensive high-frequency evaluation. The importance of these measurements and details of the techniques have been discussed previously.<sup>3,4</sup> One array, whose performance is given below, was slightly more uniform and had about 17 percent better heterodyne sensitivity than the other.

In Fig. 1-1 are shown CO<sub>2</sub> laser raster scan sensitivity profiles of the HgCdTe photodiode array with all 12, the outer 8, the inner 4, and diagonal quadrants connected. The diodes were reverse-biased and loaded down with 50 ohms. The central flat portions of the response profiles correspond to 55-percent quantum efficiency for these uncoated devices. It should be noted that the dead space within the inner quadrantal array is almost zero, yet all the diodes are clearly isolated from each other. This results from the long (~20 μm) electron diffusion length in the material at 77 K. The forward impedance of these 12 diodes ranged from 14 to 17 ohms, the reverse impedance of the outer 8 ranged from 160 to 400 ohms, and from 400 to 900 ohms for the inner 4.

RF isolation was measured by feeding an RF signal into one of the diodes and measuring the crosstalk on the other diodes. In Fig. 1-2 is shown the RF isolation as a function of frequency for representative cases, inner to outer diode within a quadrant (1-2), adjacent outer diodes (1-12), and adjacent inner diodes (2-5). Diode combinations of the same symmetry exhibited almost identical isolation vs frequency curves, e.g., isolation for the 3-4 combination was the same as for the 1-12 combination shown in Fig. 1-2. In all cases the isolation was better than 22 dB at 1.4 GHz. The dominant source of crosstalk was in the unshielded portion of the lead ribbons and chip package, estimated to be 5 to 10 dB higher than the crosstalk associated with the junction boundaries.

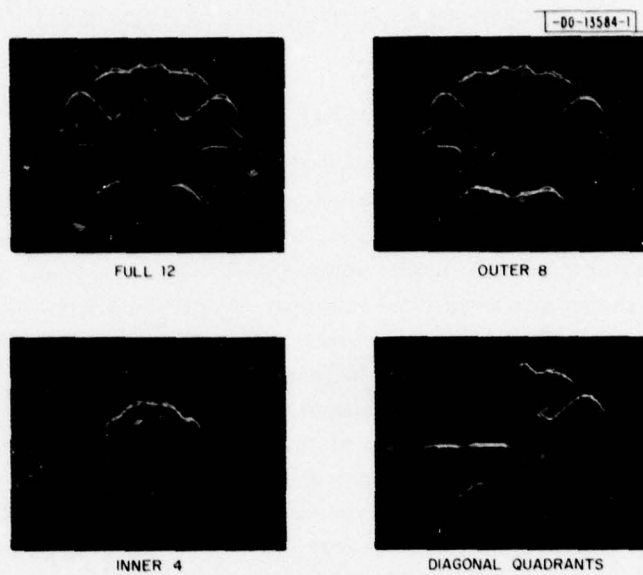


Fig. I-1. CO<sub>2</sub> laser raster scan sensitivity profiles of a 550- $\mu$ m-diameter, 12-element HgCdTe photodiode array.

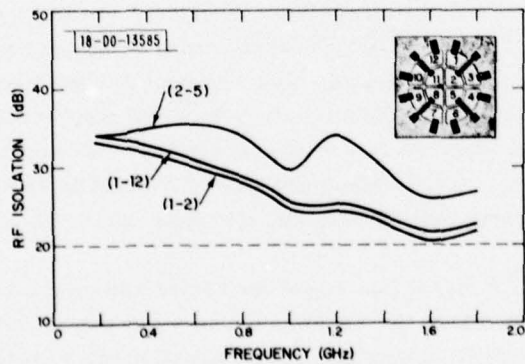


Fig. I-2. RF isolation as a function of frequency for three representative photodiode combinations in a HgCdTe 12-element array.

TABLE I-1 RELATIVE HETERODYNE SIGNAL POWER ( $P_{IF}$ ) AND EFFECTIVE HETERODYNE QUANTUM EFFICIENCY ( $\eta_{EH}$ ) IN A HgCdTe ARRAY				
Diode No.	760 MHz		1500 MHz	
	$P_{IF}$	$\eta_{EH}$ (percent)	$P_{IF}$	$\eta_{EH}$ (percent)
1	10.0	32 ± 2	9.3	17 ± 1
2	10.5	34	8.7	17
3	9.0	31	7.5	15
4	10.0	31	8.4	17
5	10.5	32	9.5	18
6	9.0	30	8.7	17
7	9.5	31	8.2	16
8	9.5	31	8.5	18
9	9.5	30	8.9	18
10	8.2	29	7.5	16
11	9.0	30	8.8	17
12	8.2	30	7.7	16

Blackbody heterodyne radiometry<sup>3-5</sup> was used to determine the heterodyne sensitivity of each element of the array at 760 and at 1500 MHz. Each measurement was carried out with the diodes reverse-biased at 0.4 V and illuminated by a 0.5-mW  $t/5$  CO<sub>2</sub> (P-20) laser local oscillator producing 2.3 mA of photocurrent. Knowing the blackbody temperature, the IF bandwidth, and the post detection integration time, the effective heterodyne quantum efficiency of the receiver (i.e., detector and preamplifier) can be determined by comparing the observed signal-to-noise ratio to that calculated for an ideal heterodyne receiver.<sup>3-5</sup> In Table I-1 are listed the measured relative heterodyne signal levels and effective heterodyne quantum efficiencies at 760 and 1500 MHz for the 12 elements (see Fig. I-2 for the diode numbering scheme). Signal-to-noise ratio is proportional to the effective heterodyne quantum efficiency ( $\eta_{EH}$ ). The uniformity over the array is quite good, showing a variation of only ±12 percent (0.5 dB) in signal and a variation of only ±6 percent (0.25 dB) in sensitivity at both frequencies. The variation in signal is due primarily to variations in RF impedance matching, not current responsivity. The 31-percent average  $\eta_{EH}$  (corresponding to a heterodyne sensitivity of  $6 \times 10^{-20}$  W/Hz at 760 MHz) is very close to the best value observed to date (36 percent) for devices without AR-coatings, and is over three times that reported for a single device made elsewhere.<sup>5</sup>

Uniformity of the photodiodes at high frequencies was measured by scanning the array with a focused, amplitude-modulated CO<sub>2</sub> beam. Figure I-3 shows DC and 0.5-GHz sensitivity profiles for three representative array elements biased at 0.4 V. The 0.5-GHz scans show the same general uniformity as the DC scans. However, the active area of the devices are slightly smaller (about 15 percent) at 0.5 GHz than at DC. This is not too surprising as the lifetime-limited diffusion length of the optically excited electron is estimated to be about 20  $\mu$ m, but only

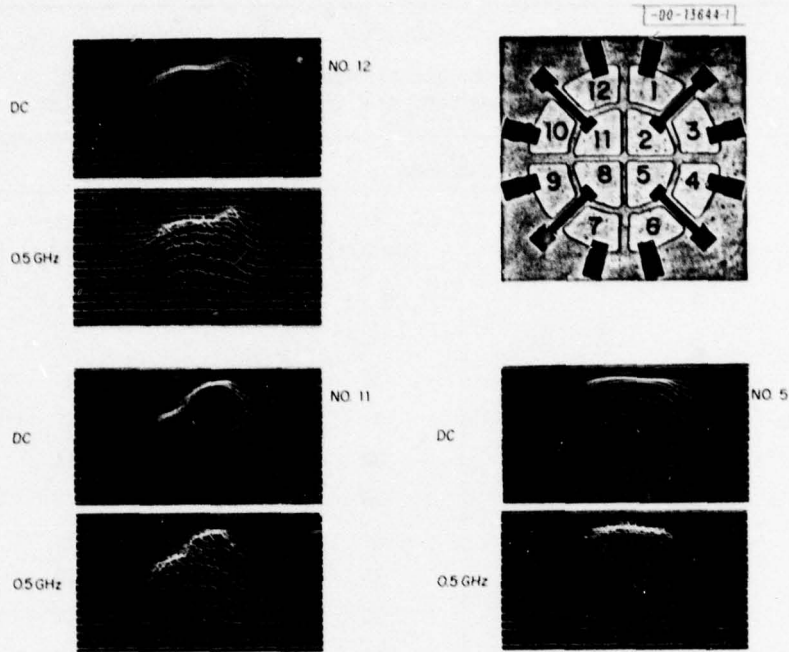


Fig. I-3. CO<sub>2</sub> laser raster scan profiles at DC and at 0.5 GHz for three elements of a 12-element HgCdTe photodiode array.

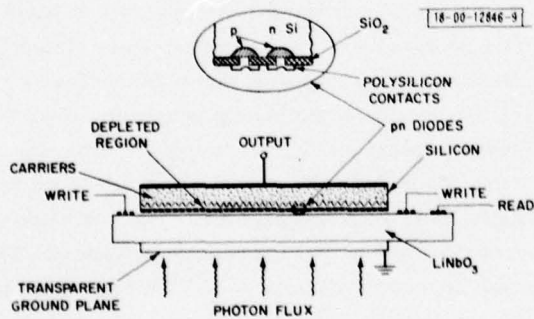


Fig. I-4. Schematic cross section of acoustically scanned optical imager. An array of either pn diodes, as shown in the magnified view, or Schottky barrier diodes is used.

optically excited electrons produced within about 10  $\mu\text{m}$  of the junction will respond at 0.5 GHz. From the data in Figs. I-1 and -3, it is estimated that the dead space at 0.5 GHz is about 15 percent within the 550- $\mu\text{m}$  diameter of the 12-element array and less than half that much within the 290- $\mu\text{m}$  diameter of the central quadrantal array.

This planar heterodyne array technology should be scalable to at least one more ring of detectors (a total of 28 elements), as material uniformity and fabrication (bonding) yield do not appear to present any immediate limitations. RF crosstalk due to the close proximity of the bonding leads, however, will be a major factor. The quadrantal arrays,<sup>2</sup> which had bonding pads spaced 180  $\mu\text{m}$  apart and leads separated by 90°, exhibited about 30-dB isolation at 1.4 GHz; the 12-element arrays, with pads spaced 100  $\mu\text{m}$  apart and leads separated by 30°, exhibited 22-dB isolation at 1.4 GHz. It is estimated that for a 28-element array with pads spaced 70- $\mu\text{m}$  apart and leads separated by 13°, the RF isolation will be only 10 to 15 dB at 1.4 GHz. Dead space due primarily to crossover of inner device leads also increases with each additional ring of detectors. In the first ring there was about 20-percent dead space between the 8 detectors. It is estimated that the second ring would have about 33-percent dead space between the 16 detectors and a third ring would have over 50-percent dead space between those 32 diodes. Such losses in signal collection and isolation would quickly defeat the purpose of a large number of array elements. The central quadrantal array plus two additional rings of photodiodes (a total of 28 elements) may be the optimum geometry for a 1.4-GHz bandwidth.

We are in the process of improving the sensitivity and RF isolation of these devices by AR-coating the diodes and modifying the RF package. Zinc sulfide AR-coatings have improved the low-frequency quantum efficiencies from the 50- to 63-percent range to the 75- to 90-percent level. Effective heterodyne quantum efficiencies at 760 MHz have been observed in the 45- to 50-percent range for several single AR-coated photodiodes.

D. L. Spears  
C. D. Hoyt

## B. ACOUSTICALLY SCANNED Si-DIODE ARRAY/LiNbO<sub>3</sub> OPTICAL IMAGING DEVICES

The development of new types of solid state optical imaging devices is an area of continuing interest. Recently, the use of a gap-coupled Si-diode array/LiNbO<sub>3</sub> acoustoelectric memory correlator as an optical imaging device was reported.<sup>6,7</sup> Our investigation of this new imager has centered on studying the operational principles of the device. In this report we demonstrate that this device can be operated as a linear imager and at a scan rate compatible with real-time imaging systems. Similar results have been obtained using both pn and Schottky diode arrays. The device structure and operation is described and its charging characteristics and optical response discussed.

### 1. Device Structure and Operation

A schematic diagram of the imager is shown in Fig. I-4. The device consists of a Si strip, approximately 1.7  $\times$  35 mm<sup>2</sup>, containing a planar high-density array of either pn or Schottky diodes separated from a LiNbO<sub>3</sub> delay line by a ~0.35- $\mu\text{m}$  gap. The gap is maintained with a pseudorandom array of 6- $\mu\text{m}$ -diameter and 0.35- $\mu\text{m}$ -high posts that are ion-etched in the LiNbO<sub>3</sub> surface. Details of the package for this device are given in Ref. 8. The pn diode arrays are unthinned 150- $\mu\text{m}$ -thick commercial vidicon targets. The diodes have a 13- $\mu\text{m}$  center-to-center

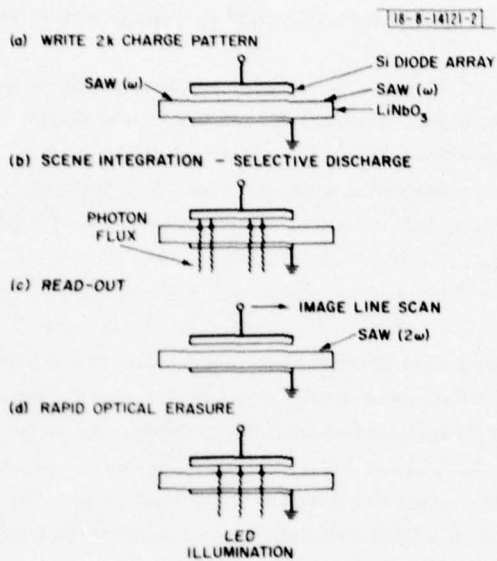
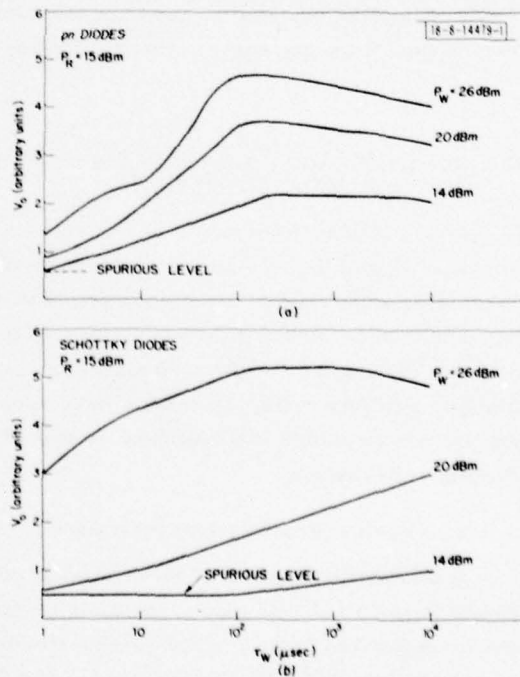


Fig. I-5. Sequence for imager operation.

Fig. I-6. Charging characteristics for (a) pn and (b) Schottky diode arrays with writing power  $P_W$  as parameter.



spacing and are formed on 50- $\Omega$ -cm n-type substrates. The p-type islands are about 2  $\mu\text{m}$  thick. The diodes have a 10- $\mu\text{m}$ -diameter p-type polysilicon overlay covering 5- $\mu\text{m}$ -diameter holes in a  $\text{SiO}_2$  film, as shown in the enlarged diagram in the figure. These overlays form annular MOS diodes over each junction. The Schottky diode arrays are identical to those described by Ralston *et al.*<sup>9</sup> They consist of rows of lozenge-shaped PtSi barriers with a 3.8- $\mu\text{m}$  center-to-center spacing in the direction of acoustic power flow formed on 20- $\Omega$ -cm n-type substrates. Light is incident on the Si diodes through the  $\text{LiNbO}_3$  and a transparent ground plane (formed by a thin film structure of  $\text{TiO}_2$ -Ag- $\text{TiO}_2$  with each layer 180  $\text{\AA}$  thick) on the back of the  $\text{LiNbO}_3$ . As will be discussed below, the write and read transducers are used to store a charge pattern in the diode array and read out the image, respectively.

The scheme of imager operation we used is detailed in Fig. 1-5. As shown in Fig. 1-5(a), two counterpropagating surface waves at frequency  $\omega$  and wavenumber  $k$  are used to form a charge grating of  $2k$  spatial frequency.<sup>10</sup> Here the diodes can be considered part of a peak detector circuit driven by the standing wave created by the two surface waves. The diodes build up a reverse-bias charge logarithmically with time, as will be discussed below. For our case, the writing signal consisted of a series of 5- $\mu\text{sec}$ , 70-MHz pulses with a 25- $\mu\text{sec}$  period. A series of pulses was used to eliminate the interference effects obtained with one long pulse due to reflection of the leading edge of the pulse from the transducer at the far end of the delay line. As shown in Fig. 1-5(b), the photon flux from the scene selectively discharges the  $2k$  grating during the scene integration time, which typically ranged from 20 to 50 msec. For all the data shown in this report, a spectrometer served as a light source, and a wavelength  $\lambda$  of 0.65  $\mu\text{m}$  used. The remaining charge is then read out nondestructively from the Si back contact at  $(2\omega, 0k)$  with a short surface wave pulse at the  $2\omega$  frequency, as illustrated in Fig. 1-5(c). In this scheme, the width of this pulse determines the spatial resolution of the imager. For our case, 0.5- to 1- $\mu\text{sec}$  pulses at 140 MHz were used (i.e., 1.5- to 3-mm resolution). Finally, the residual charge is rapidly erased by an optical pulse from an array of light-emitting diodes (LEDs) positioned near the imager as shown in Fig. 1-5(d). This pulse was typically 60  $\mu\text{sec}$  long and of sufficient optical power to fully discharge the  $2k$  pattern in the absence of light from the imaged scene. The pulse is generally applied 200  $\mu\text{sec}$  to 1 msec prior to the next writing sequence. Both red and green LEDs have been successfully utilized. This erasure was necessary to eliminate image lag effects that were otherwise found to occur and which rendered the device unsuitable for dynamic imaging applications.

## 2. Charging Characteristics

The charging characteristics of these devices are shown in Fig. 1-6. Figure 1-6(a) shows the results for a pn array. The device output voltage  $V_o$  is plotted vs the logarithm of the total writing time  $\tau_w$  (i.e., the time sum of the series of 5- $\mu\text{sec}$  writing pulses) over the range of writing power from 14 to 26 dBm. For the data shown, as well as for the other data presented here,  $V_o$  was measured at a time when the read pulse was at the position along the array where the counterpropagating writing waves first meet. This minimizes uniform charging effects caused by the traveling surface waves.<sup>10</sup> For this experiment, the read pulse was a 15-dBm, 1- $\mu\text{sec}$  pulse applied 100  $\mu\text{sec}$  after the end of the charging period. For each writing power level, the output signal (with the exception of the 26-dBm signal in the 5- to 15- $\mu\text{sec}$  range) increases logarithmically with time for the first 100  $\mu\text{sec}$ , at which point the signal saturates

and finally decreases slightly at charging times approaching  $10^4 \mu\text{sec}$ . The storage time for these devices was typically  $\sim 2 \text{ sec}$  for charging times of  $25 \mu\text{sec}$  at  $26 \text{ dBm}$ . At each writing power level, these storage times increased monotonically with increased charging time, suggesting that the saturation in the  $2\text{k}$  signal could result from the buildup of a uniform charge on the diodes and a reduction in the acoustoelectric writing and reading efficiency. The small signal decrease for  $\tau_W \gtrsim 100 \mu\text{sec}$  in particular could be attributed to a decrease in the acoustoelectric coupling due to the uniformly wider depletion layer. The results for the Schottky barrier array are shown in Fig. I-6(b). Here, only the  $26\text{-dBm}$  curve exhibits a saturation, while the  $20\text{-}$  and  $14\text{-dBm}$  curves appear logarithmic through  $\tau_W = 10^4 \mu\text{sec}$ . For these Schottky barrier devices, storage time also increased monotonically with charging time, with a maximum  $\sim 140 \text{ msec}$  for  $400\text{-}\mu\text{sec}$  charging at  $26 \text{ dBm}$ . Logarithmic charging can be explained by modeling the device as a distributed peak detector circuit. Our model, similar to one recently reported by Borden and Kino,<sup>11</sup> predicts a logarithmic dependence of  $V_O$  on time with a saturation in  $V_O$  due to full diode charging in times of  $10^5$  to  $10^6 \mu\text{sec}$ . Computer calculations indicate that the  $14\text{-}$  and  $20\text{-dBm}$  Schottky barrier charging curves are consistent within a factor of 2 in slope and magnitude with our model. However, the model does not explain the  $100\text{-}\mu\text{sec}$  saturation of the  $26\text{-dBm}$  curve, the similar saturation in the pn-diode data, or the nonlogarithmic behavior of the  $26\text{-dBm}$  curve for the pn array in the  $5\text{-}$  to  $15\text{-}\mu\text{sec}$  range. It should be noted that if charging is done without a LED erasure, the saturation in  $V_O$  occurs at an earlier time but at about the same signal level. For the pn arrays, this time is typically  $10 \mu\text{sec}$ . This rapid charging is similar to that reported by other workers<sup>7,10</sup> and is apparently caused by frame-to-frame effects.

### 3. Imaging Characteristics

The importance of an optical erasure for imaging applications is illustrated in Fig. I-7. Here we show results of an experiment in which light incident on a pn-diode imager is mechanically chopped at a  $40\text{-msec}$  period, a time similar to that used in imaging applications. In this experiment, the writing and reading sequence was synchronized with the chopper. The pn arrays were charged at  $20 \text{ dBm}$  for  $50 \mu\text{sec}$  and then read with a multiple number of  $1\text{-}\mu\text{sec}$

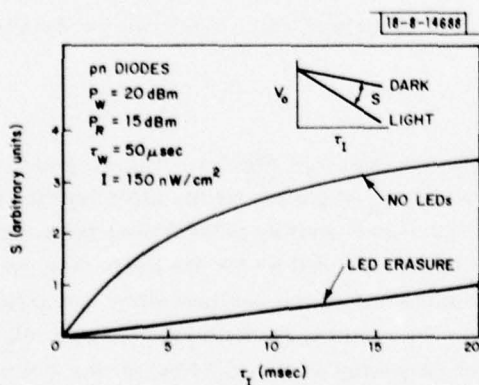


Fig. I-7. Photosignal vs integration time for pn array showing effect of LED erasure. The photosignal  $S$  is the difference in device output voltage  $V_O$  between light on and off, as indicated in the insert.

pulses to obtain oscillograms in which the signal envelope was proportional to the  $2\text{k}$  charge remaining on the device. The figure shows the photosignal  $S$  vs integration time  $\tau_I$  for the case of a uniform light intensity of  $I$  of  $150 \text{ nW/cm}^2$  and for the integration time initiated with the

start of the "light on" portion of the chopper cycle. Values of  $S$  were obtained by determining the difference in device output voltage  $V_o$  between the cases of the light blocked off and the light incident on the device. This results in a negative signal and is shown schematically in the figure insert. The data indicate that with a LED erasure a linear photoresponse is obtained. This is the expected response for reverse-biased photodiodes subjected to a constant optical generation rate as they are in this experiment (i.e., all the light absorbed generates hole-electron pairs either in or within a diffusion length of the space charge layer). If the experiment is performed without a LED erasure,  $V_o$  decays much more slowly when the light is blocked off. In addition, an exponential photoresponse, similar to that reported in Ref. 6, is obtained as shown in the figure. This response is due to image lag effects. The lag effect can be dramatically illustrated by initiating the integration time with the onset of the "light off" portion of the chopper cycle. In this case, an exponential response essentially identical to the one shown was obtained even though  $S = 0$  response should have been found, as it was when the same experiment was performed with a LED erasure. This indicates that each successive writing sequence does not fully reset the device, resulting in a higher apparent sensitivity to low light levels than is actually present. Similar effects were observed with Schottky barrier devices, but the results were not as dramatic due to their shorter storage time.

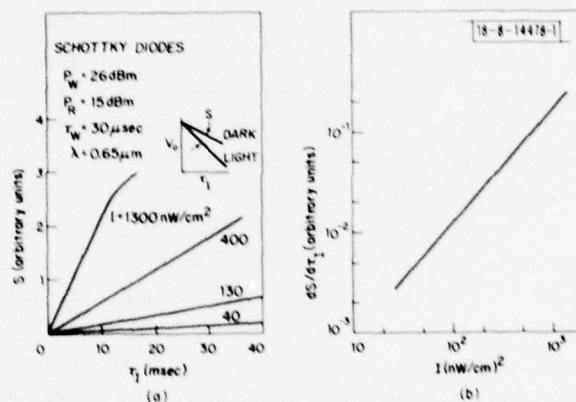


Fig. 1-8. (a) Photosignal vs integration time for Schottky array with light intensity as parameter and (b) derivative of photosignal with respect to integration time vs light intensity for data in (a), showing linearity of photoresponse.

When operated with an optical erasure, both the pn and Schottky diode devices can function as linear imagers. This is illustrated in Fig. 1-8 for the Schottky diodes. Figure 1-8(a) shows the photosignal  $S$  vs  $\tau_I$  with  $I$  as a parameter. A linear response is obtained for each value of  $I$  in the range 40 to 1300  $\text{nW/cm}^2$ . The small change in slope for the  $I = 1300 \text{ nW/cm}^2$  case for  $\tau_I > 10$  msec is not fully understood but is associated with  $V_o$  approaching the spurious level. For the case shown here, 40  $\text{nW/cm}^2$  can be detected in 15 msec; this corresponds to a sensitivity of 600  $\text{pJ/cm}^2$ . In Fig. 1-8(b) the rate of signal discharge  $dS/d\tau$  is plotted vs  $I$  for these data. The plot has a slope of  $\sim 1$ , indicating the expected linearity of the imager when it is discharged with a constant optical generation rate. Moreover, the spectral response of the devices was consistent with that expected for Si photodiodes.

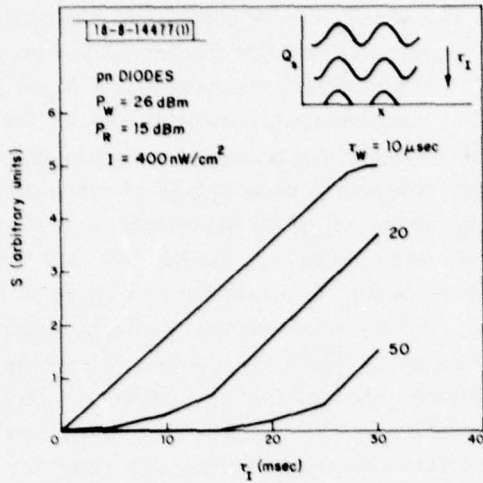


Fig. I-9. Photosignal vs integration time for pn array with writing time as parameter. The insert shows schematically the decay of a charge pattern  $Q_s$  consisting of a 2k grating and a uniform portion when subjected to a constant optical generation rate.

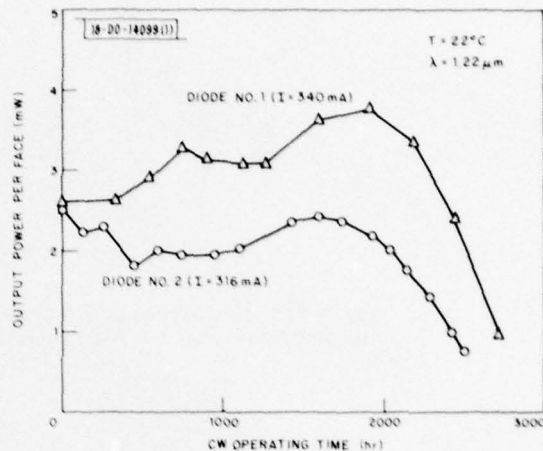
It was found that if the devices were charged to too high a level, a nonuniform photoresponse was obtained, as illustrated in Fig. I-9 for the pn arrays. Here  $S$  is plotted vs  $\tau_I$  with  $\tau_W$  as parameter for  $I = 400 \text{ nW/cm}^2$ . For a writing power of 26 dBm a linear photoresponse is obtained for  $\tau_W = 10 \mu\text{sec}$ . The departure from linearity for  $\tau_I > 27 \text{ msec}$  is due to  $V_o$  approaching the spurious level. For additional charging there is a nonlinear response that becomes more pronounced with increasing charge on the diodes, as illustrated by the  $\tau_W = 20$ - and  $50$ - $\mu\text{sec}$  curves. These responses are characterized by a slow increase of  $S$  with  $\tau_I$ , followed by an increase in  $S$  at a rate consistent with that obtained for the linear response case. The effect decreases the apparent sensitivity of the device and restricts the dynamic range for linear operation. The effect is not fully understood but could be associated with the growth of a spatially uniform reverse bias which creates an offset level for the 2k charge grating. When the light discharges the diodes, this uniform charge decays first, without strongly affecting the 2k grating as shown schematically in the figure insert. It should be recalled that only the 2k component of the stored charge is sampled by the reading signal. The interpretation of this effect is complicated by the possible decrease in acoustoelectric coupling with increasing diode bias. However, the nonlinear photoresponse can be enhanced by charging the diodes with unequal power levels in the two counterpropagating surface waves; in this case, a uniform bias level is definitely introduced. It is difficult to define the charging level that corresponds to the onset of nonlinear response because both the relevant charging time and output level vary with writing power level. For example, the results shown here can be contrasted with 20-dBm writing level results where a linear response is obtained out to  $\tau_W = 70 \mu\text{sec}$ .

To utilize these acoustically scanned imagers in practical imaging systems, it is necessary to have both good sensitivity and a large number ( $m$ ) of resolution elements per line [e.g.,  $m = 500$ , for adequate television resolution, in a 3.5-cm ( $10$ - $\mu\text{sec}$ ) imager length]. Schemes that include real-time signal processing techniques to meet these requirements are being investigated.

F. J. Leonberger    A. L. McWhorter  
 J. H. Cafarella    E. Stern  
 R. W. Ralston

### C. LIFE TESTS OF DOUBLE-HETEROSTRUCTURE GaInAsP/InP LASERS

Life tests of CW, room-temperature GaInAsP/InP double-heterostructure (DH) diode lasers have continued with a total of thirteen devices examined in some detail. Of these, three are the original lasers discussed in a previous report,<sup>12</sup> and the remaining ten are similar devices. The latter devices were operated under carefully controlled heat sink temperature ( $\pm 0.1^\circ\text{C}$ ) and current ( $\pm 2\text{ mA}$ ) conditions in the test setup described previously.



For lasers operated at room temperature with a fixed current, the typical power output as a function of operating time for two devices is shown in Fig. I-10. It is clear that, even with careful control of device current and heat sink temperature, substantial variations in output power vs time are observed prior to the device end-of-life. Comparative lifetime characteristics of the lasers are being studied by operating them CW with the current adjusted to maintain a constant output power of 2 to 4 mW per facet.

For the devices under constant current operation, the lifetime is arbitrarily defined as the operating time at which the output power drops below 1 mW. A histogram of the lifetime data so obtained on thirteen devices is shown in Fig. I-11. Lifetimes ranged from a few hundred to 7500 hours, with three devices still operating at the present time.

For most of the lasers which have failed, end-face degradation has been identified as the primary cause of failure. In fact, it was usually possible to restore the output of degraded lasers to nearly original values by rinsing the devices in a buffered HF solution. The degradation-restoration cycle could be repeated several times before the end faces became irreversibly degraded. This problem is now being investigated. Avenues of study have included:

- (1) Thorough device cleaning at several stages in the fabrication processing.  
Use of detergents, organic solvents and acid washes.
- (2) Study of different fluxes for the indium solder bond of the device to the heat sink.
- (3) Protective coatings for laser end faces.

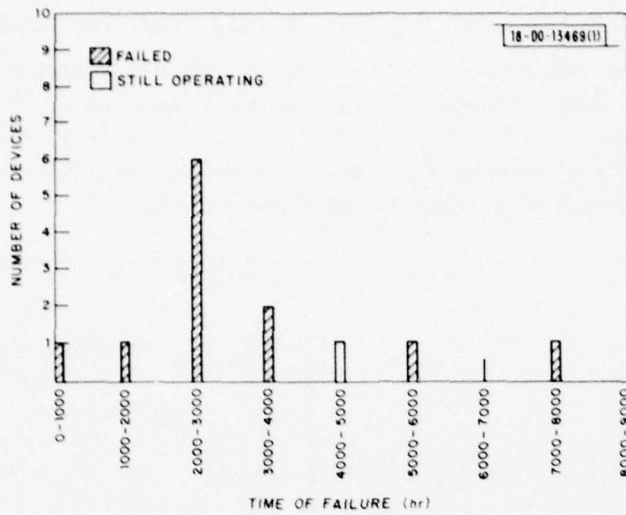


Fig. I-11. Histogram of lifetime data on thirteen GaInAsP/InP DH lasers operated CW at room temperature.

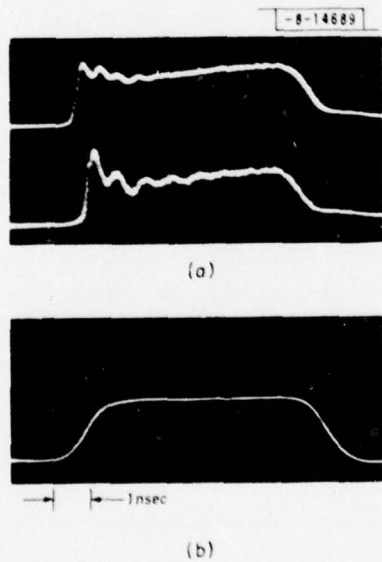


Fig. I-12. Response (a) of a germanium avalanche photodiode to the light output of a 1.22- $\mu\text{m}$  DH GaInAsP/InP laser driven by the 50-mA current pulse and (b) DC bias current through laser is 300 mA for the upper trace in (a) and 285 mA for the lower trace. Horizontal scale is 1 nsec per major division.

It appears that beneficial effects can be obtained both by the use of a sputtered  $\text{Al}_2\text{O}_3$  protective coating and by careful cleaning with an acid solution. These techniques are being evaluated in detail at present and, as a solution to the facet contamination problem is realized, studies of device lifetime and other mechanisms for degradation at both room and elevated temperatures will be investigated.

C. C. Shen  
J. J. Hsieh  
T. A. Lind

#### D. PULSE RESPONSE AND MODULATION CHARACTERISTICS OF GaInAsP/InP LASERS

Initial results of pulse response and modulation experiments on GaInAsP/InP lasers have been most encouraging. Clean, fast-risetime output pulses and 200-Mpps modulation were achieved.

The measurements were performed on stripe-geometry lasers identical to those described in a previous report.<sup>13</sup> The stripe widths and cavity lengths were 13 and 380  $\mu\text{m}$ , respectively, and the devices had threshold current densities at room temperature of about 5  $\text{kA}/\text{cm}^2$  pulsed and 6  $\text{kA}/\text{cm}^2$  CW. A bias tee arrangement was employed so that a DC bias current could be supplied simultaneously with the pulsed drive. Variable width pulses with 1-nsec rise and fall time were used in these experiments. The laser output was observed with a germanium avalanche photodiode operating into the 50-ohm input of a sampling oscilloscope.

Oscilloscope traces of the input current pulse and the detector response to the laser output are shown in Fig. I-12 for two different DC bias levels on the laser. The laser threshold current was 300 mA, so that the two bias levels of 285 and 300 mA correspond to below and just at threshold, respectively. The current pulse had an amplitude of 50 mA.

In both cases the observed risetime is approximately 250 psec, a value which is about the same as that measured by Yamamoto *et al.*<sup>14</sup> for a GaInAsP/InP laser with no DC bias. When the DC bias is well below threshold, the pulsed laser output exhibits the characteristic damped relaxation oscillation of these, as well as GaAs/AlGaAs lasers. However, when the DC bias is just below threshold, the ringing is minimized and a relatively clean output pulse is obtained as in Fig. I-12.

To determine the suitability of the lasers for pulse modulation sources, they were driven with 2-nsec pulses at 200 Mpps, as well as pairs of similar pulses to simulate 100-Mbps pulse-position modulation. The results are shown in Fig. I-13. Clearly the modulation capabilities of these lasers are well in excess of the rates used. Indeed, it has been estimated by Yamamoto *et al.*<sup>14</sup> that modulation frequencies of a few gigahertz should be achievable.

C. C. Shen  
A. G. Foyt

#### E. AUTOMATIC MEASUREMENT OF HALL COEFFICIENT AND RESISTIVITY VS TEMPERATURE

The measurement of the Hall coefficient and resistivity as a function of temperature is an important tool for semiconductor material characterization because the donor and acceptor concentrations,  $N_D$  and  $N_A$ , and the majority impurity activation energy,  $E_D$  or  $E_A$ , can be deduced from the data.<sup>15</sup> Unfortunately, these measurements are tedious and time consuming, and it is not unusual either to assign a person to operate the equipment full time or to make the

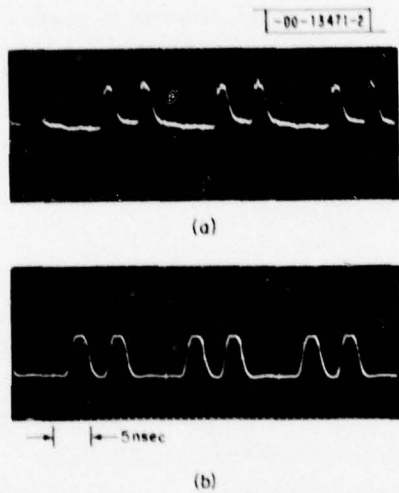


Fig. I-13. Response (a) of a germanium avalanche photodiode to the light output of a 1.22- $\mu\text{m}$  DH GaInAsP/InP laser driven by the 25-mA current pulse train (b). The laser was biased at threshold (260 mA). Time scale is 5 nsec per major division.

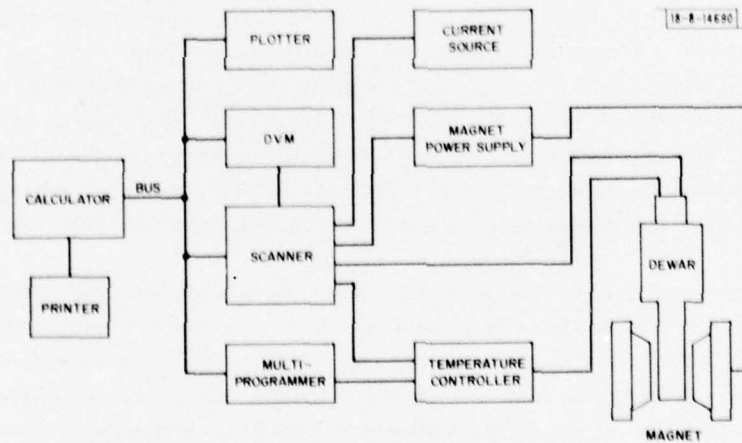


Fig. I-14. Block diagram of automatic Hall and resistivity measuring apparatus.

less desirable compromise of measuring these electrical properties at only one or two temperatures. Consequently, there is a history of efforts to introduce increasing amounts of automation into the measurements and analysis. Typically, these have involved some advanced, commercially available instrumentation and/or computation equipment supplemented by considerable apparatus of special design. Furthermore, many reports have been made of systems in which the tedious data taking or data reduction has been lessened, but the full-time presence of the operator is required to perform a switching sequence and/or to set temperatures.

We report here on highly satisfactory operation of an automatic system which has the advantages that (1) it is readily assembled from commercially available instrumentation with only relatively minor modifications necessary, (2) selections of measurement temperatures, temperature stability criteria, time delays, and measurement sequence are made from software and can easily be altered from run to run or during a run, (3) incorporation of a carbon-glass thermometer as a secondary sensor with low magnetic field dependence has made it possible to use the Si-diode-sensor type of cryogenic temperature controller, well-known for its relative convenience of use and sensitivity, and (4) a variable-temperature type of Dewar has been found suitable for a convenient mode of operation and for automatic temperature control when used with the Si-diode-sensor type of temperature controller.

Figure 1-14 shows the block layout of the system. The programmable calculator, the voltmeter, the scanner, and the multiprogrammer were purchased by us as an assembled data acquisition system. The digital voltmeter (DVM) has an input impedance of  $\sim 10^{10}$  ohms, making it useful for most semiconductor characterization. The scanner consists of switches that are remotely controlled by the calculator. The unwanted emf's introduced by the scanner switches are below  $5 \mu\text{V}$ . The multiprogrammer has two functions: (1) a serial-to-parallel, latched interface for the feeding of remote set point and gain settings from the calculator to the temperature controller and (2) a variable resistor, under calculator control, in the heater circuit, needed (as explained below) for temperature control with the magnetic field on. Our magnet supply required the minor modification of locating the "on," "reverse," and "off" switches in the scanner.

The automatic temperature setting and control was solved by using a Si-diode-sensor type of controller that was supplied with an option of 12-bit parallel inputs for remote set point and gain. In operation, the voltage-temperature calibration data for the Si-diode thermometer are stored in the calculator memory. After conversion of the desired set-point temperature to a voltage, the remote set point and gain settings are sent to the controller through the digital output cards in the multiprogrammer. A signal from the deviation meter on the temperature controller is sent to the calculator via the scanner and the DVM. A simple procedure is set up within the software to establish that the temperature has stabilized at the set point. Because of the magnetic field dependence of the Si-diode at low temperatures, it was necessary to work out a procedure for temperature control when the magnetic field is on. Carbon glass thermometers have sufficient sensitivity and low enough magnetic field dependence<sup>16</sup> to make them useful as secondary thermometers in this application. Adequate temperature control has been achieved by latching the output voltage to the heating element and then making changes in the heater current by altering a series resistor. The latching has been accomplished by inserting a long term, track and hold amplifier in series between the amplifier and the output sections of the temperature controller. The calculator-controlled resistor in series with the Dewar heater is on a resistance ladder card in the multiprogrammer. In operation, the resistance of the carbon glass

is measured at zero field after thermal stability at a desired set point has been achieved. The heater current is measured several times and the average value is stored. After the output voltage is latched, small adjustments in the series resistance are made until the latched current agrees with the stored average. The magnetic field is then applied, and temperature measurements and heater current adjustments are made after the delays of waiting for the buildup and reversal of the magnetic field. The temperature changes with the latched output are slow, and only small changes in the series resistance have been needed for our work.

The Dewar used in our system is of the variable temperature type in which a fixed flow of cold helium gas is bucked against joule heating by the heating element of the temperature controller. It is very suitable for the automatic operation when an overnight cooling procedure is used, after sample loading and liquid helium transfer. By the following morning, the sample has cooled to 4 K and the run is initiated. Our standard run, consisting of measurements made at 30 temperatures between 4 and 300 K, is made in three hours time, without need of operator attention.

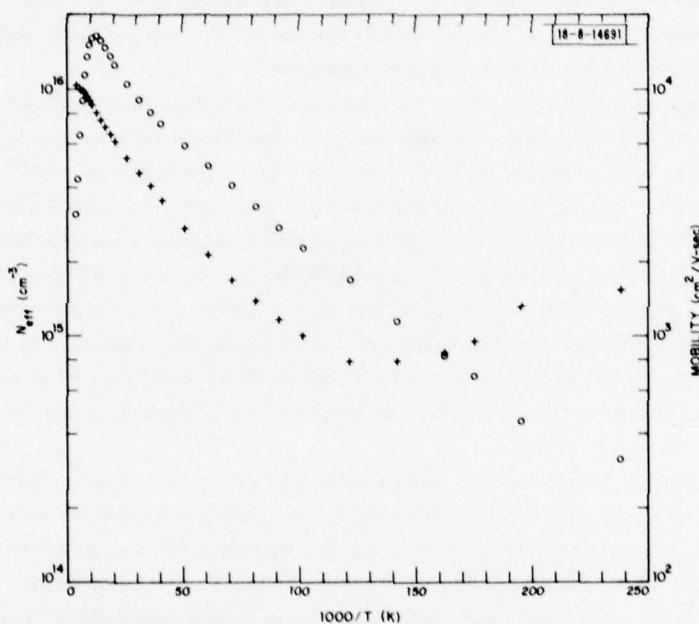


Fig. I-15. Characterization of LPE InP made on the automatic apparatus. The "+" points are  $N_{\text{eff}}$  in units of  $\text{cm}^{-3}$  and the "o" points are mobility in units of  $\text{cm}^2/\text{V}\cdot\text{sec}$ . T is in degrees Kelvin.

Figure I-15 shows results from a typical run. This apparatus is being used to characterize, among other things, liquid-phase epitaxial (LPE) growth of InP and InGaAsP alloys. The data shown in Fig. I-15 are for an LPE growth in InP, grown at  $\sim 700^\circ\text{C}$  from an indium-rich solution, where the indium is an as-received grade and the phosphorus is supplied from  $\text{PH}_3$  gas. Analysis of the data shows  $N_{\text{D}} \approx 1.8 \times 10^{16} \text{ cm}^{-3}$ ,  $N_{\text{A}} \approx 6.5 \times 10^{15} \text{ cm}^{-3}$ , and  $E_{\text{D}} \approx 0.001 \text{ eV}$ .  $N_{\text{eff}}$  is defined as  $1/R_e$ , where R is the Hall coefficient and e is the electronic charge. The criteria used for temperature control in the run permitted a maximum error in  $\Delta(1000/T) = 3(\text{K}^{-1})$  at 5 K and was much less at other temperatures.

S. H. Groves  
J. M. Lawless

#### REFERENCES

1. Solid State Research Report, Lincoln Laboratory, M.I.T. (1977:4), p. 13.
2. D. L. Spears, *Infrared Phys.* 17, 5 (1977).
3. D. L. Spears, Proceedings of Meeting of IRIS Specialty Group on Infrared Detectors, U.S. Air Force Academy, Colorado Springs, Colorado, 22-23 March 1977 (to be published).
4. Solid State Research Report, Lincoln Laboratory, M.I.T. (1976:3), p. 5, DDC AD-A034647/8.
5. B. J. Peyton, A. J. DiNardo, S. C. Cohen, J. H. McElroy, and R. J. Coates, *IEEE J. Quantum Electron.* QE-11, 569 (1975).
6. P. Defranould, H. Gautier, and C. Maerfeld, *Appl. Phys. Lett.* 29, 79 (1976).
7. W. C. Wang, K. C. Whang, and L. S. Rosenbeck, in 1976 Ultrasonics Symposium Proceedings (IEEE, New York, 1976), p. 352.
8. S. A. Reible, J. H. Cafarella, R. W. Ralston, and E. Stern, *ibid.*, p. 451.
9. R. W. Ralston, J. H. Cafarella, S. A. Reible, and E. Stern, in 1977 Ultrasonics Symposium Proceedings (IEEE, New York, 1977), p. 472.
10. See, for example, P. Defranould, H. Gautier, C. Maerfeld, and D. Tournois, in 1976 Ultrasonics Symposium Proceedings (IEEE, New York, 1976), p. 336.
11. P. Borden and G. S. Kino, *Appl. Phys. Lett.* 31, 488 (1977).
12. Solid State Research Report, Lincoln Laboratory, M.I.T. (1976:4), p. 1, DDC AD-A039175.
13. Electrooptical Devices, Semiannual Technical Summary Report to the Rome Air Development Center (31 March 1977), p. 1.
14. T. Yamamoto, K. Sakai, and S. Akiba, *Electron. Lett.* 13, 142 (1977).
15. For a review of work on one material, GaAs, see G. E. Stillman and C. E. Wolfe, *Thin Solid Films* 31, 69 (1976).
16. H. H. Sample and L. G. Rubin, *Cryogenics* 17, 597 (1977).

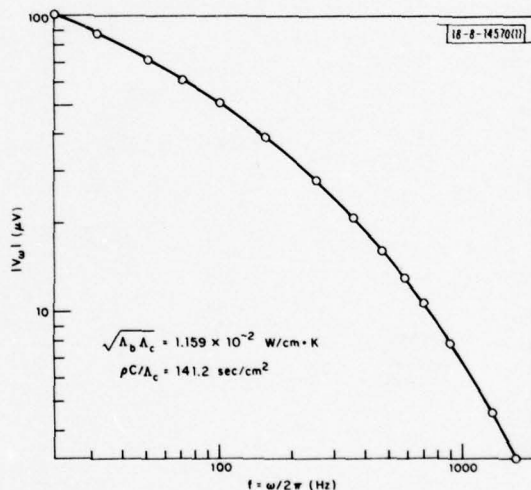
## II. QUANTUM ELECTRONICS

### A. THERMAL PROPERTIES OF $\text{Nd}_x\text{La}_{1-x}\text{P}_5\text{O}_{14}$

We have begun a series of measurements of the thermal properties of  $\text{Nd}_x\text{La}_{1-x}\text{P}_5\text{O}_{14}$  by investigating the thermal conductivity and specific heat of  $\text{NdP}_5\text{O}_{14}$ . Knowledge of these parameters is necessary in studying the feasibility of constructing CW or high-repetition-rate lasers of this material.

The method used to measure simultaneously both the thermal conductivity and specific heat is an extension of that of Bruce and Cannell.<sup>1</sup> Two parallel metal strips are fabricated on the surface of the sample. Alternating current is passed through one strip, the heater, and the temperature-induced periodic resistance variation of the other strip, the sensor, is measured as a function of the heating frequency. From the measured data, together with the electrical parameters of the heater and sensor and the temperature coefficient of sensor resistance, the thermal conductivity and specific heat can be found. Our work extends that of Ref. 1 by generalizing both the theory and measurements to include the effects of anisotropy. The case of NPP has also been simplified by the assumption of orthorhombic symmetry, since the monoclinic angle  $\beta$  in NPP deviates from  $90^\circ$  by only  $0.5^\circ$ .

Fig. II-1. Sensor voltage response, proportional to heater-induced temperature variation, as a function of heater frequency,  $f = \omega/2\pi$  (twice the applied current frequency). Open circles are data points, the solid line is best-fit theoretical curve.



Some typical data for one particular sample and crystallographic orientation are shown in Fig. II-1, along with the best-fit parameters for the thermal conductivity factor  $\sqrt{\Lambda_b \Lambda_c}$  and inverse diffusivity  $\rho C / \Lambda_c$ . Analysis of the data from other samples gives the value of the thermal conductivity tensor elements (in  $\text{W/cm}\cdot\text{K}$ )  $\Lambda_a = 2.10 \times 10^{-2}$ ,  $\Lambda_b = 9.66 \times 10^{-3}$ , and  $\Lambda_c = 1.40 \times 10^{-2}$ . The specific heat is  $0.141 \text{ cal/g}\cdot\text{K}$ , in excellent agreement with the value of  $0.139 \text{ cal/g}\cdot\text{K}$  that we measured by differential scanning calorimetry.

The thermal conductivity in NPP is considerably smaller than that of Nd:YAG,  $0.13 \text{ W/cm}\cdot\text{K}$  (Ref. 2), but comparable cooling should be achievable by using NPP laser rods with smaller

transverse dimensions. Such smaller size is also desirable in NPP laser fabrication to take advantage of the much larger pump absorption in this high-Nd-concentration material.

S. R. Chinn  
W. K. Zwicker†

## B. TRANSITION-METAL DOPED LASERS

The Ni:MgF<sub>2</sub> laser reported in the last Solid State Research Report<sup>3</sup> was operated CW in a liquid nitrogen Dewar, and the output lineshape was observed using a high-resolution grating spectrometer. The Nd:YAG pump laser was operated in the TEM<sub>00</sub> mode. At approximately 1.5 × threshold a total of 4 transverse and longitudinal modes was observed over a span of approximately 3/4 cm<sup>-1</sup>. The narrow linewidth indicates that Ni:MgF<sub>2</sub> fluorescence was primarily homogeneously broadened in the laser crystal used. The existence of several oscillating modes is most likely accounted for by spatial hole-burning.

The <sup>3</sup>T<sub>2</sub> → <sup>3</sup>A<sub>2</sub> fluorescence lineshape and lifetime as a function of temperature, polarization, and Ni concentration have been measured in Ni:MgF<sub>2</sub>. In addition, fluorescence lineshape and lifetime as a function of temperature have been measured in Co:MgF<sub>2</sub> (<sup>4</sup>T<sub>2</sub> → <sup>4</sup>T<sub>1</sub> transition) and Ni:MgO (<sup>3</sup>T<sub>2</sub> → <sup>3</sup>A<sub>2</sub> transition). The latter two crystals have previously been used as laser media.<sup>4</sup> Figure II-2 shows the 1/e decay time for three crystals; 3.3 wt% Ni in MgF<sub>2</sub>,

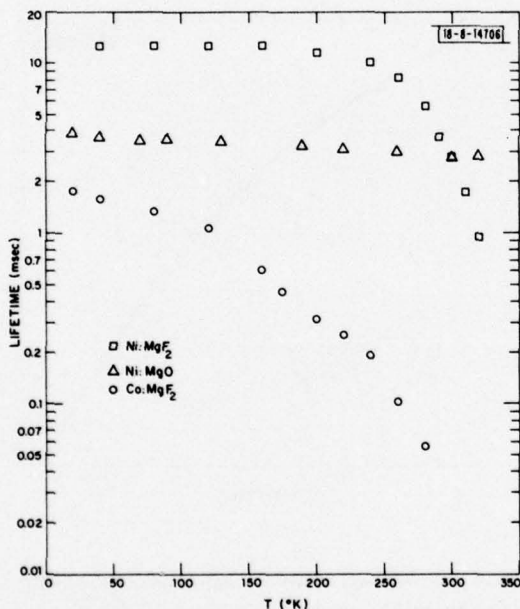


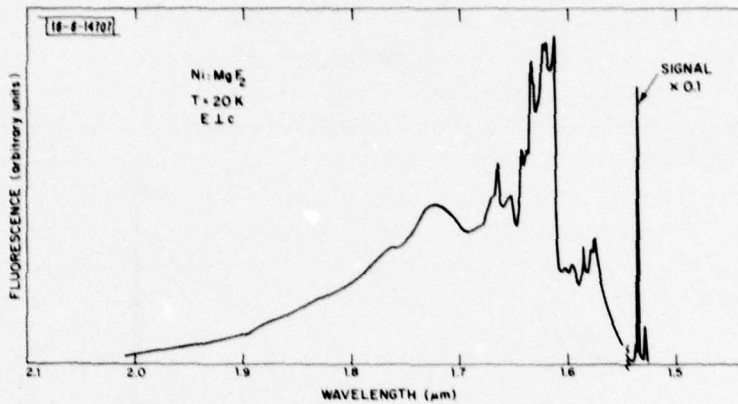
Fig. II-2. Lifetime vs crystal temperature for Ni:MgF<sub>2</sub>, Co:MgF<sub>2</sub>, and Ni:MgO.

1.3 wt% Co in MgF<sub>2</sub>, and 0.3 wt% Ni in MgO. The lifetimes observed in the Ni:MgF<sub>2</sub> sample are the same as those observed in crystals with smaller Ni concentrations. The decay time for a crystal with 6.5 wt% Ni in MgF<sub>2</sub> was observed and was about 10 percent shorter than that of the crystal with 3.3% Ni; the lifetime variation with temperature was similar. Lifetime measurements will be made on Ni:MgF<sub>2</sub> with larger amounts of Ni to determine at what doping

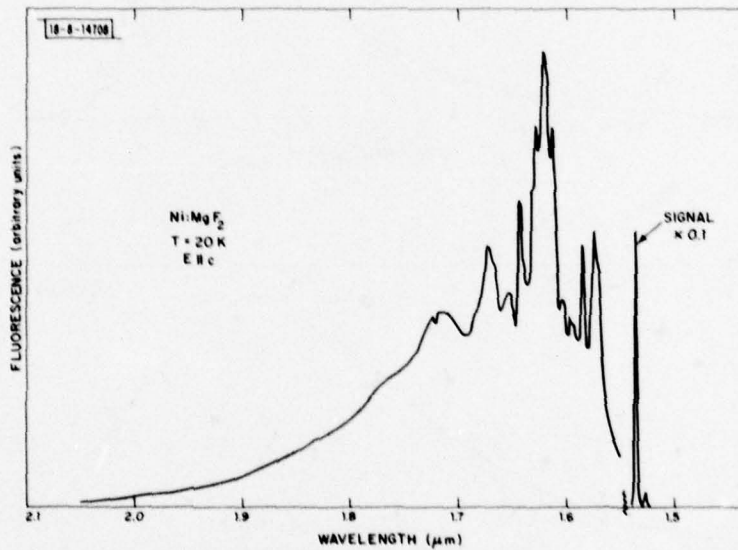
† Philips Laboratories, Briarcliff Manor, New York.

level concentration quenching becomes significant. The reduction in lifetime at high temperatures for Ni:MgF<sub>2</sub> appears to be exponential in nature. The behavior can be modeled by postulating a nonradiative decay path with an activation energy of 0.36 eV. The physical explanation for such a path is unclear, however. The shortening of decay time in Co:MgF<sub>2</sub> does not follow such a simple model. The relatively small reduction of Ni:MgO lifetime at 300 K compared to low temperatures may allow room temperature operation of a Ni:MgO laser.

In Figs. II-3(a-e) the fluorescence lineshape for Ni:MgF<sub>2</sub> is shown for crystal temperatures of 20, 80, and 200 K, observed in a crystal with 0.4 wt% Ni doping. Fluorescence from

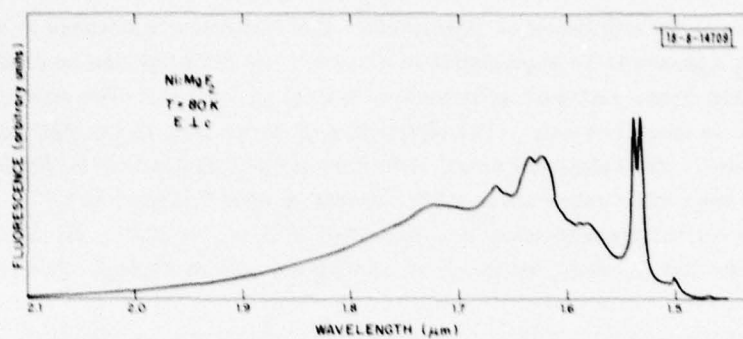


(a)

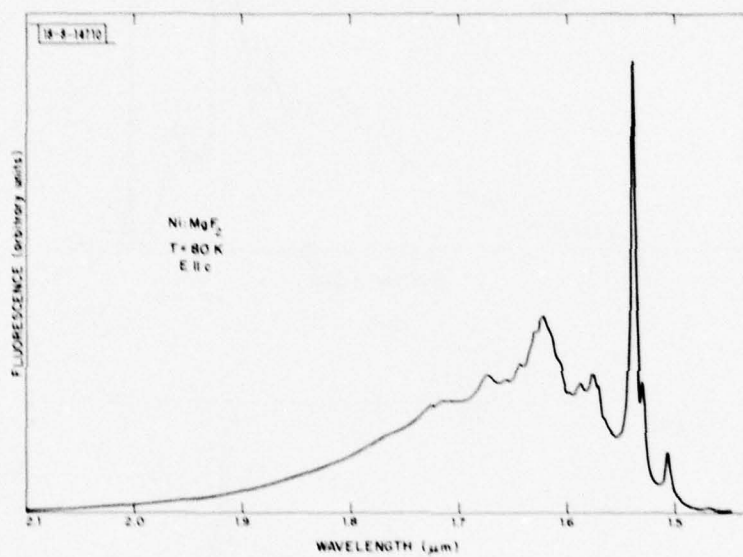


(b)

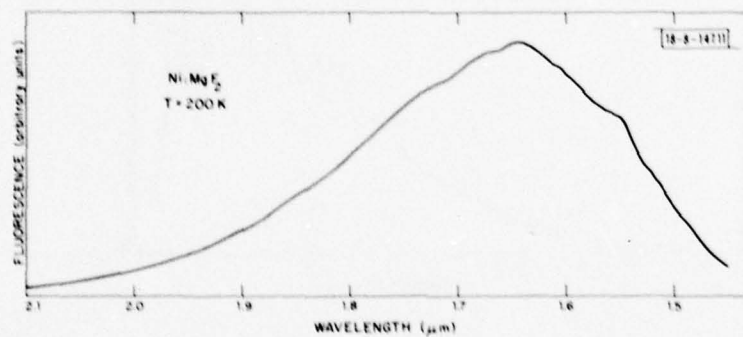
Fig. II-3(a-e). Fluorescence from Ni:MgF<sub>2</sub> at 20, 80, and 200 K. Both polarizations are shown for 20- and 80-K crystal temperatures.



(c)



(d)



(e)

Fig. II-3(a-e). Continued.

two different polarizations is indicated for 20 and 80 K. Such data can be used to predict gain lineshapes following the theoretical work of McCumber.<sup>5</sup> Of interest are the relative intensities of the two polarizations, which are indicated in Figs. II-3. The ratio of 3:1 in fluorescence intensity between  $E \parallel c$  and  $E \perp c$  previously reported<sup>4</sup> was not observed. Instead, almost similar intensities were found, indicating that the gain is not as anisotropic as had been assumed.

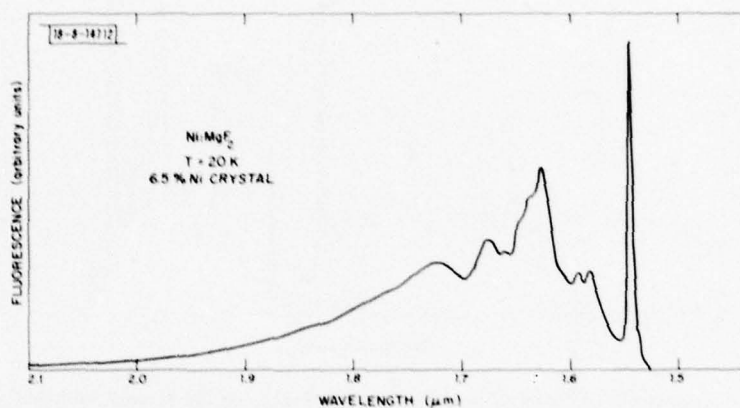


Fig. II-4. Unpolarized fluorescence from a 6.5% Ni-doped  $\text{MgF}_2$  crystal at 20 K.

While no significant concentration quenching was observed in  $\text{Ni:MgF}_2$  crystals up to at least 6.5 wt% Ni, at high Ni concentrations there was a definite increase in the linewidth of the sharp spectral components apparent in the low-temperature fluorescence. Figure II-4 shows the emission lineshape from the 6.5 wt% Ni crystal at 20 K, which can be compared with the lineshapes of Figs. II-3. Presumably, the difference is due to the increasingly random site environments in the more heavily doped crystals, which leads to inhomogeneous line broadening. The effect of such broadening, given the large overall homogeneous linewidth, should be negligible on the laser threshold of the more heavily doped crystals, however.

The unpolarized fluorescence spectra from  $\text{Co:MgF}_2$  and  $\text{Ni:MgO}$  are shown in Fig. II-5 for crystal temperatures of 20 and 80 K, respectively. The line marked in the  $\text{Co:MgF}_2$  spectrum was observed in previous measurements<sup>6</sup> and was claimed to be fluorescence from a small amount of Ni in the crystal. The time decay of emission from this line was observed in our sample, which had about 0.01% Ni, to check this hypothesis. The decay proved to be non-exponential, as shown in Fig. II-6, in which the decay of this line and that at a wavelength of 1.8  $\mu\text{m}$  are compared. The intensity of the Ni line, given the small amount of Ni in the sample, and the nonexponential decay indicate that the Ni atoms are not excited directly by the pump radiation but instead receive excitation by nonradiative transfer from Co atoms. The use of this transfer mechanism to increase pumping efficiency under broadband pump excitation should be considered.

P. F. Moulton  
A. Mooradian

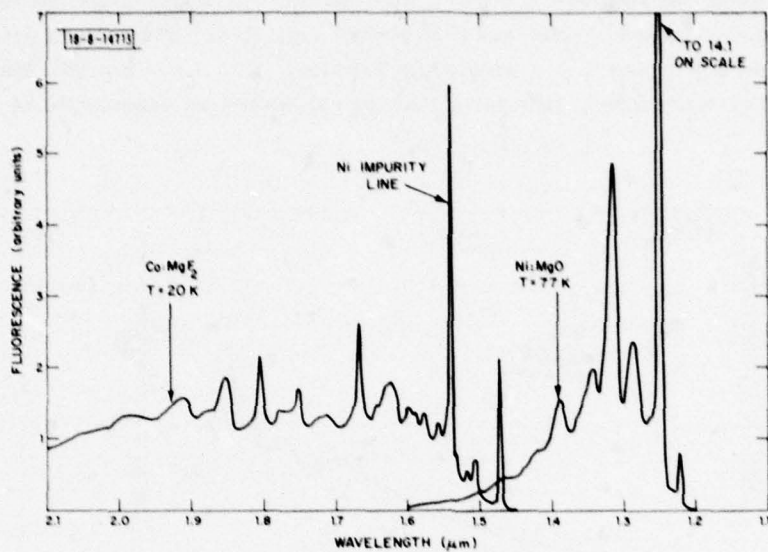


Fig. II-5. Unpolarized fluorescence from Co:MgF<sub>2</sub> at 20 K and Ni:MgO at 80 K. Ni impurity line is indicated.

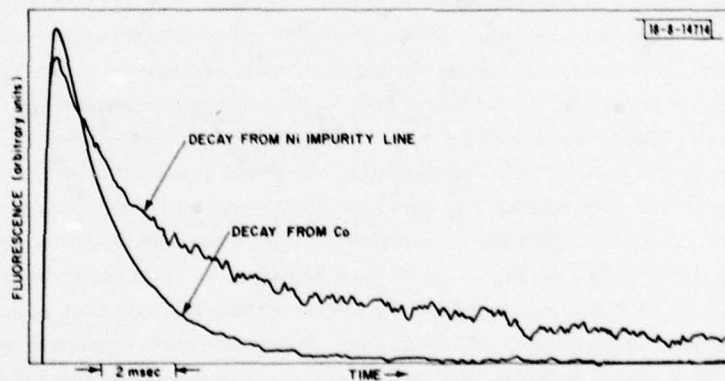


Fig. II-6. Comparison of fluorescence decay from Ni impurity line with normal decay in Co:MgF<sub>2</sub>.

### C. LASER-INDUCED BREAKDOWN OF CRYOGENIC LIQUIDS

In previous reports<sup>7-9</sup> we have discussed efficient nonlinear frequency conversion processes in liquid CO-O<sub>2</sub> mixtures. The present limiting mechanism in these processes is laser-induced breakdown (LIB) of the liquid. We have therefore undertaken a study of the LIB process in cryogenic liquids. The purpose of this study has been both to provide the necessary parameters for scaling the nonlinear processes to higher conversion efficiencies and also to gain more insight into the breakdown process itself, which will be of help in developing techniques for raising the breakdown threshold.

In contrast to the extensive investigations of the LIB process in gaseous and solid media, relatively few studies have been reported in liquid media. In particular, we are not aware of any LIB measurements in cryogenic liquids other than He. For the gas phase, there is general agreement on the mechanisms that lead to LIB. It is interesting to note that our preliminary LIB threshold measurements are at least an order of magnitude smaller than the thresholds extrapolated from dust-free gas phase data, suggesting that dust or another mechanism specific to liquids such as bubble formation may be important.

The LIB process has been investigated by both measurements of the scaling laws for LIB and temporal studies of the accompanying visible and infrared emission, liquid photoconductivity, and transmitted CO<sub>2</sub> laser pulse shapes. The effects of purifying and pressurizing the liquids as well as applying DC electric fields have also been examined. Table II-1 lists preliminary LIB energy density thresholds for four liquids. We believe that the LIB threshold variations are due to spot size and pulse duration dependences and not to a wavelength dependence. The breakdown process is statistical and the thresholds are defined as the energy densities where the LIB probability is 50 percent. All LIB thresholds were measured using liquids which had not previously been broken down. This was necessary because the LIB thresholds decrease

TABLE II-1 LASER-INDUCED BREAKDOWN THRESHOLD IN CRYOGENIC LIQUIDS IN J/cm <sup>2</sup>					
CO <sub>2</sub> laser line	R(24)		R(6)		P(12)
Wavelength (μm)	9.25		9.35		9.49
Pulse length (nsec)	55		110		80
Spot size (μm)	76	216	65	186	209
Cryogenic liquid:					
CO	314	114	436	190	164
O <sub>2</sub>	464	93	570		
N <sub>2</sub>	365	163			134
Ar	129				104

after several breakdowns. After more than 100 breakdowns the LIB threshold reaches a constant value which is a factor of 2 to 3 smaller than the original value. If the liquid is then left undisturbed the LIB threshold recovers, at least partially, over a timescale of several hours.

The three diatomic liquids, CO, O<sub>2</sub>, and N<sub>2</sub>, have comparable LIB thresholds, somewhat higher than that of Ar. The breakdown threshold decreases with increasing spot size and for the range of spot sizes we have used, with the exception of Ar, the dependence appears to be inversely proportional to the spot diameter.

Measurements of the transmitted CO<sub>2</sub> laser pulses in fresh liquid O<sub>2</sub> show that the peak transmitted power continues to increase approximately as the input energy for input energies up to at least a factor of 2 above the LIB threshold. In contrast, after the liquid has been broken down a number of times (~100) the LIB threshold becomes dependent on intensity rather than energy density. Thus, different mechanisms are responsible for the LIB in the two cases. Measurements with shorter duration (~10 nsec) CO<sub>2</sub> pulses are currently under way.

We have not observed any evidence of prebreakdown phenomena in the liquid. The ultra-violet and visible emission which consists of a line spectrum on top of a broad continuum are seen only when a spark develops in the liquid. Similar results are found for the CO vibrational fluorescence from a CO-N<sub>2</sub> solution (0.003% CO). Also, there is no measurable laser-induced photoconductivity preceding the visible emission.

A DC field across the liquids should sweep out any charges. Fields of 500 V/cm have been applied for several hours. However, no effect on the breakdown threshold has been found either in fresh liquids or in liquids that have been broken down a number of times.

We have also investigated the effect on the breakdown threshold of changing the pressure above the cryogenic liquids. The O<sub>2</sub> liquid is regularly kept at liquid N<sub>2</sub> temperature (77 K) where the vapor pressure is approximately 160 Torr. Pressurizing the liquid to 590 Torr with He or N<sub>2</sub> gas did not increase the breakdown threshold. For He there was actually a slight reduction. We have also increased the pressure above the O<sub>2</sub> liquid by increasing the bath temperature to 87.3 K (liquid Ar bath) which corresponds to an O<sub>2</sub> vapor pressure of approximately 565 Torr. In this case the breakdown threshold increased slightly from 93 to 147 J/cm<sup>2</sup> for a 216- $\mu$ m spot size [R(24) line]. For smaller spot sizes (~70  $\mu$ m) there was no change.

In contrast to the lack of LIB studies, there have been numerous investigations of the DC dielectric breakdown properties of cryogenic liquids.<sup>10</sup> Typical DC thresholds are 1 to 2 MV/cm which correspond to energy densities of 300 to 1200 J/cm<sup>2</sup> (100-nsec pulse durations), in reasonable agreement with our LIB threshold results. The interpretation of the DC measurements, however, is always complicated by electrode effects. Laser measurements avoid this ambiguity and complement the DC results.

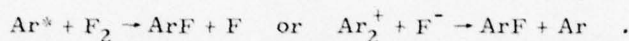
It is too early to draw any final conclusions about the LIB mechanism in these cryogenic liquids. If cascade ionization is important, it is necessary to have an initial electron within the focal volume to trigger the process. It is worth noting that the background charge density in cryogenic liquids can be very low. For example, in O<sub>2</sub> liquid, conductivities as low as 10<sup>-20</sup>  $\Omega^{-1}$  cm<sup>-1</sup> have been reported. This corresponds to a carrier concentration of only 50 cm<sup>-3</sup> which raises some questions concerning the source of the initial electron. It might be supplied by a low ionization potential impurity or a micron-sized dust particle. The spot size dependence of the breakdown threshold may be consistent with the latter possibility. However, the effects of micron-sized gas bubbles which are potentially present must also be considered. The gas inside a bubble may have a lower breakdown threshold than the liquid.

In conclusion, we do not believe that we have yet reached the intrinsic breakdown thresholds of the cryogenic liquids. We feel that a special effort is warranted in order to minimize the probability of dust particles or bubbles in the liquids.

S. R. J. Brueck  
H. Kildal

#### D. LASER ASSOCIATION OF DIATOMIC MOLECULES

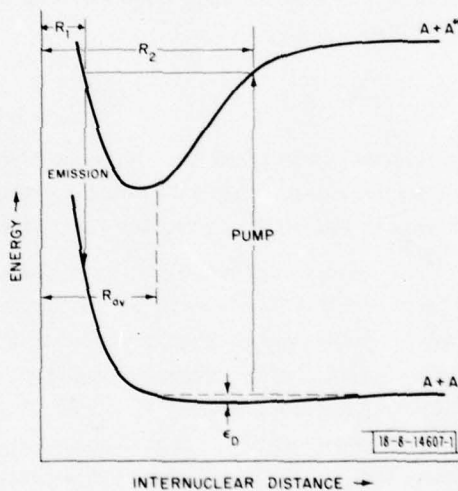
Conventionally, excimers and exciplexes have been formed as a result of collisional processes in electron beam or discharge excited gas mixes in which the dominant channels for formation are either metastable molecule reactions or ion recombination reactions; for example,



These approaches to excitation have been the basis for recent progress of UV excimer laser technology as well as for studying the structure of the excimers themselves.

Now that intense efficient sources of monochromatic UV light are readily available in the form of excimer lasers, an alternate approach to the production of excimers can be envisaged. The technique is to use the UV light to associate directly the unbound atomic constituents of the excimer, a process illustrated schematically in Fig. II-7. This formation method has a number

Fig. II-7. Potential energy curves for a normally unbound molecule which is associated with UV light. In general,  $R$  is a molecular internuclear distance.  $R_{av}$  is the average of the right ( $R_2$ ) and left ( $R_1$ ) turning points.



of unique practical and scientific ramifications. First, as can be seen from Fig. II-7, an optically associated excimer forms an interesting candidate for a two-level laser system. If the reradiated light terminates high on the repulsive wall of the dissociative ground state, the lower level of the laser would be essentially unoccupied. In addition, the bandwidth of a transition which begins in an excited vibronic state with high vibrational quantum number can be of the order of one electron volt; thus, the system would be useful as a broadly tunable UV laser. Secondly, since the laser associative process is specific in the final state, as compared to collisional production channels, new structural details about the resulting molecule may be learned. As will be discussed for  $\text{Hg}_2$  below, excitation to high-lying vibrational levels in the

excited electronic state gives information on the steeply repulsive part of the ground state potential curve.

### 1. General Considerations

Absorption at frequency  $\nu$  of unbound atoms into a bound excited state will occur if the separation between atoms is between  $R_1$  and  $R_2$  (Fig. II-7). If  $R_{av}$  is sufficiently far from the point at which the repulsive curve reaches  $kT$  above the asymptotic ground-state level, we may approximate the volumetric average of the hard-core correlation function by unity. Under these conditions the probability,  $P$ , for finding another atom within  $\Delta R$  of any given atom is

$$P = 4\pi n \Delta R (R_{av})^2 \quad (\text{II-1})$$

where  $n$  is the number density of atoms. Notice that this probability, which is also the fractional number of unbound quasi-molecular absorbers, is independent of temperature. The absorption coefficient,  $\alpha$ , for the free-bound process is then given by

$$\alpha = P n \sigma = 4\pi \Delta R (R_{av})^2 \sigma_\lambda n^2 f \quad (\text{II-2})$$

where  $\sigma_\lambda$  is the wavelength-dependent optical cross section.

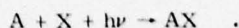
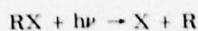
There will also be a contribution to the production of excited-state molecules from ground-state molecules which are weakly bound by Van der Waals forces. The expression for the fraction,  $A_2/A$ , of such molecules is

$$\frac{A_2}{A} = KA \quad (\text{II-3})$$

where  $A$  is expressed in pressure,  $K$  is the equilibrium constant, and where we have assumed a homonuclear molecule. For a diatomic molecule, this equilibrium constant can be shown to be proportional to the ratio of partition functions of the molecular to atomic species times the factor  $e^{-\epsilon_D/kT}$ , where  $\epsilon_D$  is the energy of dissociation of the ground-state molecule. For molecules with  $h\nu_0 \ll kT$ , where  $\nu_0$  is the fundamental vibrational frequency, the Boltzmann factor determines the temperature dependence of  $A_2/A$ . Since the number of free absorbers does not have a strong temperature dependence, the relative importance of bound-bound excitation will clearly diminish when  $T \gg \epsilon_D/k$ . In the case of mercury, which has  $\epsilon_D \sim 480 \text{ cm}^{-1}$ , the bound-bound and free-bound contributions are equal at  $T \sim 300^\circ\text{C}$ .

An interesting aspect of the associative absorption is that because of the rapid spatial relaxation times of the atoms, a large number of molecules may be created with short intense pulses. Neglecting coherence effects which are unimportant for free-bound transitions, the maximum excitation rate for a two-level absorber interacting with an intense field is the rate of production of the absorbing species. In the case of unbound quasi-molecules, this production rate is the inverse of the time for collision between two atoms with an impact parameter less than  $R_{av}$ ; in other words,  $n\hat{v}\pi R_{av}^2$ , where  $\hat{v}$  is the average relative molecular velocity. For  $R_{av} \sim 4 \text{ \AA}$ , a typical value, the collision time is 5 nsec at  $3 \times 10^{18} \text{ mol/cc}$  (100 Torr). In contrast, the dimer formation rate is 600 nsec at the same number density. Thus, with intense pulses of  $\leq 100$ -nsec duration, associative absorption will dominate the excitation channel since quasi-molecular absorbers can be produced during the pulse duration.

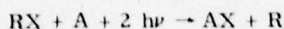
So far our discussion has considered only the situation in which the molecule is formed from free atom constituents. In fact, many interesting exciplex molecules, such as the rare gas monohalides, have one atom which is too reactive to remain in its unreacted state for a significant period of time. In such circumstances, optical pumping of the desired exciplex, AX, can be accomplished by the following two-step process:



Assuming no recombination of RX during the pulse, the cross section,  $\sigma_2$ , for this process can be shown to be approximately

$$\sigma_2 \approx \frac{4\sigma_A \sigma_D E n \Delta R (R_{av})^2}{h\nu} \quad (\text{II-4})$$

where  $\sigma_A, \sigma_D$  are the cross sections for the dissociative and associative steps, E is pulse energy, and n is the number density of the high-pressure gas. If realistic values are assumed for the various quantities in Eq. (II-4), a cross section of  $10^{-22} \text{ cm}^2$  is calculated. As a point of reference, for the same intensities typical near-resonance two-photon cross sections for rare gases are  $10^{-24} \text{ cm}^2$ . Note that the above mentioned two-step process would have many functional similarities to the following nonlinear free-free absorption process



which has been discussed by Dubov *et al.*<sup>11</sup> and Harris.<sup>12</sup>

## 2. Specific Examples

### a. Hg<sub>2</sub>

Figure II-8 shows the relevant molecular energy levels for Hg<sub>2</sub>. The designation of the molecular energy levels is that appropriate for heavy molecules which are examples of Hund's case "a" and "c" coupling; that is,  $\Omega$  is the appropriate quantum number. In the mercury system, Hg<sub>2</sub> excimers in the O<sub>u</sub><sup>+</sup> state may be formed by excitation with an ArF laser at 193 nm. The O<sub>u</sub><sup>+</sup> level correlates with two Hg atoms in the <sup>1</sup>S<sub>0</sub> and <sup>1</sup>P<sub>1</sub> states, respectively. The long-range characteristic of the O<sub>u</sub><sup>+</sup> potential well arises from the dipole-dipole coupling of the atoms in these two constituent states. The dipole moment connecting the O<sub>u</sub><sup>+</sup> and O<sub>g</sub><sup>+</sup> states is 4 Debye,<sup>13</sup> and the corresponding radiative lifetime is ~0.5 nsec.

In Fig. II-9, we show the bound-free emission from the Hg<sub>2</sub> after excitation of the molecule with an ArF laser. The undulating character of the re-emission is quite striking and remains unaltered up to the low-pressure limit of our detection system ~3 Torr. This and similar bands in Zn<sub>2</sub> and Cd<sub>2</sub> were investigated by Mrozowski<sup>14</sup> in the early 1930's, using spark source excitation and were called "die Fluktuationen-Banden." The fact that we observe the undulations at such low pressures, which is collision free for the lifetime of the molecule, indicates that the "Fluktuationen" are Condon diffraction bands; that is, they arise from the oscillations of the excited state wave function as "reflected" on the ground-state repulsive curve. If the Hg<sub>2</sub> pressure is raised to the point that the collisional rate exceeds the radiative rate, the emission band envelope changes shape and begins to exhibit the morphology of a vibrationally relaxed band.

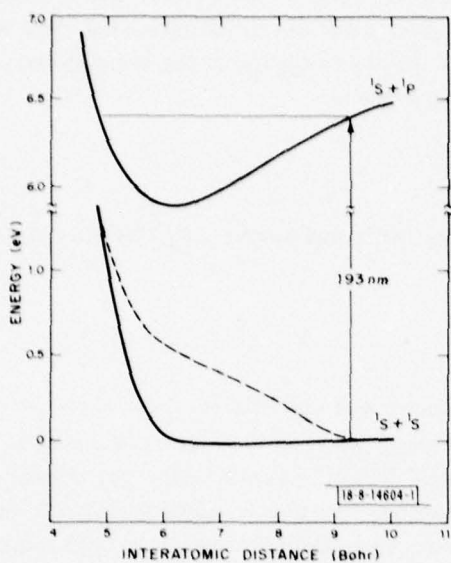


Fig. II-8. Molecular energy levels of  $\text{Hg}_2$ , which are relevant to excitation of  $\text{O}_u^+$  level with an ArF laser.

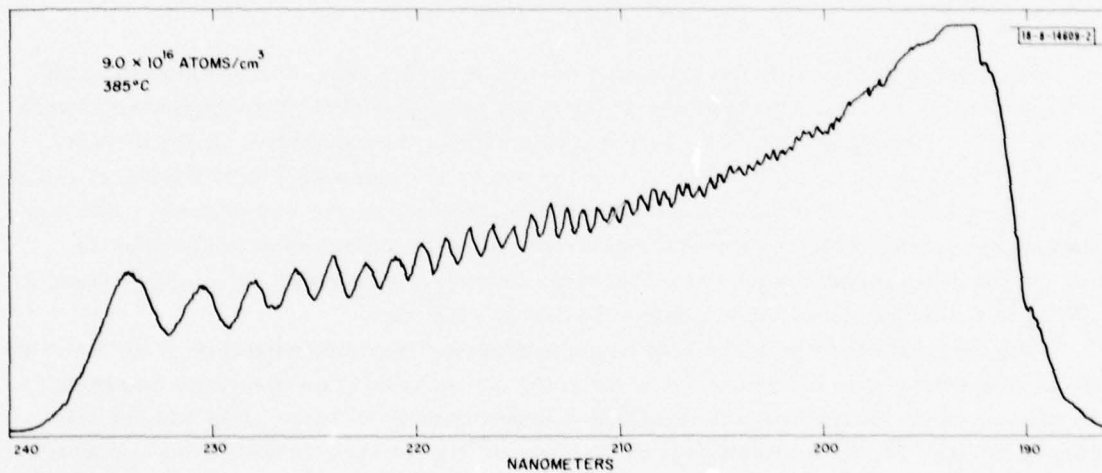


Fig. II-9. Fluorescence spectrum of the  $\text{O}_u^+ \rightarrow \text{O}_g^+$  transition in molecular  $\text{Hg}_2$ . The  $\text{Hg}_2$  density is approximately  $3 \times 10^{18}$  molecules/ $\text{cm}^3$ .

Consideration of the Franck-Condon principle indicates that the unrelaxed emission band will be composed of frequencies given by the dotted line in Fig. II-8. In addition, by using the WKB approximation to derive the wave functions in both the excited and ground states, one can derive the following approximate expression for the spacing of the maxima,  $\Delta\epsilon$ ,

$$\Delta\epsilon \approx \frac{\partial u_g}{\partial R} \frac{\pi}{K_v(R)}$$

where  $\partial u_g / \partial R$  is the slope of the ground-state curve at the particular internuclear distance,  $R$ , corresponding to the transition frequency, and  $K_v(R)$  is the local wavenumber of the vibrational wave function of the excited state. In case of the  $\text{Hg}_2$  molecule  $K_v(R)$  can be estimated from the potential curves generated by Mies *et al.*; <sup>13</sup> thus, from the measured maxima of the oscillations, we obtain  $\partial u_g / \partial R$ , a physical quantity which is both difficult to measure by conventional means, and to calculate (because of the importance of correlation among the molecular electrons). The results which we obtain are in agreement with this approximate formula. However, it will be necessary to use numerical techniques to generate the Franck-Condon overlap before a refined ground-state potential can be obtained.

The final comment with respect to the mercury  $\text{O}_u^+ \rightarrow \text{O}_g^+$  band is that its strong transition moment and broad emission band make it an excellent candidate for an optically pumped tunable laser.

#### b. Xenon Bromine

While bromine is not readily available in atomic form, it can be photolytically generated readily from a large number of molecular compounds including HBr. Thus, by irradiating a high-pressure sample of xenon which has been lightly doped with HBr, with an intense ultra-violet source, it should be possible to observe the two-step excitation process described above.

In Fig. II-10 we show the XeBr spectrum which was obtained when irradiating a 2-Torr HBr, 300-Torr Xe mixture with 4 mJ of focused 193-nm light. The intensity of this emission displays an intensity squared behavior, as would be predicted from Eq. (II-4). However, it still is not possible to rule out two-photon pumping of trace amounts of  $\text{Br}_2$  followed by subsequent reaction

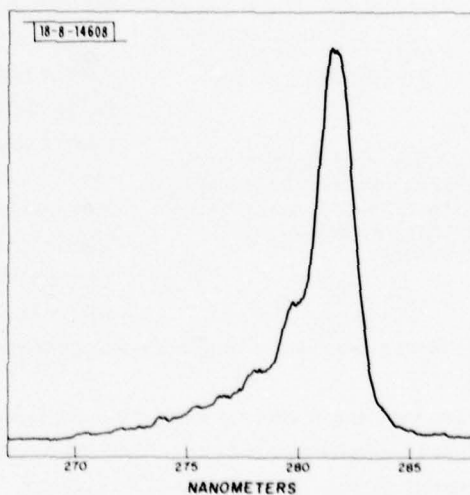


Fig. II-10. Spectrum of the XeBr  $B \rightarrow X$  fluorescence.

with Xe as the source of the excited XeBr. The cross section for reaction has not been previously measured and, thus, further experimental work must be carried out before the importance of the two-photon channel can be gauged.

D. J. Ehrlich  
R. M. Osgood, Jr.

#### E. OPTICAL ENERGY EXTRACTION FROM MOLECULAR MERCURY

Excimeric mercury has many properties which make it a desirable medium for a high-power laser. For example, compared to the gas mixtures for the rare gas-monohalide lasers, it is easily excited at high pressure in an electron beam stabilized discharge. Further, because the lowest excited  $\text{Hg}_2$  levels are both collisionally and radiatively metastable, optical energy can be stored in the  $\text{Hg}_2$  during the application of a comparatively long excitation pulse.

The work which we describe in this section is directed toward investigating methods of extracting the stored optical energy in the form of a short pulse of coherent ultraviolet light.

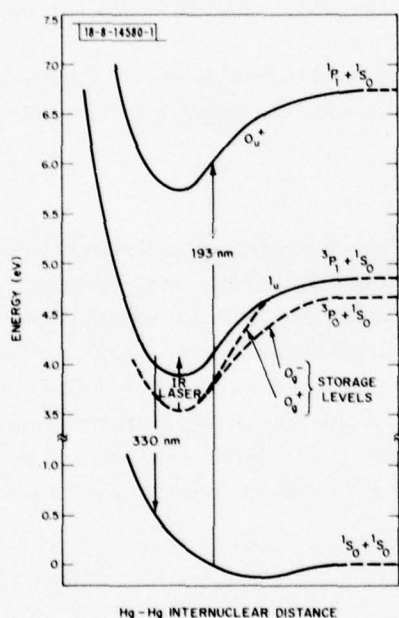


Fig. II-11. Potential energy curves of  $\text{Hg}_2$ , which show levels and transitions pertinent to infrared-induced optical energy extraction from molecular mercury.

$\text{O}_g^+$  levels, it was necessary to use a combination transient digitizer signal average to observe the signal.

Thus far we have observed a 200 percent laser-induced enhancement in the 300-nm fluorescence. This enhancement varies linearly with both HF and UV intensity and depends sensitively on the overlap of the HF and UV laser beams. These results rule out the possibility of a

Previous calculations<sup>15</sup> have shown that the most direct extraction technique for the specific case of  $\text{Hg}_2$  is via excited-state optical pumping with an infrared laser. In Fig. II-11 a simplified energy level diagram for  $\text{Hg}_2$  is shown. The two storage levels with the most population are the  $\text{O}_g^+$  and  $\text{O}_g^-$  levels. The former level is connected via a 0.6 Debye transition moment with the essentially unpopulated  $1_u$  level,<sup>13</sup> which is itself radiatively connected to the  $\text{O}_g^+$  ground state. The population in the storage levels may be switched to the  $1_u$  level with the application of a 2.5- to 4- $\mu\text{m}$  infrared pulse.

The experimental apparatus which we have used to investigate the energy extraction process is shown in Fig. II-12. In essence, a steady-state population  $\text{Hg}_2$  in the  $\text{O}_g^+$ ,  $\text{O}_g^-$  levels was produced by optically pumping high-pressure Hg vapor with the output of a doubled argon ion laser. The purity of the  $\text{Hg}_2$  sample was checked by observing the  $\text{Hg}_2$  spectrum under Hg arc lamp excitation and by measuring the  $\text{Hg}_2$   $1_u$  decay time after excitation of the  $\text{Hg}_2$  with the output from an ArF laser. The mercury sample was then irradiated with a high-energy pulse ( $\sim 2.7 \mu\text{m}$ ) from a HF chemical laser. The transient population in the  $1_u$  level was monitored by observing the induced change in the  $1_u \rightarrow \text{O}_g^+$  fluorescence at 300 nm. Because of the low population in the

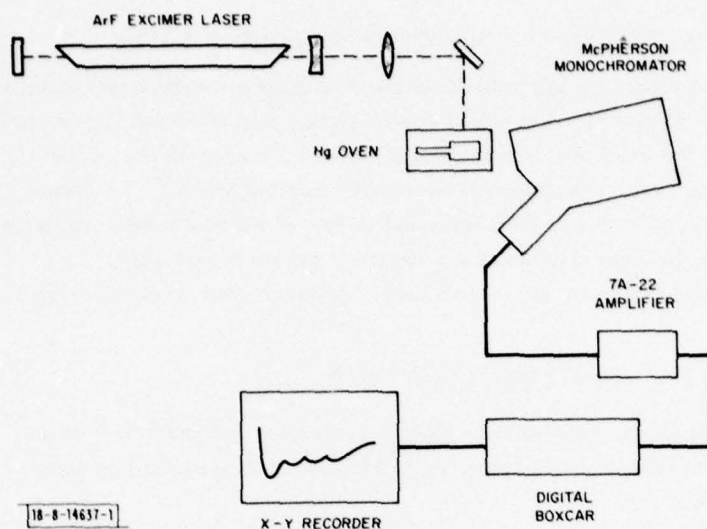


Fig. II-12 Experimental apparatus used in study of infrared-laser-induced UV emission from  $\text{Hg}_2$ .

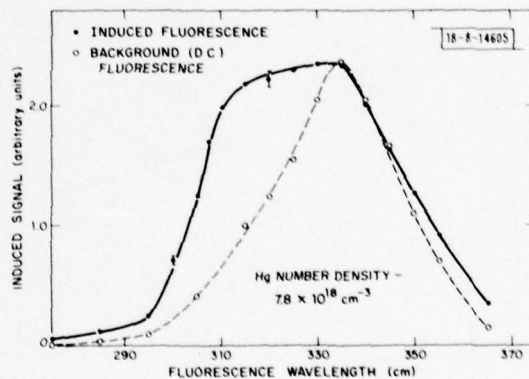


Fig. II-13. Spectrum of infrared-induced 300-nm emission (open circles) from  $\text{Hg}_2$  compared with thermal background (solid circles).

spurious signal due to laser breakdown. In addition, by changing the operating conditions of the HF laser, we have observed an intensity independent alteration in the induced signal. This may be attributable to the change in spectral output of the laser for different laser gas pressures.

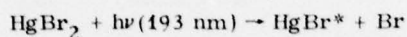
Figure II-13 shows a spectral scan of the 300-nm induced signal (circles) along with the background (solid dots) 300-nm signal which arises from the small thermal population of the  $1_u$  level. The induced spectra is considerably broader than and slightly blue shifted from the thermalized emission. Both of these changes result from the fact that the HF laser populates high (nonthermal) vibrational levels in  $1_u$  state.

D. J. Ehrlich  
R. M. Osgood, Jr.

## F. PHOTOLYTICALLY EXCITED MERCUROUS BROMIDE LASER

Ultraviolet photolysis of polyatomic molecules is an attractive technique for exciting a visible gas laser. Photolytic processes can be highly specific with regard to final fragment electronic states; for example, spectroscopic measurements of the nascent yield from photolysis of  $N_2O$  at 130 nm have shown 100-percent quantum yields.<sup>16</sup> Further, the bandwidth of molecular dissociative bands is well matched to that of many excimer radiators. As a result, driving the photolysis laser with efficient excimer lamps is possible.

In order to investigate the photolytic laser approach, we first chose to investigate the process



which produces population inversion in  $HgBr$ . Recently, Schimitschek *et al.*<sup>17</sup> have demonstrated laser action from this system; however, few details regarding laser efficiency, limitations, etc., were given.

In our experiment, we chose to pump longitudinally a 26-cm-long quartz sample cell containing the  $HgBr_2$ . Sufficient vapor pressure of  $HgBr_2$  was obtained by heating the sample cell, with a slightly cooler reservoir arm, in a brass-lined oven of low-density firebrick. The laser cavity was formed with two dielectric mirrors with 30-cm spacing and whose radii of curvature and reflectivities were  $R = \infty$ , 88 percent; and  $R = 60$  cm, 98 percent. The ArF laser pump beam was weakly focused (through the flat mirror) to a spot size of a few millimeters.

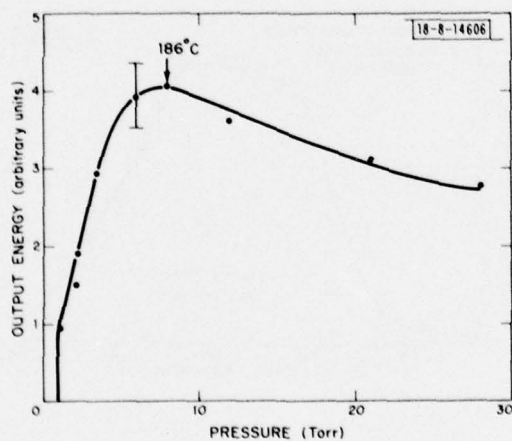


Fig. II-14. Dependence of output of  $HgBr$  photolysis laser of  $HgBr_2$  vapor pressure.

The output of the laser is in the green at 502 nm. Despite rather large incidental intracavity losses, laser oscillation was readily obtained with this apparatus. Figure II-14 shows a plot of output energy vs  $HgBr_2$  pressure. The laser threshold was at a pressure of  $\sim 400$  mTorr. As the pressure was raised, a larger fraction of the pump pulse was absorbed in the  $HgBr_2$  vapor and the laser power increased proportionally. For much higher pressures, i.e.,  $>25$  Torr, energy deposition was not uniform along the optical axis, therefore, higher pressures were not studied. At present we are investigating the source of the turnover at  $186^\circ C$  shown in Fig. II-14.

D. J. Ehrlich  
R. M. Osgood, Jr.

## G. HIGH-SENSITIVITY SUBMILLIMETER HETERODYNE RECEIVER

We report the results of radiometric determinations of noise equivalent powers of a new quasi-optical receiver system in the wavelength range of 1 mm to 170  $\mu\text{m}$ . At a frequency of 670 GHz the highest sensitivity [ $4.3 \times 10^{-19}$  W/Hz double sideband (DSB)] to date has been obtained. These measurements indicate, that at least up to 1760 GHz, there are no fundamental problems impeding the development of high-sensitivity receivers.

The experimental system used in these measurements is essentially a Dicke type radiometer which mixes a laser local oscillator (LO) with a blackbody of known temperature. Illustrated in Fig. II-15, it consists primarily of the following components: (1) corner reflector

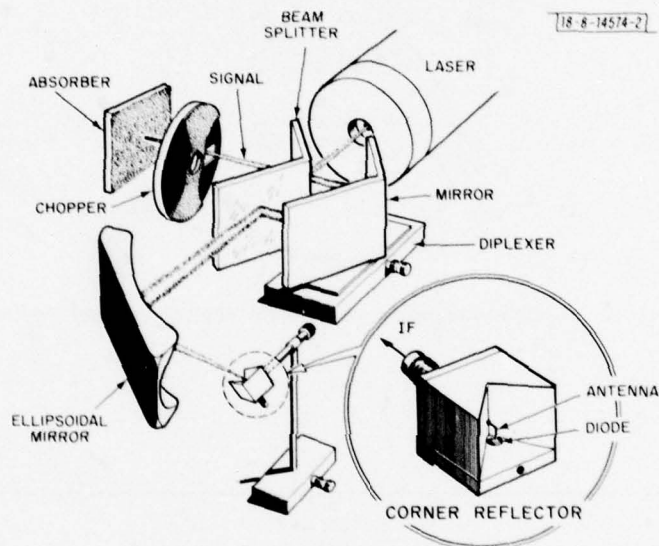


Fig. II-15. Quasi-optical submillimeter receiver using corner reflector diode mount.

diode mount, (2) ellipsoidal coupling mirror, (3) Mach-Zehnder diplexer, (4) laser LO, and (5) low-temperature absorber. The GaAs Schottky diode mounted in the corner reflector was developed especially for high-frequency applications and has been discussed elsewhere.<sup>18</sup> The diodes are typically 1  $\mu\text{m}$  in diameter, have  $1.5 \times 10^{-15}$  F capacitance and a series resistance of 45  $\Omega$ .

As shown in Fig. II-15, the detector consists of a long wire antenna mounted in a 90° corner reflector. This approach for the submillimeter region was recently proposed by Kräutle, Sauter, and Schultz.<sup>19</sup> They both theoretically and experimentally demonstrated that the addition of a corner reflector to a long wire antenna would improve the gain by about 12 dB. However, in their actual experimental setup the conversion loss was relatively high (29.5 dB).

In order to optimize a corner reflector mount we carried out 100 times scale modeling experiments at 6 to 8 GHz. One early design, which looked sufficiently promising for actual submillimeter construction, is a 90° corner cube (*i.e.*, a 90° corner reflector with a ground plane) with a  $4\lambda$ -length antenna spaced  $1.2\lambda$  from the corner. The beam pattern, obtained from

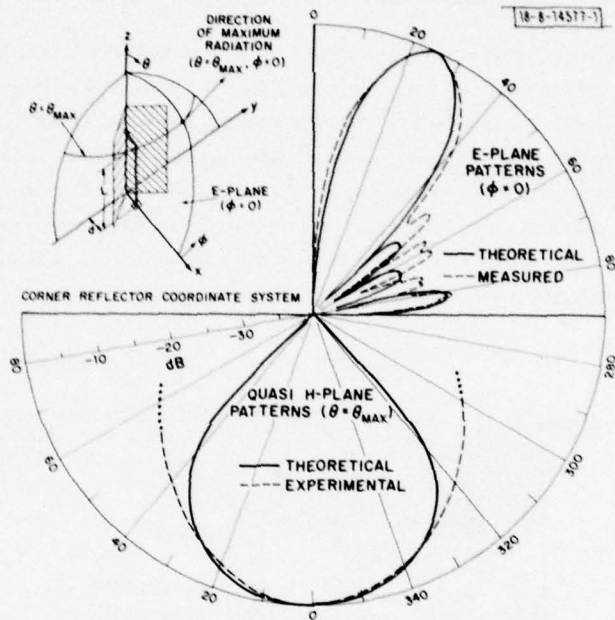


Fig. II-16. X-band modeling results for the 90° corner reflector.

TABLE II-2				
$\lambda$ ( $\mu\text{m}$ )	Frequency (GHz)	Total Systems Noise Temperature (K) (DSB)	Mixer Temperature (K)	Conversion Loss (dB)
946.	316.9	13,000	7,800	12.8
447.1	670.5	9,700	5,900	11.6
432.6	692.9	13,100	6,900	11.9
419.6	716.2	13,000	6,800	11.9
393.6	761.6	14,500	7,600	12.3
170.6	1,757.5	370,000 <sup>†</sup>		
† Diplexer not working at this wavelength.				

the modeling, is shown in Fig. II-16. The principal lobe is seen to be at an angle of  $25^\circ$  to the antenna, and has a roughly elliptical cross section of beam width of  $14^\circ \times 38^\circ$  (full width at 3 dB points).

The local oscillator and a corresponding mode from the blackbody (Eccosorb AN-72) at liquid nitrogen temperature were coupled to the mixer utilizing a diplexer. This diplexer was essentially a Mach-Zehnder type interferometer, similar in principle to that used by the National Radio Astronomy Observatory<sup>20</sup> and Erickson,<sup>21</sup> but made specifically for the 0.4-mm-wavelength region. The beam splitters are 3-mil mylar stretched over machined reflector mounts and gave roughly 50-percent transmission. An extremely short focal length, right angle, ellipsoidal mirror was used to couple in the transmitted signal and LO into the antenna pattern of the diode. With this system virtually all of the signal and better than 90 percent of the LO were transmitted.

A carcinotron was used for the measurements at 1 mm. The laser LOs used at the other wavelengths were far infrared lasers of standard waveguide design<sup>22</sup> and had an output power of about 30 mW when pumped by a free-running stable  $\text{CO}_2$  laser of about 50 W. These sources were found to be sufficient to saturate the mixer diode at all but the 170- $\mu\text{m}$  line. The wavelength of each LO line was unambiguously determined by using the diplexer as an interferometer; tuning through approximately 10 interference maxima allowed a wavelength measurement of 0.5 percent accuracy.

The results of our first measurements are summarized in Table II-2. The rectified IF signal was read on a DVM, and the difference in voltages between the hot (room temperature absorber on chopper) and cold absorber synchronously detected. The amplifier had a measured noise temperature of 245 K (2.6 dB). A standard Y-method interpretation of the data then yielded the results shown in the table.

These measurements demonstrate that it is possible to make sensitive heterodyne detectors at submillimeter frequencies. Second-generation devices of this basic design are now being fabricated and should have wide application.

H. R. Fetterman  
P. E. Tannenwald  
B. J. Clifton

C. D. Parker  
W. D. Fitzgerald†  
N. R. Erickson‡

---

† Group 33.

‡ University of California, Berkeley, California.

## REFERENCES

1. R. H. Bruce and D. S. Cannell, *Rev. Sci. Instrum.* **47**, 1323 (1976).
2. P. H. Klein and W. J. Croft, *J. Appl. Phys.* **38**, 1603 (1967).
3. Solid State Research Report, Lincoln Laboratory, M.I.T. (1977:4), p. 15.
4. L. F. Johnson, H. J. Guggenheim, and R. A. Thomas, *Phys. Rev.* **149**, 179 (1966).
5. D. E. McCumber, *Phys. Rev.* **134**, A299 (1964).
6. L. F. Johnson, R. E. Dietz, and H. J. Guggenheim, *Appl. Phys. Lett.* **5**, 21 (1964).
7. Solid State Research Report, Lincoln Laboratory, M.I.T. (1976:4), p. 23, DDC AD-A039175.
8. Solid State Research Report, Lincoln Laboratory, M.I.T. (1977:3), p. 17, DDC AD-A050551.
9. Solid State Research Report, Lincoln Laboratory, M.I.T. (1977:4), p. 19.
10. T. J. Gallagher, Simple Dielectric Liquids: Mobility, Conduction and Breakdown (Clarendon, Oxford, 1975).
11. V. S. Dubov, L. Gudzenko, L. Gurvich, and S. Iakovlenko, *Chem. Phys. Lett.* **45**, 330 (1970).
12. S. Harris, private communication.
13. F. Mies, W. Stephens, and M. Krauss (to be published).
14. S. Mrozowski, *Z. f. Phys.* **87**, 340 (1934); *Z. f. Phys.* **62**, 314 (1930).
15. P. L. Kelley, private communication.
16. G. Black, R. Sharpless, T. S. Langer, and D. Lorents, *J. Chem. Phys.* **62**, 4266 (1975).
17. E. Schimitschek, J. Celto, and J. Trias, *Appl. Phys. Lett.* **31**, 608 (1977).
18. B. J. Clifton, *IEEE Trans. Microwave Theory Tech.* **25**, 457 (1977).
19. H. Kräutle, E. Sauter, and G. V. Schultz, *Infrared Phys.* **17**, 477 (1977).
20. P. Goldsmith, private communication.
21. N. R. Erickson, *IEEE Trans. Microwave Theory Tech.* **25**, 865 (1977).
22. D. T. Hodges and F. B. Foote, *IEEE J. Quantum Electron.* **13**, 491 (1977).

### III. MATERIALS RESEARCH

#### A. BIAS-ASSISTED CdTe PHOTOEMITTER DEVELOPMENT

For the successful operation of infrared photocathodes utilizing graded-gap  $\text{Hg}_x\text{Cd}_{1-x}\text{Te}$  structures, as previously proposed,<sup>1</sup> photogenerated electrons must be able to escape from the surface of the CdTe emitter. In earlier experiments<sup>2</sup> we found that direct cesiation of CdTe (i.e., with no metal overlayer) lowered the work function,  $\Phi$ , to 2.3 eV. This value is not low enough to achieve negative electron affinity (NEA) with respect to the lowest,  $\Gamma_6$ , conduction band minimum. However, it is close to that necessary to achieve NEA relative to the  $L_6$  conduction band minimum (depending on the magnitude of the band bending induced by the Cs/O cesiating layer), which would make it feasible to operate a CdTe photocathode in a bias-assisted, transferred-electron mode,<sup>1</sup> as has been demonstrated for InP (Ref. 3).

In an attempt to obtain bias-assisted photoemission from CdTe, we evaporated an In grid of 6- $\mu\text{m}$  stripes with 60- $\mu\text{m}$  openings onto p-CdTe substrates. (The In film was thick enough to be opaque to both light and photoelectrons.) The entire surface was then cesiated. Since In produces a good Schottky barrier on p-CdTe, the grid could be used to bias the surface of the emitter. With voltage applied to the grid, it was anticipated that photoelectrons would be emitted from the cesiated CdTe openings, provided that the Cs/O layer had sufficient conductivity to maintain a uniform surface potential across the openings. Weak bias-assisted photoemission was obtained when such devices were exposed to white light from a tungsten filament, but the emission decayed markedly within a few hours after cesiation.

We have now established that the decay of the photoemission results from diffusion of Cs into CdTe. Although even a thin metal overlayer has the disadvantage of attenuating the photoelectron flux, we have concluded that it will be necessary, because of the diffusion problem, to cover the entire CdTe surface with such an overlayer and then cesiate the metal to lower its work function. We have therefore studied Cs diffusion into a number of potentially useful metals. For Al, Ti, and Cr, which were found to have low Cs diffusion rates, we have measured the work functions of cesiated surfaces and have obtained preliminary results on the properties of Schottky barriers formed by these metals on p-CdTe.

Diffusion of Cs into CdTe:— The possibility that diffusion of Cs is responsible for the temporal decay of photoemission from cesiated CdTe was suggested by the affinity of bulk Te for Cs (Ref. 4). We have confirmed this mechanism by comparing Auger sputter profiles for CdTe samples after various exposures to atomic Cs vapor with such profiles for GaAs samples, where Cs is known to reside only on the surface.

With the thermal Cs source used in our experiments, it is not possible to measure the Cs atom flux striking the sample. To determine relative Cs exposures of CdTe samples from run to run, we have monitored the white-light photoemission of Ar-ion-bombarded single-crystal GaAs during exposure to Cs. After adsorption of a critical amount of Cs (less than one monolayer<sup>5</sup>), the photoemission rises rapidly from zero to a maximum and then falls to zero again as more Cs is deposited. As soon as Cs exposure is stopped, the photoemission begins to rise due to desorption of excess Cs, reaching a stable level in about 30 min. The Auger sputter profile obtained after reaching equilibrium is shown as curve (a) of Fig. III-1, where the ratio of Cs to Ga Auger peak heights is plotted vs the time of sputtering with 500-eV Ar ions incident

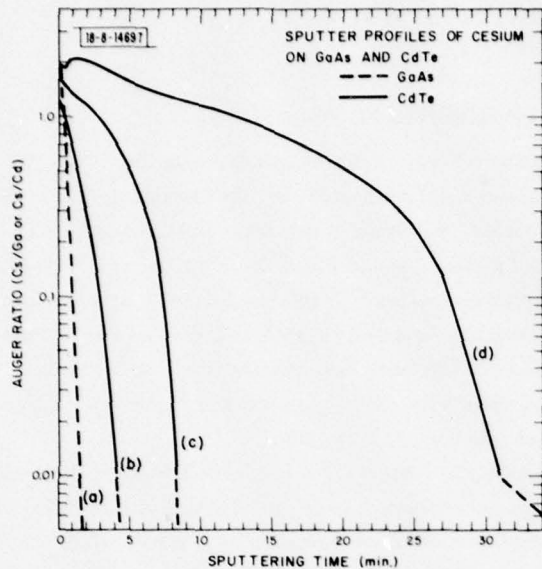


Fig. III-1. Ratios of Auger peak height [in  $dn(E)/dE$ ] for Cs/Ga and Cs/Cd vs Ar-ion sputtering time for GaAs (dashed curve) and CdTe (solid curves) after exposure to atomic Cs vapor. The relative Cs exposures for curves (b), (c), and (d) are 1.5/2.5/8.

at about  $70^\circ$  to the surface normal. The sputtering rates are estimated to be in the range of 2 to 5  $\text{\AA}/\text{min}$ . Profile (a) is obtained regardless of Cs exposure time, indicating that Cs is stable only up to some critical coverage. The extremely short sputtering time necessary to completely remove the Cs is consistent with its residing only on the surface of the GaAs.

We have used the Cs exposure time necessary to reach the initial maximum in the white-light photoemission of GaAs as the unit of Cs exposure for CdTe. Exposure of CdTe for 1.5 times this long does not result in measurable white-light photoemission, but Cs is adsorbed, as shown by curve (b) of Fig. III-1, which is the Auger sputter profile taken 30 min. after cesiation. (The ordinate in this case is the Cs/Cd peak height ratio.) For an exposure of 2.5 units, white-light photoemission is observed. The sputter profile, curve (c) of Fig. III-1, shows that Cs has diffused farther into the CdTe, since a longer sputtering time is necessary to remove all the Cs. Curve (d) of Fig. III-1, the profile obtained after an exposure of 8 units, shows much deeper diffusion.

Such extensive diffusion would deplete Cs from the Cs/O surface layer used to lower  $\Phi$ , and it could also have a detrimental effect on the electrical properties of CdTe in the surface region. It thus appears that direct cesiation of CdTe is not feasible for photocathode applications, and the surface of the emitter will have to be covered with a thin metal overlayer.

Cesiation of Metals:— To be used for the surface electrode in a bias-assisted CdTe photocathode, a metal must satisfy several criteria: (1) it must be impermeable to Cs, (2) it must not diffuse into CdTe, (3) it must be able to form continuous films that are sufficiently thin ( $\lesssim 50 \text{\AA}$ ) to minimize photoelectron attenuation, (4) it must be capable of cesiation to a stable low  $\Phi$  condition, and (5) it must form a good Schottky barrier on p-CdTe; therefore, its work function should be low, preferably less than 4 eV.

In order to identify metals satisfying criterion (1), we have examined the diffusion of Cs into bulk, polycrystalline samples of the potentially useful metals Be, Mg, Al, Sc, Ti, Cr, Mn, Zr, In, and Pb (with others still to be studied) by using Ar-ion sputtering to prepare atomically

clean surfaces, exposing these surfaces to large amounts of atomic Cs, and then Auger sputter profiling. For most of the metals studied, the behavior of the white-light photoemission is similar to that observed for GaAs, except that after the maximum is reached the emission stabilizes at some lower value, rather than falling to zero. After Cs exposure is stopped, the photoresponse rises slowly to a stable value, often close to the initial maximum. Four representative Auger profiles obtained after equilibration are shown in Fig. III-2, where the ratios of Cs to metal Auger peak heights are plotted vs 500-eV Ar-ion sputtering time. For Cr (and also for Al and Mn), the time necessary to remove the Cs is extremely short, indicating that Cs resides only on the surface; this behavior is ideal for photocathode applications. For Ti (as well as In and Sc), there appears to be deeper penetration of Cs, but still no marked diffusion. The difference in the profiles for these metals may be partly due to a difference in sputtering rates, which may vary by a factor of 3 or so. For Pb and Mg (and also Sr), the profiles show Cs diffusion well below the surface (the sputtering rates are probably in the range of 2 to 5 Å/min.); these metals are thus poor candidates for overlayers on CdTe photoemitters. The profile for Be lies between those for Ti and Mg.

Since Cs diffusion is small for Al, Cr, and Ti, we have determined the optimum cesiation procedures (i.e., sequence of Cs and O<sub>2</sub> exposures) for these metals, and we have measured the work functions of the cesiated surfaces by ultraviolet photoemission spectroscopy. A typical cesiation procedure, for Al, is shown in Fig. III-3, where the white-light photoemission is plotted vs processing time; the times at which the Cs and O<sub>2</sub> sources were turned on and off are indicated. (There is about a 10-sec delay between the nominal on and off times for the resistance-heated Cs source and the actual beginning and end of Cs atom production.) The first Cs exposure is stopped close to the initial emission maximum, after which O<sub>2</sub> is admitted at a pressure of  $2 \times 10^{-8}$  Torr until a second, higher maximum is reached. Additional Cs and O<sub>2</sub> exposures produce only minor changes in the photoemission.

The values of  $\phi$  measured for the freshly cesiated surfaces of Ti, Al, and Cr were 1.4, 1.4, and 1.6 eV, respectively. Since the L<sub>6</sub> band minimum in CdTe is calculated to be 1.35 eV above the  $\Gamma_6$  minimum,<sup>6</sup> these  $\phi$  values should permit NEA to be achieved with respect to the L<sub>6</sub> minimum no matter how much band bending is induced by the metal overlayer. The three cesiated surfaces were affected differently by being left in the vacuum system overnight. For Ti,  $\phi$  remained 1.4 eV and the white-light photoemission only decreased to 90 percent of its initial value, indicating that the cesiated surface is quite stable. For Al,  $\phi$  increased to 1.6 eV and the photoemission decreased to 60 percent of its initial value. For Cr, however,  $\phi$  increased to 1.7 eV and the photoemission dropped to only 4 percent of its initial value, which is unacceptable behavior for device applications. Studies are continuing on the cesiation of other metals (e.g., Sc and Mn) which did not show significant Cs diffusion.

Schottky Barriers on p-CdTe:— An investigation of the Schottky barriers formed by various metals on heavily doped p-CdTe ( $p = 6 \times 10^{17} \text{ cm}^{-3}$ ) was initiated. The barriers formed by In, which we have used in the past to examine the electrical properties of p-CdTe, have very good diode characteristics just after plating or evaporation, but the breakdown properties degrade considerably after a few weeks at room temperature. In addition, evaporated In films are not continuous unless they are very thick (700 to 1000 Å) and, therefore, would not be useful as photoemitter overlayers. Figure III-4 shows current-voltage characteristics of 150- $\mu\text{m}$ -diameter Schottky barriers on p-CdTe made from evaporated Al, sputtered Ti, and evaporated Cr. Both

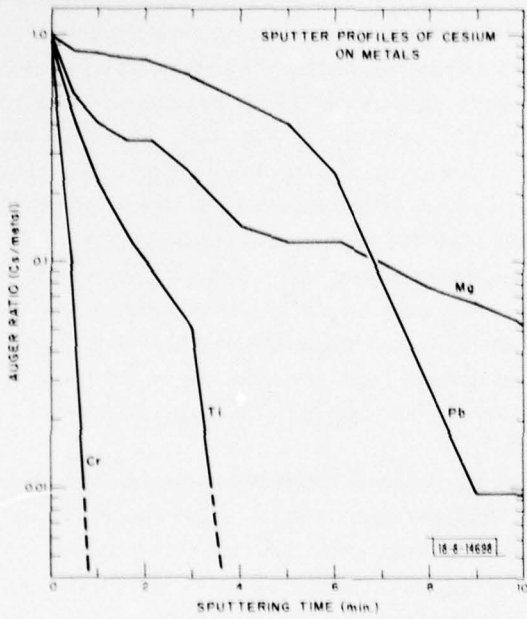


Fig. III-2. Auger Cs/metal peak height ratios vs sputtering time from Cr, Ti, Pb, and Mg surfaces after exposure to atomic Cs vapor.

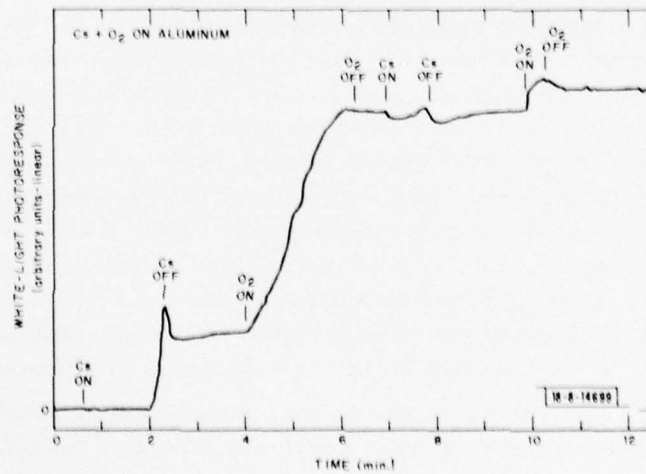


Fig. III-3. White-light photoresponse vs processing time for Al exposed successively to Cs and O<sub>2</sub>.

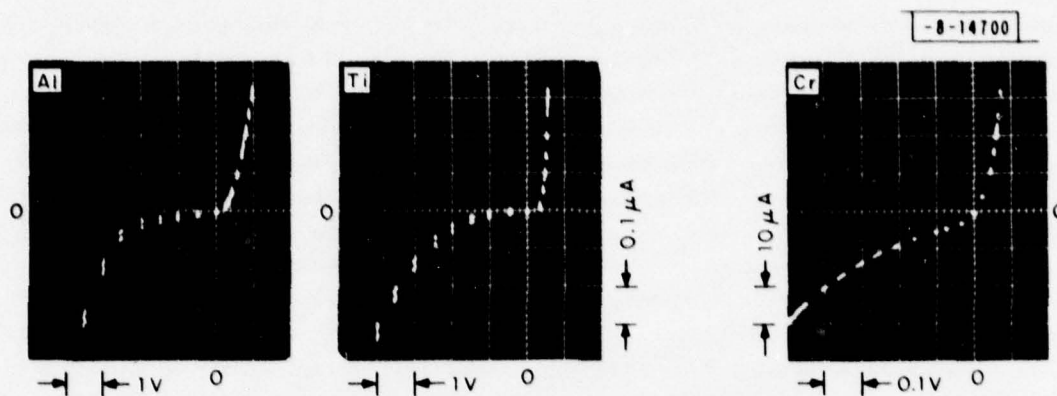


Fig. III-4. Current-voltage characteristics of 150- $\mu\text{m}$ -diameter Schottky barrier diodes formed by Al, Ti, and Cr on p-CdTe ( $6 \times 10^{17} \text{ cm}^{-3}$ ).

the Al and Ti diodes show very low dark currents ( $\sim 10^{-4} \text{ A/cm}^2$ ) at 1-V reverse bias. Their overall behavior is very similar to that observed for freshly deposited In barriers. In contrast, Cr does not yield a good Schottky barrier on p-CdTe, as is shown by the large reduction in current and voltage scales for the Cr diode in Fig. III-4. The poor Cr barrier is to be expected, since the value of  $\Phi$  for Cr (4.5 eV) is significantly higher than those for Al (4.3 eV), Ti (4.3 eV), or In (4.1 eV) (Ref. 7).

The effect of aging on Al and Ti Schottky barriers is being investigated, as is the continuity of thin Al and Ti films. In addition, we will explore the properties of Schottky barriers on p-CdTe formed by other potentially useful metals such as Sc and Mn.

V. E. Henrich  
D. L. Spears

#### B. SYNTHESIS AND CRYSTAL GROWTH OF $\text{CdGeP}_2$

Like the other II-IV- $\text{V}_2$  compounds,  $\text{CdGeP}_2$  has the tetragonal chalcopyrite structure, which is derived from the cubic zincblende structure of the III-V compounds by the ordered substitution of Group II and Group IV atoms on the Group III sublattice. The possibility of developing a tunable infrared filter that utilizes the electrooptic and birefringent properties of one of the I-III- $\text{VI}_2$  or II-IV- $\text{V}_2$  chalcopyrites is under investigation at Hughes Research Laboratories under ARPA sponsorship. To determine which of these materials would be most suitable for this application, the values of their electrooptic coefficients must be compared. At the outset of the filter investigation, however, these values were not known for  $\text{CdGeP}_2$  and many of the other chalcopyrites, and single-crystal samples large enough ( $\sim 1 \text{ cm}$  on a side) for electrooptic measurements were not available. In order to provide such a sample of  $\text{CdGeP}_2$ , we have developed a technique for the synthesis and crystal growth of this compound. A crystal whose size and optical transmission considerably exceed the minimum requirements has been obtained by this technique and supplied to Hughes for measurement.

Techniques have been reported in the literature for obtaining  $\text{CdGeP}_2$  crystals by chemical vapor transport, growth from Pb or Sn solutions, and growth from stoichiometric melts prepared by direct reaction of the elements. We selected the latter method as the only one that could potentially yield crystals of the size and optical quality required. Synthesis of the compound by direct reaction is made difficult, however, by the high vapor pressure of elemental P,

which reaches many atmospheres at temperatures far below the melting point of  $\text{CdGeP}_2$  (reported<sup>8</sup> to be  $800^\circ\text{C}$ , but close to  $794^\circ\text{C}$  according to the present investigation). A number of attempts were made to perform the reaction by weighing out the three elements in stoichiometric proportions to form a charge of about 120 g, sealing the charge in an evacuated fused-silica ampoule, then slowly heating the ampoule in a horizontal, single-zone resistance furnace. The first attempt was successful, but all the others resulted either in explosions in the vicinity of  $580^\circ\text{C}$  or in cracking of the ampoule at temperatures in the  $600$  to  $700^\circ\text{C}$  range. The explosions occurred because some of the elemental P had remained unreacted, producing a pressure that exceeded the rupture strength of fused silica, since the vapor pressure of P is about 35 atm at  $580^\circ\text{C}$ . In the other cases, the reaction between P and Cd to form  $\text{CdP}_2$  became complete at temperatures low enough to prevent the P pressure from becoming excessive, but the volatile  $\text{CdP}_2$  (which at  $600^\circ\text{C}$  has a vapor pressure of 85 Torr, very close to the value for Cd) condensed at a cold region on the ampoule wall to form a dense ring that on further heating expanded sufficiently to crack the ampoule.

These difficulties in synthesizing  $\text{CdGeP}_2$  have been overcome by performing the reaction in a two-zone furnace, a technique commonly used for preparing compounds with only one volatile constituent (e.g.,  $\text{InP}$  and  $\text{AgGaS}_2$ ). For such a compound, the procedure for obtaining a stoichiometric melt is in principle straightforward: the nonvolatile element(s) are placed at one end of the ampoule, this end is heated in the high-temperature zone to the melting point of the compound, and the other end is heated in the low-temperature zone to the temperature at which the vapor pressure of the volatile element equals the partial pressure of that element in equilibrium with the melt of the compound. Such a procedure could not be used to synthesize  $\text{CdGeP}_2$ , however, because the volatility of Cd and  $\text{CdP}_2$  (as well as P) would lead to the separation of Cd and P from the nonvolatile Ge, with the latter remaining in the high-temperature zone and the phases containing Cd and P condensing in the low-temperature zone. It was therefore necessary to devise a considerably more complicated heating schedule, as described below.

The procedure finally adopted for the synthesis and crystal growth of  $\text{CdGeP}_2$  is as follows. A stoichiometric charge of about 120 g is sealed in an evacuated fused-silica ampoule 3 cm in i. d. and 40 cm long, with the Ge at one end and the Cd and P at the other. A fused-silica rod 6 mm in diameter is attached to the Ge end of the ampoule for use in rotating the ampoule during synthesis in order to mix the melt. The ampoule is placed in the horizontal two-zone furnace shown schematically in Fig. III-5, with the Ge located in the zone at the left side of the diagram. We shall refer to this zone as the reaction zone and refer to the one on the right side as the control zone. Initially the furnace is heated for about 8 hr to give the temperature profile indicated by the solid line in Fig. III-5, with the reaction zone and the coldest point in the control zone both at about  $530^\circ\text{C}$ , where the vapor pressure of P is about 15 atm. The minimum temperature in the control zone is established at some distance from the end of the ampoule in order to prevent condensation of P or  $\text{CdP}_2$  at the end, which could lead to cracking of the ampoule. After about 16 hr the reaction zone is heated at  $\sim 8^\circ\text{C}/\text{hr}$  to  $720^\circ\text{C}$  ( $20^\circ\text{C}$  above the lowest eutectic temperature in the  $\text{CdP}_2$ -Ge pseudobinary system), while the minimum control-zone temperature is kept constant, giving the profile indicated by the dashed line in Fig. III-5. The reaction-zone temperature is then increased at  $\sim 3^\circ\text{C}/\text{hr}$  and the minimum control-zone temperature at  $\sim 11^\circ\text{C}/\text{hr}$ , so that both zones reach the melting point of  $\text{CdGeP}_2$  at about the same time. Finally, the reaction zone is rapidly heated to  $815^\circ\text{C}$  and the control zone to  $835^\circ\text{C}$ ,

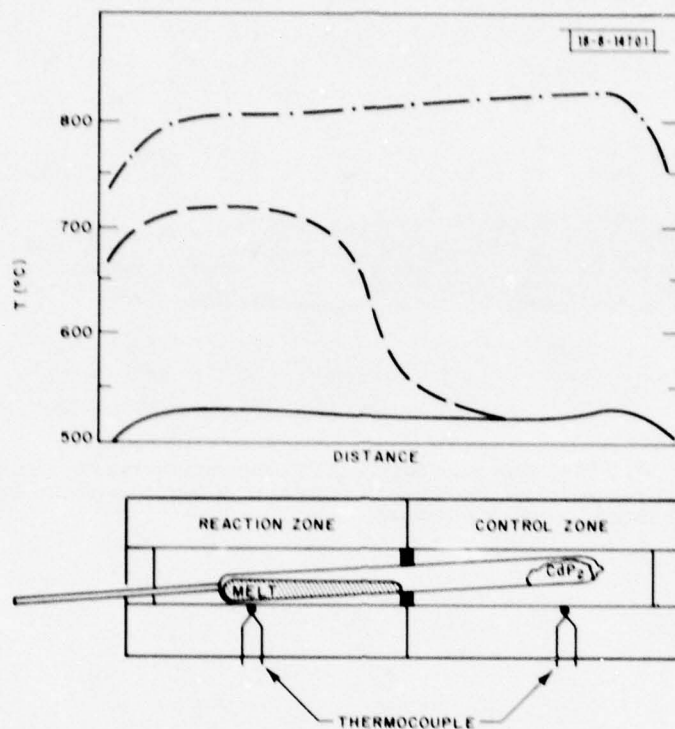


Fig. III-5. Schematic diagram of two-zone furnace for synthesis and crystal growth of  $\text{CdGeP}_2$ , together with temperature profiles at three different stages of a synthesis run.

giving the profile indicated by the dot-dashed line in Fig. III-5, in order to insure that the only condensed phase is the  $\text{CdGeP}_2$  melt in the reaction zone, which is therefore stoichiometric except for the amount of  $\text{CdP}_2$  in the vapor phase. The total time required to reach this point is about 72 hr. Directional solidification of the melt is then accomplished by lowering the temperature of the reaction zone at  $\sim 2^\circ\text{C/hr}$ , causing the melt to solidify from the left end at a rate of  $\sim 1\text{ cm/hr}$ , while the temperature of the control zone is kept constant. After solidification is completed, the furnace is cooled to room temperature in about 2 days.

The procedure described has been used for six runs, all of which were completed successfully without explosion or cracking. The ingots obtained are polycrystalline, but all contain sizable single-crystal regions. They are all rather badly cracked, a characteristic property of polycrystalline chalcopyrites. The cracks are produced during cooling by strains that develop at the grain boundaries because the thermal expansion of this structure is highly anisotropic. Figure III-6 is a photograph of the best ingot; much of the surface structure is due to growth facets rather than to grain boundaries. Figure III-7 is a photograph of a sample 3 cm long, cut from the left end of this ingot, that is almost entirely a single crystal. The cracks at the top originated at the only grain boundary present in the sample. (The location of the sample in the ingot can be found from the arrows in Figs. III-6 and -7, which point to the same growth feature.)

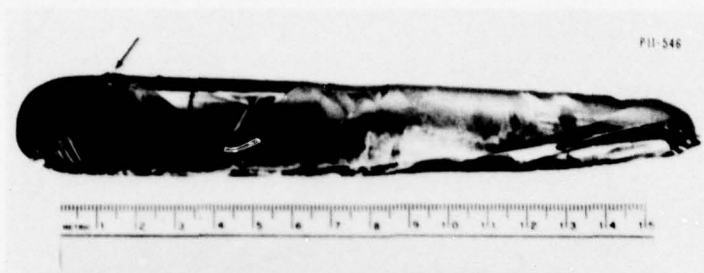


Fig. III-6. As-grown ingot of CdGeP<sub>2</sub> prepared by the two-furnace technique. Much of the surface structure is due to growth facets rather than to grain boundaries.

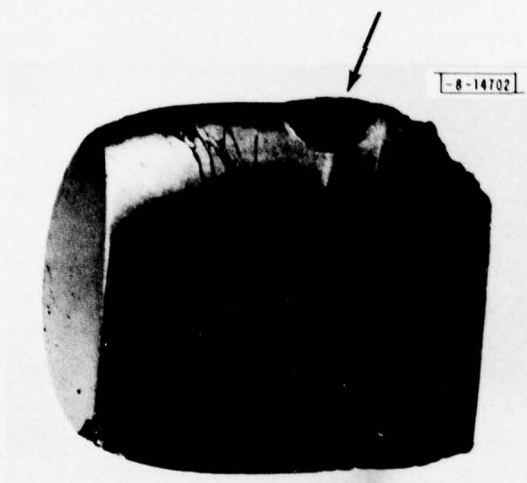


Fig. III-7. Sample 3 cm long cut from left end of ingot shown in Fig. III-6. The arrows in both figures point to the same growth feature.

Thin sections cut from the ingots were found to be generally transparent when examined with an infrared microscope, but contained numerous absorbing areas of micrometer dimensions. Electron microprobe analysis showed that most of these areas, which are presumably inclusions or precipitates, are nearly pure Cd, while a few are nearly pure Ge. For a section 0.9 mm thick cut from the ingot of Fig. III-6, measurements made with an infrared spectrophotometer showed the transmission to be reflectivity limited within the accuracy of the data over the wavelength range from about 2  $\mu\text{m}$  to the onset of lattice absorption at about 11  $\mu\text{m}$ . Between the intrinsic absorption edge at about 0.7 and 2  $\mu\text{m}$  there was significant absorption, which was probably due to scattering. There was no evidence of free-carrier absorption, consistent with electrical measurements that showed the resistivity to be at least  $10^9 \Omega\text{-cm}$ , the upper limit of the measuring equipment. Measurements of the transmission through the whole length of the crystal in Fig. III-7 gave an optical absorption coefficient of only  $0.4 \text{ cm}^{-1}$  at 5  $\mu\text{m}$ . This crystal has been sent to Hughes Research Laboratories to provide samples for measurement of the electrooptic coefficient.

P. Vohl

#### REFERENCES

1. I. Melngailis, "The Graded-Gap Semiconductor Photoemitter," Technical Note 1971-8, Lincoln Laboratory, M.I.T. (22 January 1971), DDC AD-720796.
2. Solid State Research Report, Lincoln Laboratory, M.I.T. (1976:3), p. 35, DDC AD-A034647/8.
3. R. L. Bell, L. W. James, and R. L. Moon, *Appl. Phys. Lett.* 25, 645 (1974).
4. A. H. Sommer, *Photoemissive Materials* (Wiley, New York, 1968), p. 179.
5. N. D. Lang, *Phys. Rev. B* 4, 4234 (1971).
6. D. J. Chadi, J. P. Walter, M. L. Cohen, Y. Petroff, and M. Balkanski, *Phys. Rev. B* 5, 3058 (1972).
7. H. B. Michaelson, *J. Appl. Phys.* 48, 4729 (1977).
8. K. Masumoto, S. Isomura, and W. Goto, *J. Phys. Chem. Solids* 27, 1939 (1966).

#### IV. MICROELECTRONICS

##### A. ORIENTED CRYSTAL GROWTH ON AMORPHOUS SUBSTRATES USING ARTIFICIAL SURFACE-RELIEF GRATINGS

The nucleation and growth of crystalline overlayers are influenced by accidental structural features on a substrate surface, such as cleavage steps, scratches, pits, etc.<sup>1,2</sup> The influence of such structural features on overlayer properties has always been considered detrimental and, thus, workers have generally tried to achieve totally smooth substrate surfaces. We propose that artificially created surface microstructures might be employed to manipulate the growth and orientation of crystalline overlayers. One outcome of this approach might be a method of obtaining oriented crystalline films on substrates and under growth conditions that otherwise yield polycrystalline films. As an example of this, we demonstrate that a 320-nm spatial-period surface-relief grating etched into amorphous  $\text{SiO}_2$  induces an orientation in KCl crystallites grown from a water solution.

Figure IV-1 is a scanning-transmission-electron micrograph showing the KCl crystallites after growth on a surface-relief grating in amorphous  $\text{SiO}_2$ . The sides of nearly all the rectangular KCl crystallites are aligned parallel and perpendicular to the surface grating. The smaller crystallites are generally located in grooves (the lighter shaded stripes), and it appears that growth is initiated at vertical steps. Selected-area electron diffraction patterns taken in a scanning-transmission-electron microscope (STEM) confirm one's intuition that the  $\langle 100 \rangle$  directions are parallel to the sides of the crystallites. Clearly, the artificially imposed

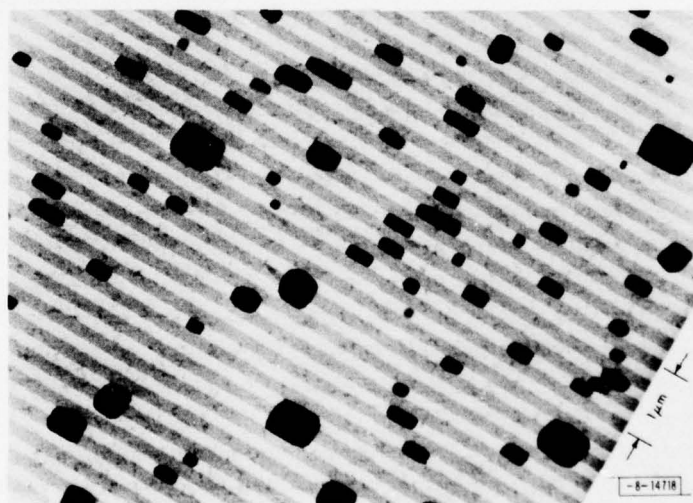


Fig. IV-1. Scanning-transmission-electron micrograph of KCl crystallites grown on a 320-nm spatial-period square-wave surface-relief grating in amorphous  $\text{SiO}_2$  showing that the grating has induced an oriented crystal growth where  $\langle 100 \rangle$  directions are parallel to the grating grooves. The grooves are 25 nm deep and have the lighter shading. The electron microscopy produces some decomposition of the KCl crystallites during viewing, leading to the serrated edges of some of the crystallites.

surface-relief grating has induced an oriented crystal growth. In areas of the  $\text{SiO}_2$  surface where no surface grating is present, crystallite habit (i.e., shape) is found to be less regular, and  $\langle 100 \rangle$  directions show no preferential azimuthal orientation. These results are the first demonstration of crystal orientation using artificial surface microstructures and are also a clear demonstration of oriented crystal growth (i.e., heteroepitaxy) on an amorphous substrate.

Our  $\text{SiO}_2$  substrates were films, about 100 nm thick, grown by a commercial chemical-vapor-deposition (CVD) process over a 100-nm-thick  $\text{Si}_3\text{N}_4$  film, also grown by a commercial CVD process, on a silicon wafer. Details of the techniques used to create the relief grating in  $\text{SiO}_2$  are given elsewhere.<sup>3,4</sup> In brief, a grating was exposed in PMMA using  $\text{Cu}_L$  x-ray lithography. After development, a 10-nm layer of chromium was evaporated over the structure and a chromium grating produced by liftoff. The  $\text{SiO}_2$  was then etched in  $\text{CHF}_3$  by reactive ion etching using the chromium grating as a mask. Finally, the chromium was removed in a chemical etchant. This procedure yields relief gratings having flat tops and flat groove bottoms and sidewalls that deviate a maximum of about  $6^\circ$  from the vertical. The radii of curvature at the corners where the sidewalls join the tops and the groove bottoms are less than 5 nm. The depth of the gratings used in the KCl experiments ranges from 25 to 50 nm. After producing the surface-relief grating, the silicon underlying the  $\text{Si}_3\text{N}_4$  and  $\text{SiO}_2$  films was etched away using ethylene diamine pyrocatechol in water.<sup>5</sup> The sample was held in a special fixture to avoid any etching of the front surface. The KCl was grown by flooding the  $\text{SiO}_2$  grating with a solution of KCl in water and then blowing nitrogen gas over it to promote evaporation, supersaturation, and crystal growth. Crystal orientation in the grating area was uncorrelated with the blowing direction. Because our  $\text{SiO}_2/\text{Si}_3\text{N}_4$  substrates were only about 200 nm thick, they could be viewed in transmission by electron microscopy using both conventional and STEM systems. The STEM permitted selected-area electron diffraction, although the signal-to-noise ratio was poor.

The results shown in Fig. IV-1 indicate that the surface-relief grating influences both the nucleation and the growth of the KCl. Nucleation appears to occur preferentially at vertical steps, and subsequent growth is constrained and aligned by the steps. Preferential nucleation at naturally occurring cleavage steps (usually called "decoration") has been observed for many crystalline film-substrate combinations including Au on NaCl (Ref. 6), Au on LiF (Ref. 7), Ag on NaCl (Ref. 8), Sn on NaCl (Ref. 9), Ag on mica,<sup>8</sup> and Au on graphite,<sup>10</sup> and has been explained qualitatively using classical nucleation theory, with the assumption of isotropic surface tensions.<sup>7</sup> On the basis of this simplified theory, one can expect decoration of artificially created surface-relief steps on amorphous substrates if the radius of curvature at the base of the step is sufficiently small compared to the size of the critical nucleus, and if the contact angle of the deposit is  $< 100^\circ$ . An extension of the theory predicts that KCl will decorate steps on  $\text{SiO}_2$ .

The grating's orienting influence on the KCl growth can be explained on the basis that oriented growth corresponds to a minimum free energy configuration. When grown on smooth amorphous substrates, most alkali halides, including KCl, form textured films with  $\{100\}$  planes parallel to the substrate surface,<sup>11</sup> indicating that surface free energy is minimum for this particular texture. Our surface-relief grating consists of flat tops, flat groove bottoms, and nearly vertical sidewalls, and thus a crystal would have a higher free energy if it grows misaligned relative to such a structure than if it grows aligned. Our method of growing the KCl by evaporation of a solution is far from an equilibrium process. However, the KCl deposit

was "annealed" after growth by placing it in a humid atmosphere for a few minutes prior to storage in a dessicator. Because of the islands' small size, we feel this annealing was sufficient to establish equilibrium.

Many polycrystalline thin films exhibit a texture when deposited on smooth amorphous substrates such that the most densely packed planes are generally parallel to the substrate surface.<sup>11</sup> Our technique may be effective in inducing azimuthal alignment in such cases as well.

The above results are an example of how the growth and orientation of an overlayer can be manipulated by an artificially created microstructure on a substrate surface. Since the spatial period, symmetry, cross-sectional profile, and overall pattern configuration of artificial microstructures are subject to one's control, and since many aspects of overlayer growth and orientation are affected by surface structure, manipulation using artificial microstructures may be of rather general applicability and contribute to both the technology and the basic science of overlayer growth. Precisely how growth might be manipulated for any given overlayer/substrate combination will depend on the geometry of the microstructure, the method and conditions of the deposition, and the detailed mechanisms of nucleation and growth.<sup>12</sup>

H. I. Smith  
D. C. Flanders

#### B. FABRICATION OF VERTICAL-SIDEWALL PATTERNS IN GLASS FILMS ON GaAs SUBSTRATES

Reactive ion etching has been combined with plasma etching to produce submicrometer-geometry patterns in glass films on GaAs substrates. Figure IV-2 shows the film configurations

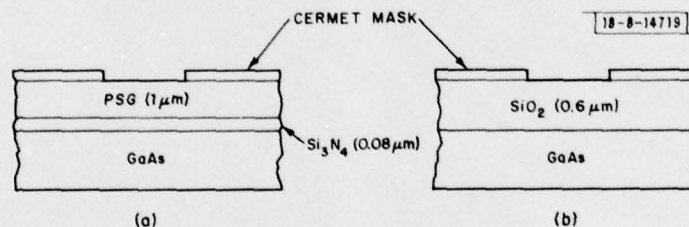


Fig. IV-2. Cross section of glass/GaAs films to be patterned by the combination of reactive ion etching and plasma etching showing cermet mask already etched. (a) is a PSG/Si<sub>3</sub>N<sub>4</sub> film used as an ion-implantation mask and (b) is an SiO<sub>2</sub> film used as a plating mask.

investigated: a phosphosilicate glass (PSG)/Si<sub>3</sub>N<sub>4</sub> film similar to those used as a selective ion-implantation mask in the fabrication of FETs [Fig. IV-2(a)]; and a CVD SiO<sub>2</sub> layer such as those used as electroplating masks in the fabrication of submicrometer Schottky-barrier diodes [Fig. IV-2(b)]. Previously these films were etched using wet chemical or plasma etching techniques. However, the undercutting which occurred during the etching process caused sloping sidewalls and a large variability in pattern size.

Both applications mentioned above would benefit greatly from steep-edged walls and precise dimensional control. Reactive ion etching has previously been used to achieve these goals in

TABLE IV-1 REACTIVE-ION-ETCHING PARAMETERS			
		Removal Rates ( $\text{\AA}/\text{min.}$ )	
		Gas	$\text{CHF}_3$
Gas Pressure	0.01 Torr	GaAs	173
Gas Flow Rate	15 scc/min.	PSG	300
Target Power Density	$0.3 \text{ W}/\text{cm}^2$	$\text{SiO}_2$ (CVD)	300
		$\text{Si}_3\text{N}_4$	>700

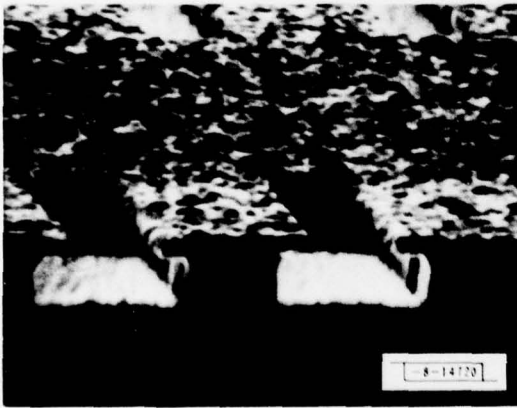


Fig. IV-3. Line etched in glass film on GaAs by reactive ion etching followed by sprayed, buffered HF etching of final  $1000 \text{ \AA}$  of PSG. The  $1\text{-}\mu\text{m}$ -wide line has been undercut beneath the cermet mask. The surface roughness originates from the original roughness of surface of the PSG layer.

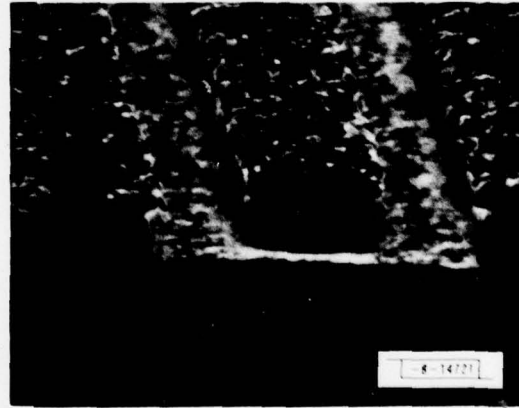


Fig. IV-4. Another section of the same wafer as shown in Fig. IV-3 with the final  $1000 \text{ \AA}$  of PSG film removed by plasma etching. Note the maintenance of the  $1\text{-}\mu\text{m}$  line and space as compared with Fig. IV-3. Cermet mask is still in place on glass film.

etching vertical-sidewall relief gratings in SiO<sub>2</sub> (Refs. 3 and 13), but the use of this technique alone to pattern films on GaAs produces poor results. When the etching reaches the glass film/GaAs interface, rapid etching of the GaAs substrate occurs which renders the substrate useless for subsequent device fabrication.

In order to overcome the problem of damage to the GaAs substrate, the following modifications to a reactive-ion-etching procedure alone were incorporated into our process. After the deposition of the glass films, the samples are overcoated with a 1500- to 2000-Å film of an RF-sputtered cermet (70% Cr<sub>2</sub>O<sub>3</sub>/30% Cr) which acts as the reactive-ion-etching mask (shown in Fig. IV-2). The desired pattern is then defined in photoresist and the cermet film is patterned with a commercial chromium etch. After stripping the photoresist, the PSG or SiO<sub>2</sub> is reactively ion etched until approximately 1000 Å of the PSG or SiO<sub>2</sub> remains, thus avoiding any damage to the GaAs. The reactive-ion-etching parameters and the measured etch rates are shown in Table IV-1.

Figure IV-3 shows a PSG/Si<sub>3</sub>N<sub>4</sub> sample in which the remaining PSG layer was removed by spraying buffered hydrofluoric acid. The Si<sub>3</sub>N<sub>4</sub>, because of its low etch rate in buffered HF, was not etched appreciably. Although the sidewalls produced by the reactive ion etching remain vertical, the chemical etching necessary to completely remove the PSG has caused significant lateral etching. This result, though not completely understood, is typical of chemically etched PSG layers. Figure IV-4 shows results obtained from the same wafer and differs only in that the remaining PSG layer was removed by plasma etching. In this case both vertical sidewalls and negligible undercutting were obtained. Plasma-etching parameters together with removal rates are shown in Table IV-2. Similar results have been obtained with the SiO<sub>2</sub> on GaAs configurations of Fig. IV-2(b).

TABLE IV-2 PLASMA-ETCHING PARAMETERS			
Equipment	IPC Model 1001B	Removal Rates (Å/min.)	
		Gas	DE 100 (CF <sub>4</sub> + 5% O <sub>2</sub> )
Gas Pressure	0.3 Torr	GaAs	Negligible
Input Power	1 W	PSG	83
Chamber Volume	0.75 liter	Si <sub>3</sub> N <sub>4</sub>	50
		SiO <sub>2</sub>	35

In addition to producing a favorable etched-wall geometry, the combination of reactive ion etching and plasma etching is also capable of precisely defining very thick pyrolytic glass layers. For example, a 1500-Å-thick layer of cermet can be used as a mask to reactively ion etch up to 1.5 μm of PSG. This cermet thickness is sufficiently thin to allow high resolution patterning. Present work in this area centers about applying this technique to other glass systems, and determining more carefully its limitations.

G. A. Lincoln      G. L. Hansell  
R. J. Reinhard    P. J. Daniels  
J. J. Lambert      R. A. Murphy

#### REFERENCES

1. K. L. Chopra, Thin Film Phenomena (McGraw-Hill, New York, 1969).
2. Handbook of Thin Film Technology, Chapters 8 and 10, edited by L. I. Maissel and R. Glang (McGraw-Hill, New York, 1970).
3. D. C. Flanders, H. I. Smith, H. W. Lehmann, R. Widmer, and D. C. Shaver, Appl. Phys. Lett. **32**, 112 (1978).
4. D. C. Flanders and H. I. Smith, J. Vac. Sci. Technol. **15**, No. 3 (May/June 1978).
5. J. C. Greenwood, J. Electrochem. Soc. **116**, 1325 (1969); A. Bohg, J. Electrochem. Soc. **118**, 401 (1971).
6. G. A. Bassett, Philos. Mag. **3**, 1042 (1958).
7. B. K. Chakraverty and G. M. Pound, Acta Metall. **12**, 851 (1964).
8. K. L. Chopra, J. Appl. Phys. **37**, 3405 (1966).
9. G. Shimaoka and G. Komoriya, J. Vac. Sci. Technol. **7**, 178 (1970).
10. G. R. Henning, Appl. Phys. Lett. **4**, 52 (1964).
11. E. Bauer, Trans. 9th Vac. Sym. AVS, 1962, edited by G. H. Bancroft (Macmillan, New York, 1962), p. 35; E. Bauer, in Single Crystal Films, edited by M. H. Francombe and H. Sato (Pergamon Press, London, 1964), p. 43.
12. D. C. Flanders, PhD Thesis, February 1978, M.I.T. Department of Electrical Engineering and Computer Science; H. I. Smith and D. C. Flanders, Appl. Phys. Lett. **32**, 349 (1978).
13. H. W. Lehmann and R. Widmer, Appl. Phys. Lett. **32**, 163 (1978).

## V. SURFACE-WAVE TECHNOLOGY

### A. SURFACE-ACOUSTIC-WAVE PROPERTIES OF FRESNOITE

Fresnoite ( $\text{Ba}_2\text{Si}_2\text{TiO}_8$ ) is a new piezoelectric crystal with a noncentrosymmetric tetragonal structure, P4bm. Growth of single crystals<sup>1,2</sup> several centimeters long and measurements of the complete elastic, piezoelectric, and dielectric constants<sup>3</sup> have been reported. We have calculated and measured surface-acoustic-wave (SAW) properties for several cuts of fresnoite and have observed efficient coupling for the z-cut, x- or y-propagating wave.

The SAW properties of fresnoite were calculated by solving the coupled electromagnetic and acoustic-wave equations subject to the appropriate boundary conditions, using a previously developed computer program<sup>4</sup> and values of the material constants measured by Kimura.<sup>3</sup> The results are shown in Fig.V-1 for eight standard cuts. Due to the symmetry of the fresnoite

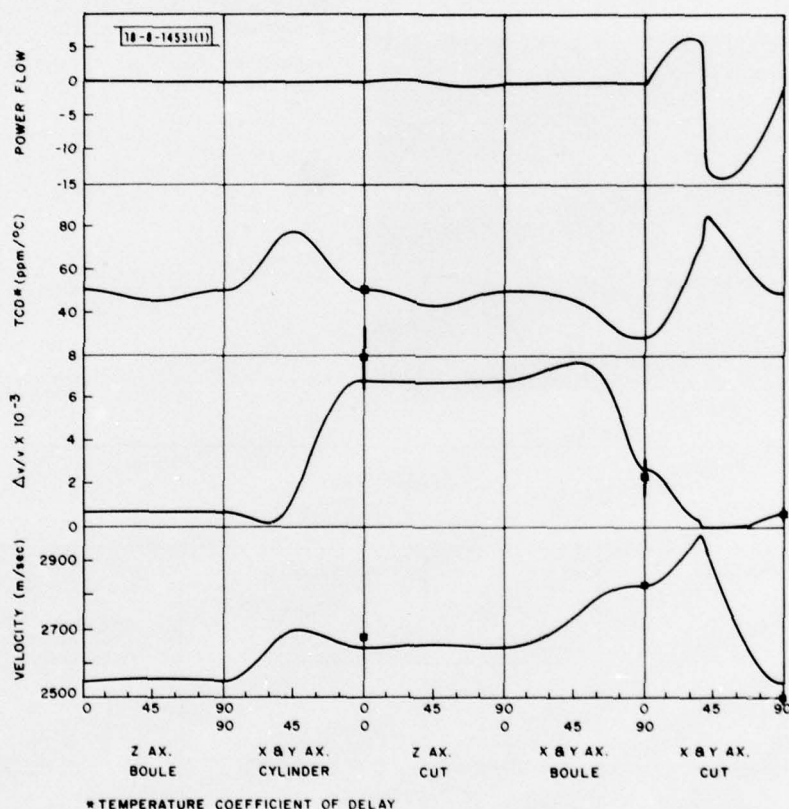
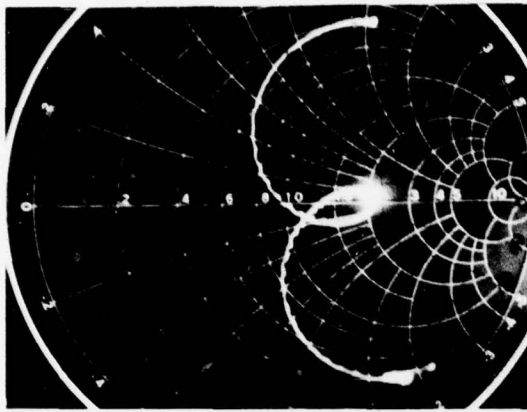
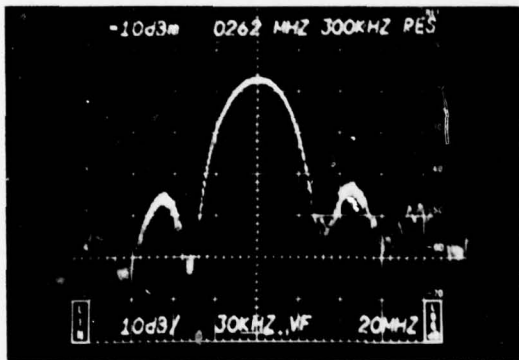


Fig. V-1. Calculated (curves) and measured (points) SAW properties of fresnoite. The power flow angle is in degrees. The usual orientation convention is used (see Ref. 6). Axis cuts refer to surfaces cut normal to the x or z crystal axis. The propagation direction is rotated between the other two axes, e.g., for x cut, 0° corresponds to y propagating and 90° to z propagating. For the x-axis boule the direction of SAW propagation is fixed along x but the normal to the surface rotates from z to y. For the x-axis cylinder the x axis is always in the plane of the surface and normal to the direction of propagation, while the surface normal rotates from y to z.



(a)



(b)

Fig. V-2. (a) Impedance plot of a z-cut, x-directed inductor-tuned transducer. The marker at resonance is at 262 MHz. The frequency is swept from 232 to 292 MHz. (b) Frequency response of z-cut, x-directed delay line with untuned transducers. The transducers have 8-1/2 finger pairs, a period  $\lambda_0$  of 10.2  $\mu\text{m}$ , and an aperture of  $100 \lambda_0$ . The input power level is 0 dBm.

TABLE V-1  
SAW PROPERTIES

	Velocity (m/sec)	Coupling Coefficient $k^2$ ( $2\Delta v/v$ )	Temperature Coefficient of Delay $\frac{1}{\tau} \frac{d\tau}{dT}$ ( $^{\circ}\text{C}$ ) <sup>-1</sup>
Fresnoite ( $\text{Ba}_2\text{Si}_2\text{TiO}_8$ ) (measured)			
z-cut, x-propagating	2678 $\pm$ 3	0.016 $\pm$ 0.003	51 $\times$ 10 <sup>-6</sup>
x-cut, y-propagating	2827 $\pm$ 3	0.0046 $\pm$ 0.0020	-
x-cut, z-propagating	2500 $\pm$ 50	0.0010 $\pm$ 0.0006	-
Lithium niobate ( $\text{LiNbO}_3$ )			
y-cut, z-propagating	3485	0.045	94
Bismuth germanium oxide ( $\text{Bi}_{12}\text{GeO}_{20}$ ) (001) cut, (110) propagating	1681	0.0136	130

lattice, all the x- and y-type orientations are equivalent. A shear-type SAW (Bleustein-Gulyaev wave) is found to exist for the x and y cuts at  $0^\circ$ , in agreement with Kimura's calculation.<sup>3</sup>

Measurements were taken on delay lines fabricated on z-cut and on x-cut polished surfaces of fresnoite. The specimens were cut from water-white crystals grown from the melt by the Czochralski method in an oxygen atmosphere. After the crystals had been cooled to room temperature in the growth furnace, they were transferred to a muffle furnace, annealed at  $1350^\circ\text{C}$  for 60 hours to remove strains, and then slowly cooled to room temperature. The interdigital transducers used had  $N = 8\text{-}1/2$  finger pairs and a period of  $\lambda_0 = 10.2 \mu\text{m}$ . The aperture or width of the acoustic beam was 1.02 mm ( $100 \lambda_0$ ). The lengths of the delay lines were 4.06 and 5.08 mm. The metal film of the transducers was formed by a deposition of  $100 \text{ \AA}$  chromium and followed by  $2000 \text{ \AA}$  aluminum.

The surface-wave parameters of the crystals were determined by measuring the properties of the delay lines and of the individual transducers. The velocity of the surface wave could be deduced from the center frequency of the passband of the delay line, from the delay measured on an oscilloscope, or, most accurately, from a measurement of the phase response over the passband. The temperature dependence of delay was assumed to be linear, and the coefficient was determined by measuring the phase response at  $25.1^\circ$  and at  $59.8^\circ\text{C}$ .

For the z-cut, x-propagating surface wave, the coupling coefficient  $k^2$  was determined from a combination of three measurements: the real part of the tuned transducer impedance at resonance, the static capacitance of the transducer fingers, and the insertion loss of the delay line with untuned transducers. In the simple series equivalent circuit of the transducer,<sup>5</sup> the acoustic resistance is  $R_a = 4k^2 N / \pi \omega C_T$ , where  $C_T$  is the total capacitance of the transducer fingers. In addition, the equivalent ohmic resistance of the fingers  $R_\Omega$  and the resistance of the tuning inductor  $R_L$  (if it is used) appear in series with  $R_a$ . From the measured sheet resistance of the metal film,  $0.16 \Omega/\text{square}$ ,  $R_\Omega$  is estimated to be  $7.5 \Omega$ , and  $R_L$  at 260 MHz is estimated from the Q of the inductor to be  $18.5 \Omega$ . From the impedance plot of a series inductor-tuned transducer [Fig. V-2(a)]  $R_a + R_L + R_\Omega = 100 \Omega$ , so  $R_a = 74 \pm 6 \Omega$  at resonance (262 MHz). The capacitance  $C_T$  was found by using a bridge at 1 MHz to measure the capacitance of the connector alone and then the connector and transducer together. The result was  $C_T = 1.35 \pm 0.25 \text{ pF}$ . The capacitance of the transducer pads was estimated to be less than  $0.1 \text{ pF}$  and was neglected. The insertion loss of the untuned delay line was 28 dB [Fig. V-2(b)] or 14 dB/transducer, assuming negligible propagation and diffraction loss. Thus,  $10 \log T = 14 \text{ dB}$ , and the expression for the transducer conversion loss,  $T = 2[(R_o + R_a + R_\Omega)^2 + X_T^2] / 2R_a R_o$ , can be used to determine  $R_a$ . Here  $R_o = 50 \Omega$  and  $X_T = 1/\omega C_T$ . The coupling coefficient can be determined from any pair of the three measured quantities,  $R_a$ ,  $C_T$ , and  $T$ . The value is found to be  $k^2 = 0.016 \pm 0.003$ . All three ways of calculating  $k^2$  yield values well within the error limits.

All the measured SAW properties are seen to be in agreement with the calculated results (Fig. V-1). They are compared with the properties of standard cuts of lithium niobate and bismuth germanium oxide (BGO) in Table V-1 (see Ref. 6).

The shear, or at least non-Rayleigh, character of the x-cut, y-propagating surface wave is partly confirmed by the following observation: surface films such as condensed water vapor or vacuum grease, which are known to be strong attenuators of Rayleigh waves, reduced the signal in the z-cut, x-propagating and x-cut, z-propagating delay lines by more than 40 dB, but the same films on the x-cut, y-propagating delay line produced only a few decibels reduction in signal.

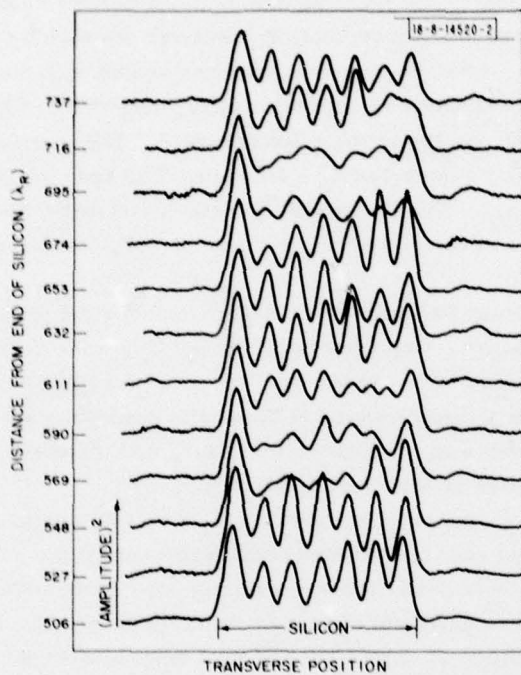


Fig. V-3. Surface-wave beam profile in silicon-LiNbO<sub>3</sub> waveguide having 6.5- $\mu$ m-wide rails on 102- $\mu$ m centers.

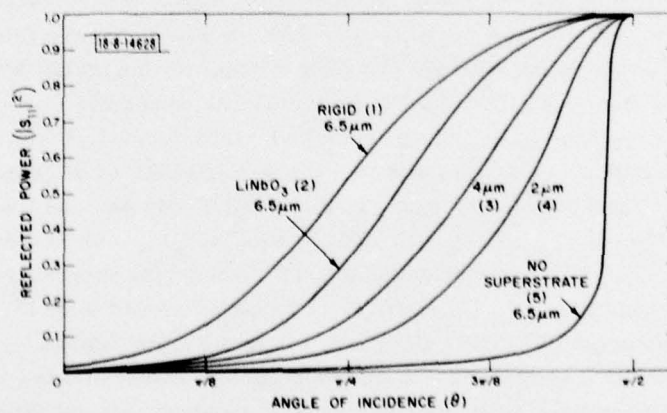


Fig. V-4. Reflection of Rayleigh wave by a (1) totally rigid rail; (2) 6.5- $\mu$ m-, (3) 4- $\mu$ m-, and (4) 2- $\mu$ m-wide rails with a silicon superstrate; and (5) a 6.5- $\mu$ m-wide rail with no superstrate.

Fresnoite promises to be a useful SAW substrate material. The coupling coefficient for the z-cut, x-propagating wave is comparable to that of BGO and is calculated to be about 10 percent higher yet for the x-axis boule cut at 45°, while the velocity is intermediate between that of BGO and LiNbO<sub>3</sub>. The dielectric constant<sup>1,3</sup> is a factor of 2 to 3 lower than for the other two substrates. Therefore fresnoite may prove to be useful as a substrate for the silicon air-gap type SAW convolvers. In fact, preliminary calculations indicate that the convolver efficiency M is 5 to 6 dB higher with fresnoite than with LiNbO<sub>3</sub> for the same convolution time and operating frequency.

J. Melngallis	T. B. Reed
J. F. Vetelino†	R. E. Fahey
A. Jhunjhunwala†	E. Stern

## B. ANALYSIS OF PROPAGATION MODES IN CONVOLVERS

Measurements of acoustic-wave propagation in gap-coupled acoustoelectric convolvers<sup>7</sup> which employ rail support structures<sup>8</sup> show distinctive beating phenomena between two acoustic modes. These phenomena have been analyzed and measured for a silicon superstrate supported above a LiNbO<sub>3</sub> substrate. Optical-probe measurements of acoustic-beam profiles in such structures show that the acoustic field repeats spatially in a periodic fashion (Fig. V-3). The profiles at 506 and 632 Raleigh wavelengths ( $\lambda_R$ ) show fairly well-formed nulls at the rail positions, while the profiles at 569 and 695  $\lambda_R$  show a more uniform power distribution across the beam. The spatial periodicity of this pattern down the length of the propagation path is the beat length ( $L_B$ ) between modes of the structure. The beating between two or more modes causes a ripple in the frequency response of the acoustic delay line formed by placing an acoustic transducer at each end of the structure. Beat lengths of 137  $\lambda_R$  have been obtained from both optical-probe and frequency-response data on a convolver having 6.5- $\mu$ m-wide support rails on 100- $\mu$ m centers.

The rail support structure has been modeled as a periodically loaded transmission line. The rails appear as discrete elements in the transmission-line model, which is justified because their width ( $\leq 0.5 \lambda_R$ ) is small compared with the transverse wavelength. The model predicts the fraction of reflected acoustic power  $|S_{11}|^2$  as a function of rail width and the angle of incidence  $\theta$  (Fig. V-4). As expected,  $|S_{11}|^2$  increases with angle of incidence and approaches unity at grazing incidence ( $\theta = \pi/2$ ).

The stiffness of the silicon superstrate is primarily responsible for the scattering of Rayleigh waves. For example, by letting the superstrate become infinitely stiff (curve 1 of Fig. V-4) the reflection increases. On the other hand, removal of the superstrate (curve 5), leads to a dramatic decrease in the reflectivity. The residual effect is due to the presence of the rails alone. The effect of the superstrate is to deaden the surface vibration. This effect is enhanced by a wider rail as evident in curves 2, 3, and 4, where the width is changed from 6 to 4 and then to 2  $\mu$ m. Although not shown in Fig. V-4, the phase of the reflected wave generally decreases along with a decrease in the magnitude of the reflection. An exception is the case of no superstrate.

Each rail appears as a two-port junction in the transmission-line model. For a symmetric structure, the incident-wave amplitudes ( $a_1$  and  $a_2$ ) and scattered-wave amplitudes ( $b_1$  and  $b_2$ ) are related by a scattering matrix  $\bar{S}$  (Ref. 9).

† Department of Electrical Engineering, University of Maine.

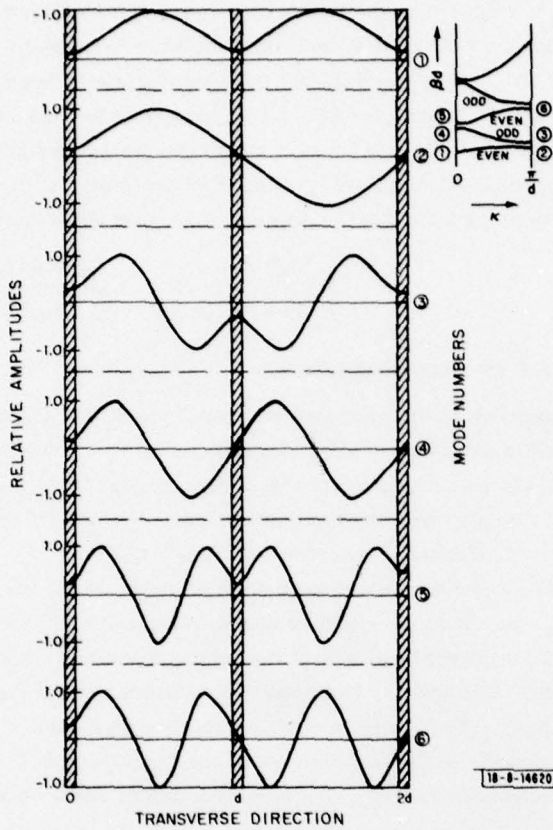


Fig. V-5. Dispersion diagram and modes of a typical periodic structure.

TABLE V-2  
THEORETICAL WAVEGUIDE DATA FOR AN ARRAY OF SUPPORT RAILS

Rail Support		No. 1 Fundamental Mode		No. 5 Higher-Order Mode		Interaction	
Width ( $\mu\text{m}$ )	Spacing ( $\mu\text{m}$ )	$\beta_1 d$	$ S_{11} ^2$	$\beta_5 d$	$ S_{11} ^2$	$L_B (\lambda_R)$	M (dB)
4	363	3.09	0.99	9.27	0.99	1119	1.9
6.5	100	3.06	0.99	9.18	0.98	86	1.9
4	100	2.96	0.99	8.89	0.92	92	1.8
2	100	2.84	0.98	8.56	0.82	99	1.6
2	30	2.35	0.84	7.47	0.28	11	0.7

$\lambda_R = 11 \mu\text{m}$

$$\begin{bmatrix} b_1 \\ b_2 \end{bmatrix} = \begin{bmatrix} S_{11} & S_{12} \\ S_{12} & S_{11} \end{bmatrix} \begin{bmatrix} a_1 \\ a_2 \end{bmatrix} . \quad (V-1)$$

The form of Eq. (V-1) is consistent with reciprocity and symmetry. Also, energy conservation imposes the condition

$$|S_{11}|^2 + |S_{12}|^2 = 1 . \quad (V-2)$$

With a periodically loaded structure such as the support rails on an acoustic delay line, the wave at junction  $(n + 1)$  can differ from the wave at junction  $n$  by at most a phase delay  $(Kd)$ , where  $d$  is the spacing between adjacent rails.

An eigenvalue equation,

$$\cos Kd = \frac{1}{2S_{12}} \left[ e^{j\beta_1 d} + (S_{12}^2 - S_{11}^2) e^{-j\beta_1 d} \right] \quad (V-3)$$

for  $K$  was obtained with  $\beta_i$  being the transverse propagation constant of the  $i^{\text{th}}$  acoustic mode.<sup>9</sup>

Solution of Eq. (V-3) for a typical periodic structure yields a dispersion diagram as shown in Fig. V-5. It shows "bands" of alternating even and odd symmetry as exhibited by the mode pattern at the Brillouin zone center ( $K = 0$ ) and edge ( $K = \pi/d$ ). These two points are of particular interest to us because we accept as modes only those solutions which have vanishing group velocity. With a uniform excitation of the periodic rail structure, we expect from symmetry that the acoustic wave is the superposition of standing waves in the transverse direction. Furthermore, because of the assumed uniform transducer input, only symmetric modes such as modes 1 and 5 could be excited. We will refer to these modes as the fundamental mode (No. 1) and the higher-order mode (No. 5). These two modes are most strongly excited and the beating between them gives rise to the observed spatial and frequency ripples.

A summary of the data obtained from the theoretical model is given in Table V-2. As the width of the rails is reduced, the magnitude  $|S_{11}|^2$  and the phase of the reflected power are reduced. This allows the fundamental mode, sketched in Fig. V-6, to spread out more uniformly across the acoustic beam path. Hence, with a lower reflectivity, more of the acoustic energy

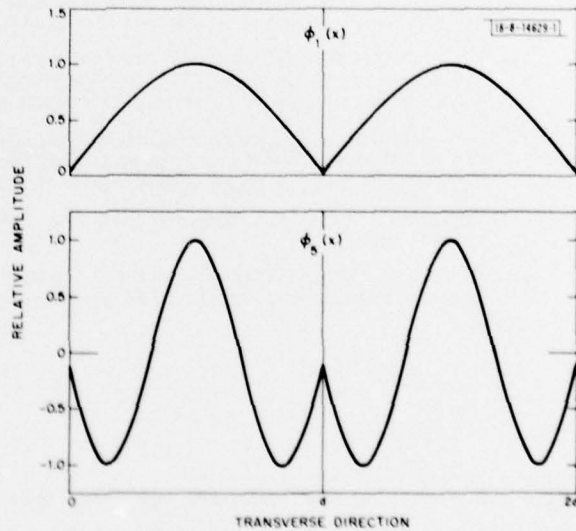


Fig. V-6. Mode profile for a 6.5- $\mu\text{m}$  rail structure with 100- $\mu\text{m}$  spacing.

from the uniform transducer will be coupled into the fundamental mode 1 and less into the first higher-order symmetric mode 5. Therefore, the amplitude ripple ( $M$ ) due to the beating phenomena between modes 1 and 5 will also decrease.

Clearly, dispersion is reduced as the width, and hence reflectivity, of the rails is reduced. The theoretical model predicts a beat length  $L_B$  of  $86 \lambda_R$  and an amplitude ripple of 1.6 dB for a structure having 6.5- $\mu\text{m}$ -wide support rails on 100- $\mu\text{m}$  centers. Beat lengths of  $137 \lambda_R$  and an amplitude ripple as large as 3 dB have been experimentally observed with similar silicon supports. Evidently, the reflectivity of the loaded rails is somewhat less than the theoretical model predicts and, hence, observed beat lengths are longer than predicted.

A 3-rail support structure is being used in the current acoustoelectric convolvers. The rails are about 4  $\mu\text{m}$  wide and are located on 368- $\mu\text{m}$  centers. The theoretical model predicts that  $L_B$  equals  $1119 \lambda_R$  and  $M$  is 1.9 dBm. Experimental evidence indicates values of  $\sim 1800 \lambda_R$  for  $L_B$  and  $M \leq 1.5$  dB. It appears that more of the acoustic energy is transferred into the fundamental mode than is indicated by the theoretical model and, therefore, the magnitude of  $M$ , which depends on the proportion of energy in the higher-order modes, is reduced. In addition to providing quantitative estimates of mode shapes, beat length and ripple, the theoretical model has yielded very useful insights into the moding phenomena and the use of rail supports.

K. L. Wang<sup>†</sup>  
S. A. Reible

#### REFERENCES

1. M. Kimura, Y. Fujino, and T. Kawamura, *Appl. Phys. Lett.* **29**, 227 (1976).
2. J. Eckstein, K. Recker, and F. Wallrafen, *Naturwissenschaften* **63**, 438 (1976).
3. M. Kimura, *J. Appl. Phys.* **48**, 2850 (1977).
4. S. N. Gupta, J. F. Vetelino, V. B. Jipson, and J. C. Field, *J. Appl. Phys.* **47**, 858 (1976).
5. W. R. Smith, H. M. Gerard, J. H. Collins, T. M. Reeder, and H. J. Shaw, *IEEE Trans. Microwave Theory Tech.* **17**, 856 (1969).
6. "Microwave Acoustics Handbook," Vol. 1A, Air Force Cambridge Research Laboratories Report No. AFCRL-TR-73-0597, A. J. Slobodnik, Jr., E. D. Conway, and R. T. Delmonico, Editors (1973), pp. 11-19.
7. S. A. Reible, J. H. Cafarella, R. W. Ralston, and E. Stern, "Convolvers for DPSK Demodulation of Spread Spectrum Signals," in *1976 Ultrasonics Symposium Proceedings* (IEEE, New York, 1976), pp. 451-455.
8. Solid State Research Report, Lincoln Laboratory, M.I.T. (1974:4), pp. 53-57.
9. K. Wang, "Modal Analysis of SAW Convolver," Technical Report 526, Lincoln Laboratory, M.I.T. (13 January 1978).

<sup>†</sup>Electrical Engineering and Computer Sciences, M.I.T.

UNCLASSIFIED

SECURITY CLASSIFICATION OF THIS PAGE (When Data Entered)

REPORT DOCUMENTATION PAGE		READ INSTRUCTIONS BEFORE COMPLETING FORM
1. REPORT NUMBER ESD-TR-78-27	2. GOVT ACCESSION NO.	3. RECIPIENT'S CATALOG NUMBER
4. TITLE (and Subtitle) Solid State Research, 1978.02	5. TYPE OF REPORT & PERIOD COVERED Quarterly Technical Summary 1 November 1977 - 31 January 1978, rept.	
7. AUTHOR(s) Alan L. McWhorter	6. PERFORMING ORG. REPORT NUMBER 1978:1	8. CONTRACT OR GRANT NUMBER(s) F19628-78-C-0002Y
9. PERFORMING ORGANIZATION NAME AND ADDRESS Lincoln Laboratory, M.I.T. P.O. Box 73 Lexington, MA 02173	10. PROGRAM ELEMENT, PROJECT, TASK AREA & WORK UNIT NUMBERS Program Element No. 65705F Project No. 649L	
11. CONTROLLING OFFICE NAME AND ADDRESS Air Force Systems Command, USAF Andrews AFB Washington, DC 20331	12. REPORT DATE 15 February 1978	
14. MONITORING AGENCY NAME & ADDRESS (if different from Controlling Office) Electronic Systems Division Hanscom AFB Bedford, MA 01731	13. NUMBER OF PAGES 80	
16. DISTRIBUTION STATEMENT (of this Report) Approved for public release; distribution unlimited.		15. SECURITY CLASS. (of this report) Unclassified
17. DISTRIBUTION STATEMENT (of the abstract entered in Block 20, if different from Report)		15a. DECLASSIFICATION DOWNGRADING SCHEDULE
18. SUPPLEMENTARY NOTES None		
19. KEY WORDS (Continue on reverse side if necessary and identify by block number) solid state devices      surface-wave technology      imaging arrays quantum electronics      photodiode devices      infrared imaging materials research      lasers      surface-wave transducers microelectronics      laser spectroscopy		
20. ABSTRACT (Continue on reverse side if necessary and identify by block number) This report covers in detail the solid state research work of the Solid State Division at Lincoln Laboratory for the period 1 November 1977 through 31 January 1978. The topics covered are Solid State Device Research, Quantum Electronics, Materials Research, Microelectronics, and Surface-Wave Technology. Funding is primarily provided by the Air Force, with additional support provided by the Army, ARPA, NSF, and DOE.		

DD FORM 1473 1 JAN 73

EDITION OF 1 NOV 65 IS OBSOLETE

UNCLASSIFIED

SECURITY CLASSIFICATION OF THIS PAGE (When Data Entered)

207 650

slf